IMPROVED PARTICLE IDENTIFICATION AT HERMES AND POLARISED VALENCE QUARK DISTRIBUTIONS IN THE PROTON

by

Jürgen Wendland

Vordiplom (TU Braunschweig, Germany, 1996)

THESIS SUBMITTED IN PARTIAL FULFILLMENT

OF THE REQUIREMENTS FOR THE DEGREE OF

MASTER OF SCIENCE

in the Department

of

Physics

SIMON FRASER UNIVERSITY

June 1999

APPROVAL

Name: Jürgen Wendland

Degree: Master of Science

Title of thesis: Improved Particle Identification at HERMES and Polarised Valence Quark Distributions in the Proton

Examining Committee: Dr. Mike Plischke (Chair)

Dr. Mike Vetterli, Research Scientist
TRIUMF, Vancouver B. C.
Adjunct Professor, SFU
Senior Supervisor

Dr. Howard Trottier, Associate Professor
Department of Physics, SFU

Dr. K. S. Viswanathan, Professor
Department of Physics, SFU

Dr. Byron Jennings, Research Scientist
TRIUMF, Vancouver B. C.
Adjunct Professor, SFU
Internal Examiner

Date Approved: ______________________

Abstract

The HERMES experiment was designed to investigate the spin structure of the nucleon using polarised deep inelastic scattering. Longitudinally polarised positrons at an energy of 27.5 GeV are scattered off various polarised hadronic targets to determine the contributions to the nucleon spin by the constituents of the nucleon.

This thesis consists of two parts. First, an improved analysis of the data from the particle identification system of the HERMES spectrometer is described. Second, an extraction of the polarised valence quark distribution functions in the proton is presented.

In order to identify the outgoing particles in the spectrometer, a sophisticated particle identification (PID) system is essential. The existing PID system of the HERMES experiment consists of a calorimeter, a preshower detector, a Čerenkov counter and a transition radiation detector. These four detectors allow for the discrimination of leptons and hadrons. The threshold Čerenkov detector also identifies pions in the hadron sample. The old analysis scheme for PID was based on early experimental results and (crude) theoretical models.

After a review of the theory of deep inelastic scattering and a description of the HERMES experiment, the development and performance of the improved particle identification scheme are discussed. A Monte Carlo model based on the probability distributions of the PID detector responses was implemented to optimise the new scheme.

In the last part of this thesis, results on the spin distributions of the valence quarks in the proton are presented. The distributions, which are consistent with parameterisations of existing world data, were calculated from asymmetries in the semi-inclusive cross sections of the two target spin states relative to the beam polarisation. The asymmetries were extracted from data taken in 1995 on ^{3}He, and in 1996 and 1997 on hydrogen.

Acknowledgements

First of all I would like to thank my supervisor Mike Vetterli for giving me the opportunity to do my Master's degree in elementary particle physics, answering every question I had and guiding me through the degree in general. I am grateful for the funding provided by SFU and TRIUMF and for the Billy Jones Memorial Scholarship. Weiterhin möchte ich mich bei der Studienstiftung des Deutschen Volkes und der Dr.-Jürgen-Ulderup-Stiftung bedanken, die mich während der zweiten Hälfte meines Studiums unterstützt haben.

I also would like to thank all the HERMES collaborators, especially the (ex-) members of HERMES Canada: Manuella and Eric for getting me started on this project, Jinsong for solving all the computer problems I had and Andy, Felix and Matthias for providing valuable hints.

In addition I would like to mention the people who helped make my stay in Canada enjoyable: Greg, Kelly, Adam, Jane, Tracy, Andrew, Connie, Ekim, Alison, Denise, Dan, Amy, Janna and Bordeaux. I also had a great time with Eldon, Andrew and Wolfgang in our basement office. Thanks to Sharon, Amanda, Susan and Candida for providing useful information on the administrative side. I would like to thank Jörn and Jillian for proof-reading part of this thesis and providing a base out there in Richmond.

Schließlich gilt mein Dank auch denen in Deutschland: Sven, Martina, Ira, Volker, Ingo, Gerrit, Ulf, Eike und Robert (Wer ist eigentlich gerade Semestersprecher?) und alle anderen. Besonderer Dank gilt meinen Eltern und meiner Schwester, die mich jederzeit voll unterstützt haben.

Contents

List of Tables

List of Figures

Chapter 1

Introduction

The structure of the nucleon, which is not entirely understood at present, is of great interest in high energy physics. The simple parton model assumes the nucleon to be composed of three quarks, two up quarks and a down quark in the case of the proton and one up and two down quarks in the case of the neutron. The quarks are confined to the nucleon through the exchange of *gluons*. In addition to these *valence quarks*, *sea quarks* are produced from and annihilate into gluons in the nucleon.

Quarks are not observed as individual particles because the QCD coupling increases with distance and it is therefore not energetically favourable for a quark to exist in isolation. However, the quarks move with relatively little constraint within the nucleon, a phenomenon known as *asymptotic freedom*.

The structure of the nucleon has been probed by scattering experiments since 1955 [1]. The early experiments probed only the unpolarised structure, but experiments at SLAC and CERN in the eighties gave first data on the spin structure of the proton by scattering polarised leptons off a polarised proton target. These experiments concluded that the quarks carry only a small fraction of the proton spin, a result known as the *spin crisis*, that is inconsistent with the parton model.

Experiments at SLAC and SMC first investigated this unexpected result. HERMES is a second generation experiment specifically designed to solve the spin puzzle. The spin structure of the nucleon is being probed by scattering polarised positrons and electrons off polarised hydrogen, deuterium and ^{3}He targets. Due to the large acceptance of the HERMES spectrometer, it is not only possible to make *inclusive* measurements that only detect the outgoing positron, but also *semi-inclusive* measurements that in addition measure a hadron in coincidence with the scattered positron.

These measurements allow for the discrimination of the contributions to the nucleon spin by the different components of the nucleon. In particular the nucleon spin is the sum of the spins of the valence quarks, the sea quarks, the gluons, and the orbital angular momentum of the quarks:

$$S_z = \frac{1}{2}(\Delta V + \Delta S) + \Delta G + \Delta L_z$$

Measurements of spin asymmetries in the pion production cross section lead to the polarised valence quark distributions. The spin distributions of sea quarks can be found from polarisation asymmetries on π^- and K^- production. The contribution by the gluons to the nucleon spin can be obtained by investigating the polarisation asymmetry in J/ψ and D^0 production or the production of hadrons with large transverse momentum [2]. The contribution by the angular momentum can possibly be extracted from data on transversely polarised targets [3].

For data analysis the identification of the particles in the final state is crucial. At HERMES, particle identification is done with a Čerenkov counter, a transition radiation detector, a preshower detector, and a calorimeter. The detector responses are analysed with a likelihood method to discriminate between hadrons and leptons. The probability analysis is based on *parent distributions* of the responses that the two particle types cause in the detector. The production of accurate parent distributions is essential for the calculation of the probabilities.

In this thesis the spin distribution functions of the valence quarks in the proton are investigated by analyzing the semi-inclusive scattering data on ^{3}He and hydrogen targets. In addition an improved particle identification scheme using data based parent distributions is presented. The underlying theoretical model is discussed in chapter 2 and the setup of the HERMES experiment in chapter 3. The implementation of the new particle identification scheme is discussed in chapter 4. The results of the inclusive and semi-inclusive measurements are presented in chapter 5 and the results on the valence quark spin distributions in chapter 6.

Chapter 2

Deep Inelastic Scattering

2.1 Kinematics

In a deep inelastic scattering (DIS) experiment, leptons are scattered off a nucleon target at high energies, with the lepton interacting with a quark in the nucleon. The inelastic scattering of the lepton off the nucleon can be considered as elastic scattering of the lepton off the quarks in the nucleon. The process is therefore sensitive to the substructure of the proton and the neutron. Quantitatively, the deep inelastic region is defined by

$$\nu, q^2 \to \infty \quad \text{with} \quad \frac{\nu}{q^2} = \text{const.},$$

where ν is the energy and q^2 the squared four-momentum that are transferred from the lepton to the nucleon.

The DIS reaction is illustrated in figure 2.1. A lepton of energy E and momentum $\vec{k}$ is scattered off a quark in the nucleon. The outgoing electron has energy E' and momentum $\vec{k}'$.

The transferred four-momentum $q = k - k'$ is carried by the virtual photon γ^* which mediates the scattering process. The analogue reaction through the exchange of a Z boson is negligible at HERMES energies.

In the lab frame where the nucleon is initially at rest, the squared four-momentum q^2 is given by:

$$q^2 \stackrel{lab}{=} -4EE' \sin^2 \frac{\theta}{2}, \tag{2.1}$$

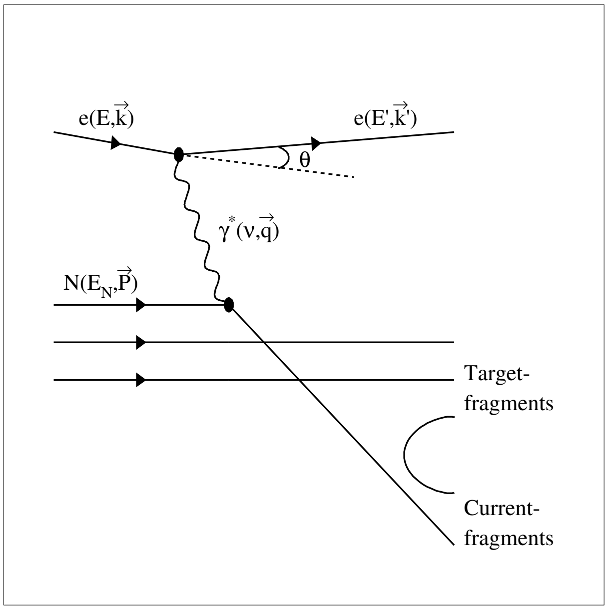

Figure 2.1: Diagram of the deep inelastic scattering process

where the mass of the electron has been neglected. Here θ is the scattering angle. The DIS variable Q^2 is defined as the negative of the squared momentum transfer,

$$Q^2 = -q^2 \tag{2.2}$$

and is positive. The energy ν of the virtual photon is given by

$$\nu = \frac{P \cdot q}{M_N} \stackrel{\text{lab}}{=} E - E'. \tag{2.3}$$

The total CM energy W of the $\gamma^* - N$ system is

$$W^2 = (P+q)^2 = P^2 + 2P \cdot q + q^2 \stackrel{\text{lab}}{=} M_N^2 + 2M_N\nu - Q^2, \tag{2.4}$$

where P is the four-momentum of the initial nucleon and M_N its rest mass.

Additional DIS variables are the parameters y and $x_{Bjørken}$. The variable y which is defined by

$$y = \frac{P \cdot q}{P \cdot k} \stackrel{\text{lab}}{=} \frac{E - E'}{E} = \frac{\nu}{E}. \tag{2.5}$$

measures the inelasticity of the scattering process; if $y = 0$, the process is elastic. $x_{Bjørken}$ is approximately the fraction of the nucleon momentum carried by the struck quark (cf. section 2.3):

$$x_{Bjørken} = \frac{Q^2}{2P \cdot q} \overset{\text{lab}}{=} \frac{Q^2}{2M_N(E - E')} = \frac{Q^2}{2M_N \nu}. \tag{2.6}$$

$x_{Bjørken}$ will often be referred to as x_{bj} or simply x.

In the case of elastic scattering $W^2 = M_N^2$ holds and equation (2.4) leads to $x_{bj} = 1$. In inelastic scattering the invariant mass M_X of the final system is always bigger than the mass of the initial nucleon because the nucleon is the lightest hadron with baryon number 1:

$$M_X = \sqrt{(P + q)^2} > M_N \tag{2.7}$$

x_{bj} can be written in terms of the masses M_X and M_N:

$$x_{bj} = \frac{Q^2}{(P + q)^2 - P^2 - q^2} = \frac{Q^2}{M_X^2 - M_N^2 + Q^2}. \tag{2.8}$$

Therefore, since Q^2 is always positive, x_{bj} is positive but less than 1 in inelastic scattering.

In a semi-inclusive measurement, a final state hadron is detected in addition to the outgoing lepton. The detected hadron can be classified as a *current fragment* or a *target fragment* (see figure 2.1). Current fragments are final state hadrons that are associated with the struck quark and can therefore be related simply to the DIS process. Target fragments are generated by the remaining (spectator) quarks. The parameters $x_{Feynman}$ (x_F) and z provide a means to distinguish between current and target fragments, which is essential to identify the struck quark.

x_F is defined by the relation

$$x_F = \frac{p_{CM}^{||}}{W} \quad -1 \leq x_F \leq 1, \tag{2.9}$$

where $p_{CM}^{||}$ is the projection of the hadron momentum onto the direction of the virtual photon in the photon-nucleon center of mass frame. Current fragments are identified by $x_F > 0$, whereas x_F is negative for target fragments.

z is the ratio of two scalar products:

$$z = \frac{p_h \cdot P}{q \cdot P} \overset{lab}{=} \frac{E_h}{\nu} \quad 0 < z \leq 1, \tag{2.10}$$

where p_h is the momentum of the final state hadron and E_h is its energy in the lab frame.

The hadron that contains the struck quark is likely to carry a significant amount of the energy ν that was transferred to this quark from the virtual photon. Therefore z tends to be large for current fragments. Hadrons that carry only a small fraction of the photon energy ν are identified by a small z. These hadrons are likely to be produced by the spectator quarks because the spectator quarks are not directly involved in the absorption of the virtual photon and thus only carry small momenta. Accordingly hadrons with small z are part of the target fragments [4].

2.2 The Deep Inelastic Scattering Cross Section

The DIS process $e + N \to e + \ldots$ described in the previous section is a good probe of the structure of the nucleon because the lepton is point-like and does not have a resolvable internal structure.

The most general form of the cross section in the lab frame is [5]:

$$\frac{\mathrm{d}^2\sigma}{\mathrm{d}E'\mathrm{d}\Omega} = \frac{E'\,\alpha^2}{E\,Q^4}\,L_{\mu\nu}\,W^{\mu\nu} \tag{2.11}$$

where $L_{\mu\nu}$ and $W^{\mu\nu}$ are the leptonic and hadronic scattering tensors respectively, and α is the fine structure constant. The leptonic tensor is calculated to leading order in QED:

$$L_{\mu\nu} = 2\left[k_\mu k'_\nu + k_\nu k'_\mu - g_{\mu\nu}\,k\cdot k' + g_{\mu\nu}\,m_e^2\right], \tag{2.12}$$

where $g_{\mu\nu}$ is the metric in Minkowski space:

$$g_{\mu\nu} = \mathrm{diag}(1, -1, -1, -1). \tag{2.13}$$

It is difficult to calculate the hadronic tensor explicitly, because the nucleon has an internal structure that must be modelled. However the application of Lorentz and gauge invariance principles yields a general form of the inelastic hadronic tensor [5]:

$$W^{\mu\nu} = \left(-g^{\mu\nu} + \frac{q^\mu q^\nu}{q^2}\right)W_1(Q^2,\nu) + \left(p^\mu - q^\mu\,\frac{p\cdot q}{q^2}\right)\left(p^\nu - q^\nu\,\frac{p\cdot q}{q^2}\right)\frac{W_2(Q^2,\nu)}{M_N^2}. \tag{2.14}$$

After some calculation the unpolarised DIS cross section can be written as:

$$\frac{\mathrm{d}^2\sigma}{\mathrm{d}E'\mathrm{d}\Omega} = 4E'^2\,\frac{\alpha^2}{Q^4}\left[2\sin^2\left(\frac{\theta}{2}\right)W_1(Q^2,\nu) + \cos^2\left(\frac{\theta}{2}\right)W_2(Q^2,\nu)\right], \tag{2.15}$$

where the mass of the electron has been neglected. The functions W_1 and W_2 are the structure functions of the nucleon. They are obtained from DIS experiments by measuring the energy E' of the scattered lepton and the scattering angle θ for a given beam energy E. The dependence on the variable Q^2, which is a measure for the scale resolved, reflects that at different resolutions the proton appears differently. In the limit of infinite momentum transfer the proton is composed of structure-less point-like particles, the quarks that exchange gluons (see section 2.3).

This cross section is only valid if the beam and the target are unpolarised. Additional terms arise in a polarised process, in which the target and the beam have well-defined polarisations. In this case the hadronic tensor becomes:

$$\begin{aligned} W^{\mu\nu} = & \left(-g^{\mu\nu} + \frac{q^\mu q^\nu}{q^2}\right) W_1(Q^2,\nu) + \left(p^\mu - q^\mu \frac{p\cdot q}{q^2}\right)\left(p^\nu - q^\nu \frac{p\cdot q}{q^2}\right) \frac{W_2(Q^2,\nu)}{M_N^2} + \\ & + i\epsilon^{\mu\nu\lambda\sigma} q_\lambda\, s_\sigma\, M_N\, G_1(Q^2,\nu) + i\epsilon^{\mu\nu\lambda\sigma} q_\lambda \left(s_\sigma\, k\cdot p - p_\sigma\, q\cdot s\right) \frac{G_2(Q^2,\nu)}{M_N}, \end{aligned} \tag{2.16}$$

where s_μ is the nucleon spin and $\epsilon^{\mu\nu\lambda\sigma}$ the totally antisymmetric tensor:

$$\epsilon^{\mu\nu\lambda\sigma} = \begin{cases} -1 & \text{if } \mu\nu\lambda\sigma \text{ is an odd perm. of 0123;} \\ 1 & \text{if } \mu\nu\lambda\sigma \text{ is an even perm. of 0123;} \\ 0 & \text{otherwise.} \end{cases} \tag{2.17}$$

G_1 and G_2 are the spin dependent structure functions of the proton. They do not enter the spin averaged DIS cross section, because the last two terms in (2.16) change signs when the proton spin is flipped, and therefore cancel.

The antisymmetry of the tensor $\epsilon^{\mu\nu\lambda\sigma}$ and the symmetry of the spin averaged lepton tensor requires that both the beam and the target be polarised to measure G_1 and G_2. In a polarised measurement the lepton tensor has an additional antisymmetric term

$$i\epsilon_{\mu\nu\alpha\beta}\, q^\alpha\, s_e^\beta,$$

which gives a nonzero contribution to the polarised DIS cross section when it is contracted with the antisymmetric part of $W^{\mu\nu}$.

Polarised DIS thus provides a method to measure the spin-dependent structure functions of the nucleon (see section 2.4). The spin-independent structure functions are determined from unpolarised DIS experiments.

2.3 Bjørken Scaling and the Quark-Parton Model

Experiments at the Stanford Linear Accelerator observed that for large momentum transfers the structure functions of the nucleon are independent of any energy scale and depend only on the ratio x_{bj} [6, 7]. This phenomenon is referred to as *Bjørken scaling* or simply *scaling*.

The quark-parton model (QPM) was first introduced by Feynman to interpret the structure functions and explain the scaling behaviour [8] (see also [9]). In this model the hadron is considered to be composed of point-like particles. These particles are called *partons*, they have spin 1/2, and their mass can be neglected in the DIS regime. The inelastic scattering of leptons off the nucleon is considered as elastic scattering off the partons.

In this model, the hadronic tensor $W^{\mu\nu}$ can be written in terms of new structure functions, F_1, F_2, g_1, and g_2:

$$\begin{aligned} F_1(Q^2, x_{bj}) &= M_N\, W_1(Q^2,\nu) \qquad & F_2(Q^2, x_{bj}) &= \nu\, W_2(Q^2,\nu) \\ \frac{g_1(Q^2, x_{bj})}{P\cdot q} &= M_N\, G_1(Q^2,\nu) \qquad & \frac{g_2(Q^2, x_{bj})}{(P\cdot q)^2} &= \frac{G_2(Q^2,\nu)}{M_N} \end{aligned} \tag{2.18}$$

With these functions the tensor becomes:

$$\begin{aligned} W^{\mu\nu} = &- g^{\mu\nu}\, F_1(Q^2, x_{bj}) + \frac{P^\mu P^\nu}{\nu}\, F_2(Q^2, x_{bj}) + \\ &+ \frac{i}{\nu}\, \epsilon^{\mu\nu\lambda\sigma}\, q_\lambda\, s_\sigma\, g_1(Q^2, x_{bj}) + \frac{i}{\nu^2}\, \epsilon^{\mu\nu\lambda\sigma}\, q_\lambda\, (P\cdot q\, s_\sigma - s\cdot q\, p_\sigma)\, g_2(Q^2, x_{bj}). \end{aligned} \tag{2.19}$$

Early DIS measurements showed that for large momentum transfers Q^2 the structure functions depend only on x_{bj}; they scale:

$$\begin{aligned} F_1(Q^2, x_{bj}) &\equiv F_1(x_{bj}) \qquad & F_2(Q^2, x_{bj}) &\equiv F_2(x_{bj}), \\ g_1(Q^2, x_{bj}) &\equiv g_1(x_{bj}) \qquad & g_2(Q^2, x_{bj}) &\equiv g_2(x_{bj}). \end{aligned} \tag{2.20}$$

In the QPM, x_{bj} is the fraction of the nucleon momentum carried by the struck quark if the reaction is considered in the Breit frame. In this infinite momentum frame the momentum of the struck quark is turned around when it scatters off the photon [10]. The scaling behaviour is explained by assuming that the partons are point-like particles. The unpolarised structure functions for an electron hitting a parton with a given momentum fraction x_{bj}

are [11]:

$$
\begin{aligned}
F_1^{point}\left(\frac{Q^2}{2M_N\,\nu}\right) &= \frac{1}{2x_{bj}^2}\,\frac{Q^2}{2M_N\,\nu}\,\delta\left(1-\frac{1}{x_{bj}}\,\frac{Q^2}{2M_N\,\nu}\right),\\
F_2^{point}\left(\frac{Q^2}{2M_N\,\nu}\right) &= \delta\left(1-\frac{1}{x_{bj}}\,\frac{Q^2}{2M_N\,\nu}\right).
\end{aligned}
\tag{2.21}
$$

The structure functions of the proton follow by summing the parton structure functions over all flavours weighted by the probabilities $f_i(x_{bj})$ that a parton of flavour i has a fraction x_{bj} of the nucleon momentum and by the squared fractional charge e_i^2 of the quark in units of the elementary charge e:

$$
F_1(x_{bj}) = \frac{1}{2}\sum_i f_i(x_{bj})\,e_i^2 \qquad F_2(x_{bj}) = \sum_i f_i(x_{bj})\,e_i^2\,x_{bj},
\tag{2.22}
$$

where x_{bj} has been identified with its definition (2.6) using the δ-function in (2.21).

The Callan-Gross relation [12] which shows that the structure functions are not independent is a direct consequence of equation (2.22):

$$
F_2(x_{bj}) = 2x_{bj}\;F_1(x_{bj}).
\tag{2.23}
$$

This relation which assumes that the quarks have spin $1/2$ has been verified experimentally in the scaling region.

The spin structure function $g_1(x_{bj})$ has a similar interpretation as the function $F_1(x_{bj})$. g_1 measures the spin distribution of the quarks in the nucleon:

$$
g_1(x_{bj}) = \frac{1}{2}\sum_i e_i^2\left[f_i^+(x_{bj}) - f_i^-(x_{bj})\right] = \frac{1}{2}\sum_i e_i^2\;\Delta f_i(x_{bj}),
\tag{2.24}
$$

where f_i^+ (f_i^-) indicates the probability to find a quark with momentum fraction x_{bj} and with spin parallel (antiparallel) to the nucleon spin. $g_2(x_{bj})$ is related to parton momenta transverse to the momentum of the nucleon. In the parton model this function vanishes,

$$
g_2(x_{bj}) = 0,
$$

since the partons are assumed to have only a momentum fraction $x_{bj}P$ that is parallel to the nucleon momentum.

In conclusion, the QPM gives a simple explanation of the DIS cross section and its scaling behaviour with the basic assumptions that the nucleon is composed of point-like fermions whose masses can be neglected.

2.4 Asymmetries in Inclusive and Semi-Inclusive DIS

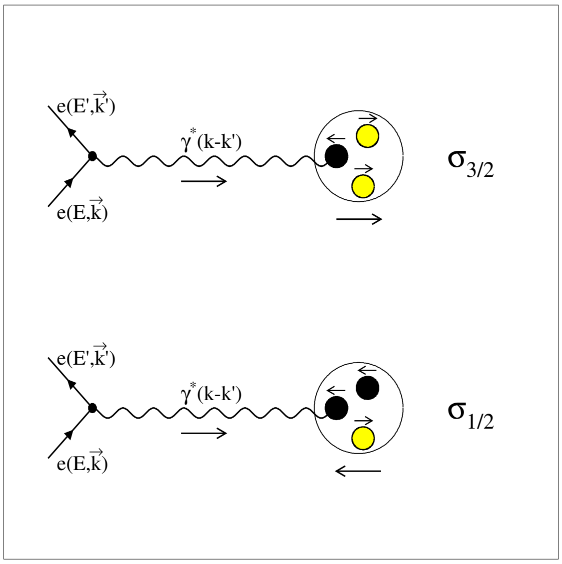

Figure 2.2: Polarised deep inelastic scattering: Top: The nucleon spin and the photon spin are aligned; the probability distribution $q_-(x_{bj})$ is measured. Bottom: The spins are anti-aligned; the cross section yields $q_+(x_{bj})$.

The physical interpretation of g_1 given in the last section is supported by the polarised DIS process shown in figure 2.2. The figure also indicates how to measure the spin structure functions.

A longitudinally polarised lepton emits a circularly polarised virtual photon. The photon with spin 1 interacts with a spin 1/2 quark in the nucleon. The quark must have spin anti-aligned to the spin of the virtual photon, otherwise it would have spin 3/2 after absorbing the photon. The cross section $\sigma_{3/2}$ describes the DIS process when the spins of the photon and the nucleon are aligned. It is proportional to the sum of the distributions $f_i^- \equiv q_-(x_{bj})$ weighted by the fractional charges of the quarks. In the other case, the cross section $\sigma_{1/2}$ is sensitive to the distributions $q_+(x_{bj})$:

$$\sigma_{3/2} \propto \sum_{q=u,\bar{u},d...} e_q^2\, q_-(x_{bj}) \qquad \sigma_{1/2} \propto \sum_{q=u,\bar{u},d...} e_q^2\, q_+(x_{bj}). \tag{2.25}$$

The difference of the two probability distributions $q_+(x_{bj})$ and $q_-(x_{bj})$ is determined by switching the polarisation of the nucleon.

Inclusive Asymmetries

The inclusive cross sections $\sigma_{1/2}$ and $\sigma_{3/2}$ for the processes shown in figure 2.2 describe the absorption of the virtual photon by the nucleon. It is not possible to measure these functions or the probability distributions $q_+(x_{bj})$ and $q_-(x_{bj})$ directly. However, the *inclusive asymmetry* A_1, defined by

$$A_1 = \frac{\sigma_{1/2} - \sigma_{3/2}}{\sigma_{1/2} + \sigma_{3/2}}, \tag{2.26}$$

can be related to the *lepton-nucleon asymmetry* $A_{||}$, defined below. The asymmetry A_1 is expected to be positive for the proton, since to 1^{st} order the photon can be absorbed by two u-quarks if the nucleon and the photon spin are anti-aligned compared to one d-quark in the other configuration (figure 2.2). The cross sections are in addition weighted by the squared charges of the quarks (equation (2.25)), i. e. a factor of $4/9$ for the u-quark and a factor of $1/9$ for the d. By the same reasoning, A_1^n is expected to be negative and smaller for the neutron. The experimental values are $A_1^p \approx 0.40$ and $A_1^n \approx -0.05$ [13, 14] at $x_{bj} = 0.3$ where the contributions to the asymmetry by the valence quarks dominate.

The spin structure function g_1 can now be found if equations (2.22) and (2.24) are substituted into (2.26) using (2.25): $g_1 = A_1 \cdot F_1$. (Small contributions by the spin structure function g_2 are neglected [15].) The function F_1 is obtained from unpolarised deep inelastic scattering. The asymmetry in equation (2.26) can be determined in polarised deep inelastic scattering.

However, the measured asymmetry A_{exp} is not the same as the photon asymmetry given in (2.26). In experiment the lepton-nucleon asymmetry $A_{||}$ is reduced by the target and the beam polarisation, p_T and p_B, and the fraction f of the polarisable nucleons in the target. The observed asymmetry A_{exp} is therefore given by

$$A_{exp} = (p_B\, p_T\, f) \cdot A_{||}, \tag{2.27}$$

where the asymmetry $A_{\|}$ is defined as

$$A_{\|} = \frac{\sigma_{\uparrow\downarrow} - \sigma_{\uparrow\uparrow}}{\sigma_{\uparrow\downarrow} + \sigma_{\uparrow\uparrow}}. \tag{2.28}$$

Here $\sigma_{\uparrow\downarrow}$ is the cross section that is measured if target and beam polarisations are anti-aligned and $\sigma_{\uparrow\uparrow}$ is the scattering cross section if the polarisations are aligned.

Disregarding small contributions by a transverse asymmetry A_2 (see [15]), $A_{\|}$ is related to A_1 by

$$A_1 \approx \frac{A_{\|}}{D}. \tag{2.29}$$

The *depolarisation factor* D is a measure for the depolarisation of the virtual photon with respect to the polarisation of the incident lepton. It follows from the kinematics of the scattering process that

$$D = \frac{y(2-y)}{y^2 + 2(1-y)(1+R)}, \tag{2.30}$$

where R is the ratio of the longitudinal to the transverse cross section [16].

Thus the spin structure function g_1 is given to a good approximation in terms of observable quantities by

$$g_1(x) \approx F_1(x)\ A_1(x) \approx F_1(x)\frac{A_{\|}}{D}. \tag{2.31}$$

Semi-inclusive Asymmetries

In a semi-inclusive measurement the detection of a final state hadron provides additional information on the type and the four-momentum p_h of the hadron.

To describe the fragmentation of a quark into a hadron, it is assumed that the fragmentation process is independent of the lepton-nucleon interaction. Moreover, the fragmentation is assumed to be independent of the spin orientation of the quark.

The *fragmentation functions* $D_q^h(z, x, Q^2)$ describe the probability distributions for a quark q to fragment into a hadron h with energy $E_h = z \cdot \nu$. In terms of these functions the multiplicity for the process $e + N \to e + h + \ldots$ can be written:

$$\frac{1}{\sigma_{TOT}} \frac{\mathrm{d}\sigma(eN \to eh \ldots)}{\mathrm{d}z\,\mathrm{d}x\,\mathrm{d}Q^2} = \frac{\sum_{q=u,\bar{u},d\ldots} e_q^2\ q(x)\ D_q^h(z, x, Q^2)}{\sum_{q=u,\bar{u},d\ldots} e_q^2\ q(x)}. \tag{2.32}$$

The dependence of the fragmentation function on x_{bj} and the momentum transfer is commonly neglected because D_q^h is not a strong function of x_{bj} and Q^2,

$$D_q^h(z, x, Q^2) \approx D_q^h(z).$$

The asymmetry defined in equation (2.26) now reads:

$$A_1^h = \frac{\sum_{q=u,\bar{u},d...} e_q^2 \, \Delta q(x) \, D_q^h(z)}{\sum_{q=u,\bar{u},d...} e_q^2 \, q(x) \, D_q^h(z)}, \tag{2.33}$$

where

$$\Delta q(x) \equiv q_+(x) - q_-(x) \quad \text{and} \quad q(x) \equiv q_+(x) + q_-(x). \tag{2.34}$$

The number of hadrons detected when the *photon* and the *nucleon* spin are anti-aligned $N_{1/2}^h$ for a given x_{bj} and z bin is proportional to the cross section given in equation (2.32):

$$N_{1/2}^h \sim \frac{\mathrm{d}\sigma_{1/2}(eN \to eh \ldots)}{\mathrm{d}z} = \sum_{q=u,\bar{u},d...} e_q^2 \, q_+(x) \, D_q^h(z). \tag{2.35}$$

An analogous equation holds for $N_{3/2}^h$.

The count rates depend on nine different fragmentation functions if the analysis is restricted to pion production from up, down, and strange quarks and anti-quarks. Using isospin and charge conjugation symmetry it is straightforward to reduce the number of fragmentation functions to three by grouping them into *favoured*, *unfavoured*, and *strange* functions labelled D_1, D_2, and D_3 respectively [17]:

$$\begin{aligned}
D_1(z) &\equiv D_u^{\pi^+}(z) = D_d^{\pi^-}(z) = D_{\bar{d}}^{\pi^+}(z) = D_{\bar{u}}^{\pi^-}(z) \\
D_2(z) &\equiv D_d^{\pi^+}(z) = D_u^{\pi^-}(z) = D_{\bar{u}}^{\pi^+}(z) = D_{\bar{d}}^{\pi^-}(z) \\
D_3(z) &\equiv D_s^{\pi^+}(z) = D_s^{\pi^-}(z) = D_{\bar{s}}^{\pi^+}(z) = D_{\bar{s}}^{\pi^-}(z)
\end{aligned} \tag{2.36}$$

Therefore the pion count rates can be written for a hydrogen target as:

$$\begin{aligned}
N_{1/2}^{\pi^+} &\sim \left[\frac{4}{9}u_+(x) + \frac{1}{9}\bar{d}_+(x)\right] D_1(z) + \left[\frac{4}{9}\bar{u}_+(x) + \frac{1}{9}d_+(x)\right] D_2(z) + \frac{1}{9}\left[s_+(x) + \bar{s}_+(x)\right] D_3(z) \\
N_{1/2}^{\pi^-} &\sim \left[\frac{4}{9}u_+(x) + \frac{1}{9}\bar{d}_+(x)\right] D_2(z) + \left[\frac{4}{9}\bar{u}_+(x) + \frac{1}{9}d_+(x)\right] D_1(z) + \frac{1}{9}\left[s_+(x) + \bar{s}_+(x)\right] D_3(z)
\end{aligned} \tag{2.37}$$

and similarly for the rates $N_{3/2}^{\pi^+}$, and $N_{3/2}^{\pi^-}$.

The contributions to the count rates by the sea quarks cancel if the following differences are taken:

$$\begin{aligned} N_{1/2}^{\pi^+-\pi^-} &\equiv N_{1/2}^{\pi^+} - N_{1/2}^{\pi^-} \sim \left[\frac{4}{9}u_+^v(x) - \frac{1}{9}d_+^v(x)\right][D_1(z) - D_2(z)] \\ N_{3/2}^{\pi^+-\pi^-} &\equiv N_{3/2}^{\pi^+} - N_{3/2}^{\pi^-} \sim \left[\frac{4}{9}u_-^v(x) - \frac{1}{9}d_-^v(x)\right][D_1(z) - D_2(z)]\,, \end{aligned} \tag{2.38}$$

where

$$q_{+(-)}^v(x) = q_{+(-)}(x) - \bar{q}_{+(-)}(x) \tag{2.39}$$

is the probability that a valence quark with spin aligned (anti-aligned) to the nucleon spin carries a fraction x of the nucleon momentum.

The sum of the two quantities in (2.38) is related to the unpolarised distributions $u^v(x)$ and $d^v(x)$ defined in (2.34) and (2.39):

$$N_{1/2}^{\pi^+-\pi^-} + N_{3/2}^{\pi^+-\pi^-} \sim \left[\frac{4}{9}u^v(x) - \frac{1}{9}d^v(x)\right][D_1(z) - D_2(z)]\,, \tag{2.40}$$

whereas their difference relates to the polarised functions $\Delta u^v(x)$ and $\Delta d^v(x)$:

$$N_{1/2}^{\pi^+-\pi^-} - N_{3/2}^{\pi^+-\pi^-} \sim \left[\frac{4}{9}\Delta u^v(x) - \frac{1}{9}\Delta d^v(x)\right][D_1(z) - D_2(z)]\,, \tag{2.41}$$

The ratio of the two sums can be identified with the asymmetry $A_{1,p}^{\pi^+-\pi^-}(x)$ for a *proton* target, if the probability distributions are identified specifically with the quark distributions in the proton, $u^v(x) \equiv u_{proton}^v(x)$ and $d^v(x) \equiv d_{proton}^v(x)$:

$$A_{1,p}^{\pi^+-\pi^-}(x) = \frac{N_{1/2}^{\pi^+-\pi^-} - N_{3/2}^{\pi^+-\pi^-}}{N_{1/2}^{\pi^+-\pi^-} + N_{3/2}^{\pi^+-\pi^-}} = \frac{4\,\Delta u^v(x) - \Delta d^v(x)}{4\,u^v(x) - d^v(x)}, \tag{2.42}$$

The fragmentation functions cancel in this ratio and they are thus not needed for the calculation of $A_{1,p}$. A similar expression is found for the neutron:

$$A_{1,n}^{\pi^+-\pi^-}(x) = \frac{4\,\Delta d^v(x) - \Delta u^v(x)}{4\,d^v(x) - u^v(x)}. \tag{2.43}$$

This asymmetry is written in terms of the parton distributions $\Delta u^v(x)$ and $\Delta d^v(x)$ of the *proton*. Isospin symmetry was used to identify the *neutron* distributions $\Delta u_{neutron}^v(x)$ and

$\Delta d^v_{neutron}(x)$ with the functions of the *proton*:

$$\begin{aligned} u^v_{neutron} &= d^v_{proton} \equiv d^v \qquad & \Delta u^v_{neutron} &= \Delta d^v_{proton} \equiv \Delta d^v \\ d^v_{neutron} &= u^v_{proton} \equiv u^v \qquad & \Delta d^v_{neutron} &= \Delta u^v_{proton} \equiv \Delta u^v \end{aligned} \tag{2.44}$$

The asymmetry for a ^{3}He target can therefore be written as:

$$A_{1,\,^3\mathrm{He}}^{\pi^+-\pi^-}(x) = \frac{-\Delta u^v(x) + 4\,\Delta d^v(x)}{7\,u^v(x) + 2\,d^v(x)} \tag{2.45}$$

The ^{3}He and proton asymmetries can be measured in polarised experiments with ^{3}He and H targets. The functions $\Delta u^v(x)$ and $\Delta d^v(x)$ are determined from this measurement using unpolarised valence quark distributions which are well known from experiments with unpolarised targets.

2.5 Extraction of the Polarised Valence Quark Distributions

The MRST Parameterisation

The MRST parameterisation is a fit to the world data on $F_2(x, Q^2)$ and gives the necessary information on the unpolarised structure functions to use as input in the determination of the polarised quark distributions $\Delta q^v(x)$ from the asymmetries given in equations (2.42) and (2.45).

The parameterisation of the parton distribution functions by Martin, Roberts, Stirling, and Thorne is a recent analysis of both experimental measurements and theoretical models [18]. The distributions are given in figure 2.3. In practice, the functions $f(x, Q^2)$ were determined by parameterising the distributions at a low value of $Q^2 = Q_0^2$. For higher momentum transfers the functions were calculated by a next-to-leading-order evolution.

The analysis is based on a wide range of data from deep inelastic scattering and related hard scattering experiments and new theoretical methods. The theoretical models include a sophisticated treatment of the charm contribution to the structure functions and a better incorporation of the heavy quark distributions.

The Spin-Dependent Quark Distributions $\Delta q^v(x)$

The spin-dependent quark distributions are obtained from polarised semi-inclusive and unpolarised measurements. The semi-inclusive measurement yields information on the asymme-

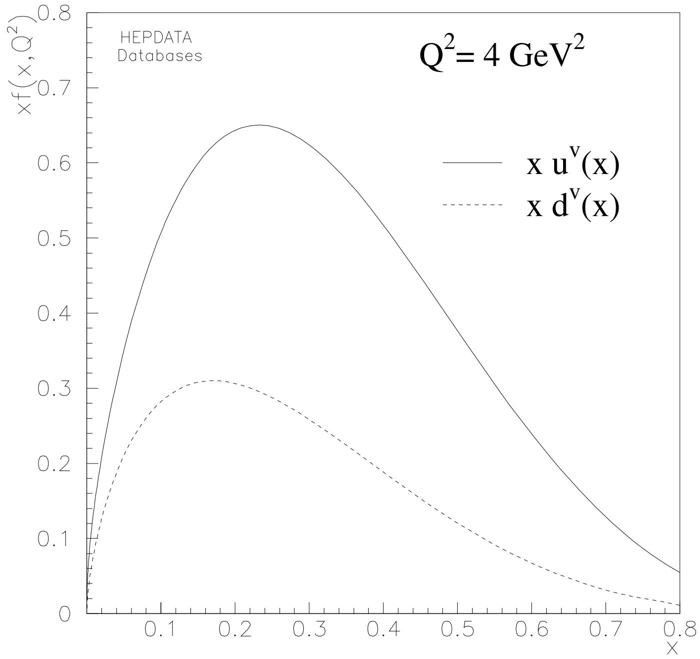

Figure 2.3: MRST parton distributions at $Q^2 = 4\,\mathrm{GeV}^2$; the solid line shows the distribution of the valence up-quark in the proton, the dotted line the distribution of the valence down-quark in the proton.

tries given in section 2.4, while the unpolarised measurements provide the spin-independent structure functions $u^v(x)$ and $d^v(x)$. These unpolarised measurements are summarised by the MRST parameterisation.

The polarised structure functions $\Delta u^v(x)$ and $\Delta d^v(x)$ of the proton can then be written as:

$$\begin{aligned}
\Delta u^v(x) &= \frac{1}{15}\left[4\,A_{1,p}^{\pi^+-\pi^-}(x)\,(4\,u^v(x) - d^v(x)) + A_{1,{}^3\mathrm{He}}^{\pi^+-\pi^-}(x)\,(7\,u^v(x) + 2\,d^v(x))\right] \\
\Delta d^v(x) &= \frac{1}{15}\left[A_{1,p}^{\pi^+-\pi^-}(x)\,(4\,u^v(x) - d^v(x)) + 4\,A_{1,{}^3\mathrm{He}}^{\pi^+-\pi^-}(x)\,(7\,u^v(x) + 2\,d^v(x))\right].
\end{aligned} \tag{2.46}$$

Chapter 3

The HERMES Experiment

The HERMES (HERA Measurement of Spin) experiment is located at the Deutsches Elektronensynchrotron (DESY) in Hamburg, Germany. The experiment is being carried out in the East Hall of the Hadron Elektron Ring Anlage (HERA) and has been running since 1995.

3.1 HERA

A diagram of the HERA accelerator facility is shown in figure 3.1. The 6.3 km long tunnel contains two synchrotrons, one for electrons with energy 27.5 GeV and one for hadrons with 820 GeV (now 920 GeV) travelling in the opposite direction. In 1996 and 1997, positrons were used instead of electrons. HERMES physics is generally not affected by the choice of the lepton type, except for the different physical processes that are used to measure the *luminosity* (see section 3.3.4), which is defined as the number of particles passing per unit time through a cross section with unit area times the number of target particles per unit area.

The accelerator is used by four different experiments, H1 in the North Hall, ZEUS in the South Hall, HERA-B in the West Hall, and HERMES in the East Hall. ZEUS and H1 are colliding beam experiments. HERA-B and HERMES are fixed target experiments, HERA-B utilises the proton beam and HERMES the positron beam.

The stored positron beam is polarised transversely to the beam direction. The polarisation is self-induced by emission of synchrotron radiation. This effect was first predicted by Sokolov and Ternov in 1964 [19]. According to their theory the beam polarisation in an

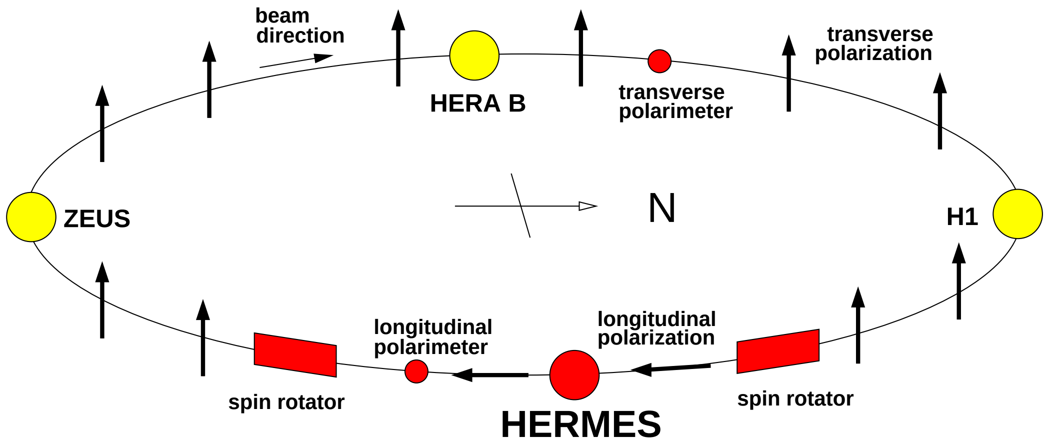

Figure 3.1: The HERA Synchrotron at DESY

ideal ring builds up following the equation

$$P(t) = P_{ST}\left(1 - e^{t/\tau_{ST}}\right), \tag{3.1}$$

where P_{ST} is the equilibrium polarisation and τ_{ST} the polarisation rise-time [20, 21].

In a real synchrotron the maximum polarisation is reduced by several effects: Unlike in an ideal ring the magnetic field is not everywhere perpendicular to the plane of the beam. In addition field-non-uniformities are caused by misalignments and field errors.

Independent of the Sokolov-Ternov effect the emission of synchrotron photons leads to stochastic diffusion of the positron spins. The misalignment of the magnets increases this effect resulting in a depolarisation of the beam. If the diffusion is described by the depolarisation time constant τ_D, the maximum achievable polarisation is given by

$$P_{max} = P_{ST}\,\frac{\tau_D}{\tau_{ST} + \tau_D}. \tag{3.2}$$

The average beam polarisation in 1996 and 1997 was above 50%.

The transversely polarised positron beam is rotated into the longitudinal direction upstream of the HERMES experiment in order to measure the process shown in figure 2.2. It is rotated back downstream of the experiment. The spin rotation is accomplished by an arrangement of vertical and horizontal bends in the beam line [22].

The transverse polarisation is measured in the West straight section. The measurement takes advantage of the angular dependence of the polarised Compton cross section for scattering of left and right circularly polarised laser light off transversely polarised electrons. A position sensitive calorimeter measures the spatial asymmetry in the energy deposition of the backscattered photons for the two polarisations. The beam polarisation is determined from this asymmetry.

In 1997 a longitudinal polarimeter was installed in the HERA East section [23]. Similarly to the transverse polarimeter the polarisation measurement uses the spin-dependent Compton cross section. The polarisation is calculated from the energy asymmetry under reversal of the laser beam helicity that is measured in the calorimeter of the polarimeter. By providing an independent polarisation measurement the longitudinal polarimeter reduces the systematic uncertainty of the beam polarisation measurement and provides redundancy.

3.2 The Target

A gaseous target which is internal to the positron storage ring is used in the HERMES experiment. The use of a gas allows for fast polarisation changes and provides a very pure target. Several different polarised and unpolarised gases have been used so far. In 1995 the experiment was run with a polarised $^3\vec{\mathrm{He}}$ target. In 1996 and 1997 the target was polarised hydrogen. In addition to the polarised targets, beam-time was dedicated to unpolarised running with H_2, D_2, ^{3}He and N_2.

Two different setups are used to inject the gas into the target cell in the storage ring. An optically pumped polarised $^3\vec{\mathrm{He}}$ cell was used in 1995 and an atomic beam source was used in 1996 and 1997. Since data taken in 1996 and 1997 were analysed in this thesis, only the atomic beam source is discussed in more detail.

The Target Cell

The target cell is shown schematically in figure 3.2. The storage cell has an elliptical cross section with principal axes of 29.0 and 9.8 mm. A cell was chosen over a free atomic beam to increase the areal density of the target by more than two orders of magnitude [24]. A further improvement of the density is achieved by cooling the cell to temperatures between 25 and 100 K depending on the target gas used.

The gas is injected in the middle of the cell and leaks out of the ends, where it is pumped away by a powerful differential pumping system. This technique provides a maximum density

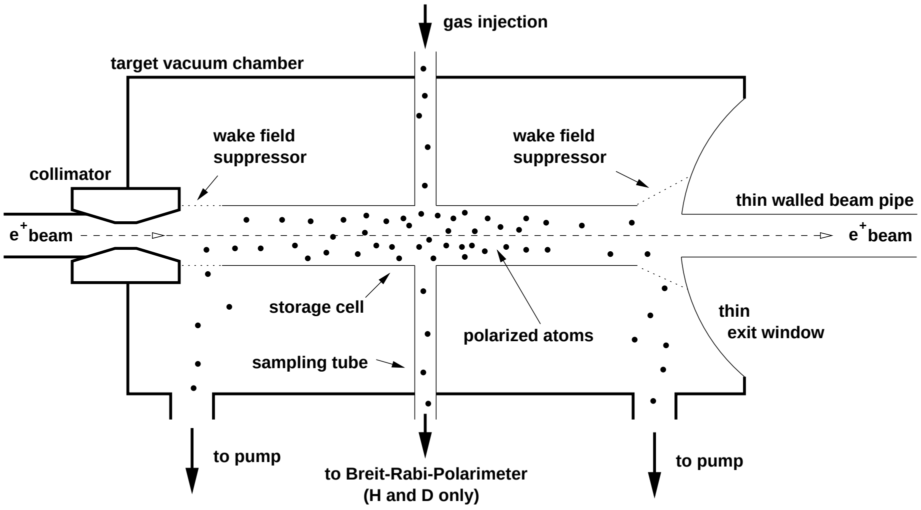

Figure 3.2: The target cell and the target chamber

of the gas in the target region and minimizes the effect on the positron beam outside of the target cell.

Wake field suppressors connect the target cell to the beam pipe on both ends. Wake fields are electromagnetic fields that are induced in a cavity when an alternating current passes through it. In this case the bunch structure of the beam plays the role of the current and the target cell/chamber is the cavity. The wake field suppressors decrease the induction of wake fields by providing a smooth transition between the target cell and the beam pipe.

The target region is protected from synchrotron radiation by two collimators, C1 and C2. C1 is located 2 m upstream of the target and C2 directly in front of it (cf. figure 3.2). A thin walled window in the vacuum chamber downstream of the storage cell allows scattered particles to enter the spectrometer almost unimpeded.

The Atomic Beam Source

An atomic beam source (ABS) was used in 1996 and 1997 to provide an atomic hydrogen target. The polarised gas is prepared in three steps [25]. First molecular hydrogen is dissociated into atoms by a radio frequency discharge. The atoms are then electron polarised by separation in a Stern-Gerlach apparatus using a sextupole magnet. The electron polarisation is transferred to the protons by adiabatic high frequency transitions. A weak field

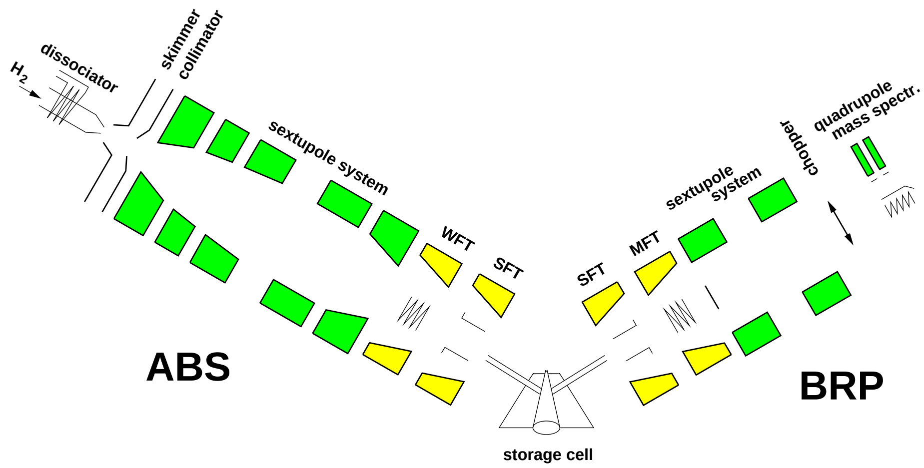

Figure 3.3: The atomic beam source (ABS) and the Breit Rabi Polarimeter (BRP)

transition (WFT) selects negative polarisation and a strong field transition (SFT) positive proton polarisation.

The Breit Rabi Polarimeter

The target polarisation is measured with a Breit Rabi Polarimeter (BRP). The polarisation measurement is in principle the reverse of the polarisation process. Specific hyperfine states of the target atoms are selected by a SFT, a WFT and a sextupole magnet. The relative occupations of the states are then measured in a mass spectrometer. The electron and the nuclear polarisations are determined from these measurements [26].

3.3 The Spectrometer

The spectrometer used to detect DIS events in the HERMES experiment is a wide-angle forward spectrometer symmetric about the horizontal plane. The acceptance covers scattering angles from 40 to 220 mrad and a range from $x_{bj} = 0.02$ to 1.0, although there are very few events with $x > 0.8$. A schematic picture of the spectrometer is given in figure 3.4. The following sections summarise the features of the individual parts of the spectrometer. A more detailed description can be found in [27].

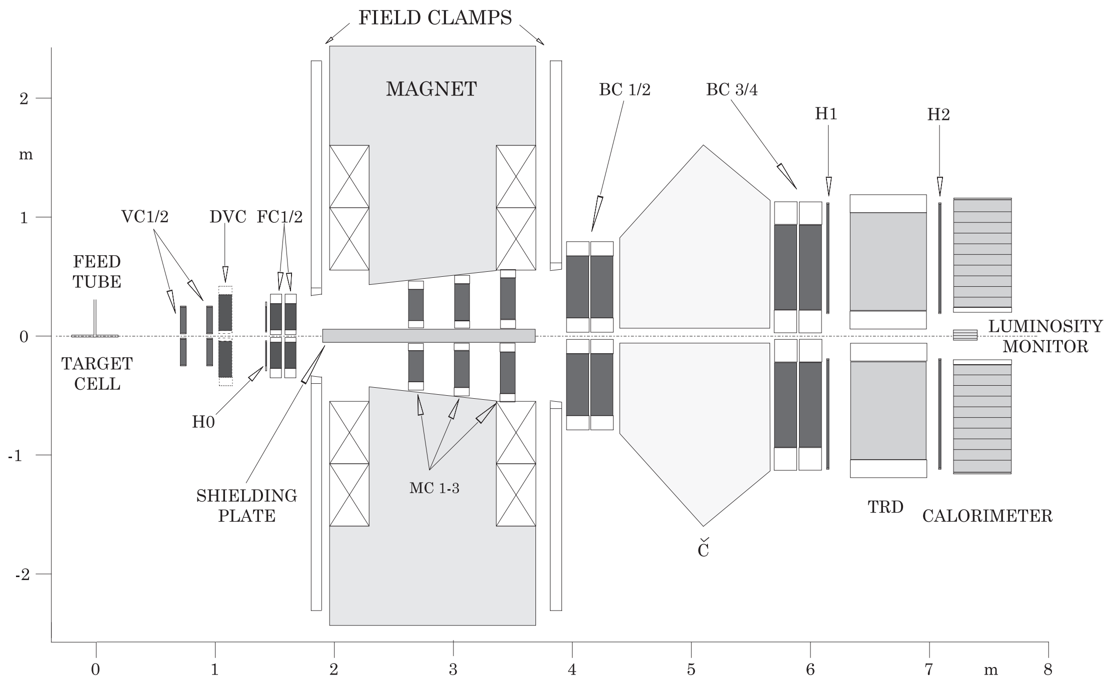

Figure 3.4: The Hermes Spectrometer

3.3.1 The Magnet

The spectrometer magnet provides the necessary magnetic field to measure the momentum of the observed tracks. It is a conventional dipole magnet operating at an integrated field strength of 1.3 Tm. The variation of the field strength within the geometrical acceptance is less than 10%.

A massive iron plate prevents the field from influencing the beams. Fringe fields are shielded from the rest of the detector with a set of field clamps. The fields do not exceed 0.1 T in the adjacent drift chambers.

3.3.2 The Tracking Detectors

The front tracking system (VC1/2, DVC, FC1/2) measures the initial particle trajectories and the vertex of the event. The particle momentum is determined by matching these tracks to trajectories in four drift chambers behind the magnet (BC1/2, BC3/4).

All the wire planes are arranged in only three different directions to facilitate track reconstruction: vertical X-planes, and U- and V-planes tilted by $\pm 30°$ to the vertical. There are no horizontal wires because they would sag due to the size of the chambers. When all chambers are fully operational the momentum and scattering angle resolution is limited only by multiple scattering and bremsstrahlung in the target cell walls and the vertex chambers.

Except for the vertex chambers and the magnet chambers, the installed tracking detectors are drift chambers that work on the following principle: A charged particle ionises gas in the detector chamber; the high electric field accelerates the electrons and initiates an avalanche near a wire. The charge collected at the wire causes a measurable signal. A spatial resolution smaller than the wire distance is achieved by measuring the difference between the time when the particle passes through the detector and the time when the avalanche is detected.

The vertex chambers are microstrip gas chambers and the magnet chambers are multiwire proportional chambers, neither of which measure drift time. The position measurement is achieved by determining near which wire the avalanche occurred.

The Vertex Chambers

The vertex chambers (VC) are located in close proximity to the target and the beam-pipe and are thus exposed to high backgrounds. A high resolution in the measurement of the scattering angle and the position is required to distinguish single tracks and determine the vertex.

The detector type that meets these requirements is a microstrip gas chamber. In these chambers the wires are replaced by metal strips etched on a substrate.

In 1996 and 1997 the vertex chambers reached an efficiency as high as 95% and a resolution of about 65 μm.

The Drift Vertex Chambers

The drift vertex chambers (DVC) are located behind the vertex chambers. They were installed in 1997 to provide redundancy in case one of the chambers in the front region fails.

The design of the DVC's is similar to the FC's (see below), only the drift cell size is smaller. The geometrical acceptance is ± 35 mrad to ± 270 mrad vertically and ± 200 mrad in the horizontal direction, extending the standard acceptance for a future upgrade to detect muons with a large polar angle.

The spatial resolution of the drift vertex chambers is about 220 μm.

The Drift Chambers

The chambers FC1, FC2, BC1/2 and BC3/4 are conventional drift chambers. The wires are arranged in the U-, V- and X-directions. Each plane of wires has alternating cathode wires at negative high voltage and anode wires at ground potential. In between the wire planes are cathode foils.

Each chamber module consists of six drift cell layers in the configuration UU', XX' and VV'. The primed layers are staggered by half a cell size with respect to the other layers to help resolve left-right ambiguities. Ambiguities occur with only one plane of wires because it is not possible to determine from the signal of one plane on which side of the wire the particle passed.

The gas was chosen with regard to the hazards of flammable gases in a tunnel environment. It is a mixture of 90% Argon, 5% CO_2 and 5% CF_4. This mixture exhibits a high drift velocity and is not flammable.

The front drift chambers FC1 and FC2 have a cell size of 7 mm. Their spatial resolution depends on the drift distance and reaches a minimum of about 160 μm. The drift cell size of the back chambers is 15 mm; the resolution is about 275 μm.

The Magnet Chambers

The magnet chambers (MC1, MC2 and MC3) are multi-wire proportional chambers. This type of tracking chamber can be operated in a strong magnetic field without severe loss of performance because the position measurement does not rely on a drift time measurement as in the case of the drift chambers. The anode wires are 2 mm apart, providing a resolution of 577 μm. Three separate modules were installed, each consisting of a U-, X- and V-plane. The centers of the planes are 21 mm apart.

Originally the magnet chambers were installed to resolve ambiguities in matching front and back tracks, but this is unnecessary due to low background. The MC's are now mainly used to detect low momentum particles that are beyond the acceptance of the back tracking system.

Track Reconstruction

The HERMES reconstruction program (HRC) has four main sections: Identification of particle tracks in the front and the back chambers, matching of front and back tracks, determination of the track momentum, and preliminary particle identification [28].

The main problem of the track identification is to find tracks with a resolution of 250 μm in a spectrometer of a few meters size. The chosen solution is a tree-search algorithm that finds tracks separately for the front and the back chambers. The separation of the front and the back of the spectrometer simplifies the tracking procedure because the partial tracks are approximately straight lines.

The algorithm considers the signal pattern in the tracking detectors initially as a whole. In the next step the program eliminates detector halves that contain no signals. Then quarters of the tracking detectors that contain no signals are dropped. 14 of these iterative steps are necessary to reach the resolution of the spectrometer. However, for track finding a resolution of only 2 mm is needed, which reduces the number of iterations to 11. During the iteration, the pattern is compared with a database to ensure that only physically possible tracks are kept.

Once the partial tracks in the front and the back part of the tracking system are found, they are matched by comparison of their coordinates at the midplane of the magnet. The full tracks are matched with tracks in another lookup table to determine their momenta. The table is generated only once during initialisation of the reconstruction program. Consequently no calculations are necessary for the identification of the particle tracks and the determination of their momenta because the tracks are only compared with a database. The reconstruction is therefore very fast allowing for efficient data analysis.

3.3.3 The Particle Identification System

The particle identification system is located in the rear section of the spectrometer behind the magnet. Charged particles are identified with four different detectors (figure 3.4): a threshold Čerenkov counter (Č), a transition radiation detector (TRD), a preshower detector (H2), and a lead-glass calorimeter. In addition neutral particles are distinguished from charged particles using the hodoscope H1 and the preshower detector.

The four detectors together discriminate positrons, pions and other hadrons. An efficient positron identification system is crucial to select DIS events in a regime with large hadron background from photo-production. The PID system was designed to provide a very clean positron sample. In off-line data analysis the hadron rejection factor (HRF), defined as the ratio of the number of all hadrons to the number of hadrons misidentified as positrons, reaches as high as 10^4 when all detectors are fully operational (see also chapter 4).

The primary purpose of the threshold Čerenkov detector is to identify pions in the hadron sample. The extraction of the contributions of the quark sea and the valence quarks to the nucleon spin relies on an efficient pion identification.

The transition radiation detector provides a means to distinguish positrons and hadrons. A probability analysis of the TRD response allows an HRF of about 130 at a positron identification efficiency of 90%. The calorimeter and the preshower detector serve in the trigger to identify DIS events, in addition to contributing to the particle identification (section 3.4). The PID detectors are described in the following sections. For a more detailed description, see [27]. The performance of the particle identification system is discussed in detail in chapter 4.

The Calorimeter

The calorimeter is built from F101 lead-glass blocks. The blocks have a cross section of $9 \times 9\,\mathrm{cm}^2$ and are 50 cm long. Each detector half is assembled from 420 single blocks. The density of lead-glass is $3.86\,\mathrm{g/cm}^3$, resulting in a total weight of the calorimeter of over 13 tons. A photo multiplier tube is attached at the back of each block to detect the light output. A diagram of the calorimeter is shown in figure 3.5.

Both calorimeter halves can be moved away from the beam pipe to prevent radiation damage during beam injection and beam dumping. Possible radiation damage of the calorimeter has been monitored since the beginning of the experiment. So far no aging effects have been observed.

Positron identification in the calorimeter is based on the fact that leptons deposit all their kinetic energy in an electromagnetic shower in the lead glass (the length of a lead glass block corresponds to 18 radiation lengths; one radiation length is the distance a particle travels while its energy falls to $1/e$ of its initial value). A hadron, on the other hand, deposits only part of its kinetic energy in the calorimeter because a hadronic shower develops

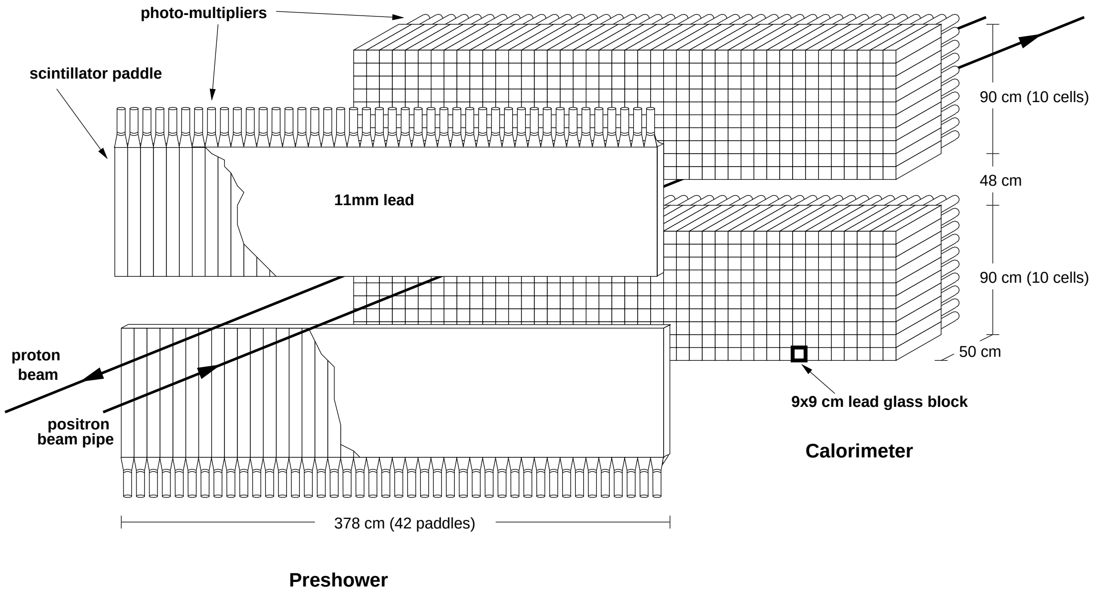

Figure 3.5: The calorimeter and the preshower detector

slower than an electromagnetic shower. (The interaction length, which is the $1/e$ length of hadronic interactions, is much larger than the corresponding electromagnetic radiation length.) Therefore positrons are identified by an E/p-ratio of one, where E is the energy deposited in the calorimeter and p the track momentum. The pion rejection is greater than 10 at the trigger level and 100 in off-line data analysis.

The Hodoscopes

There are three hodoscopes (H0, H1, and H2) in the spectrometer. Hodoscope H2 serves as a preshower detector for particle identification. A diagram of the preshower detector is shown in figure 3.5. The whole detector has an active area of almost 7 m^2. Each half is constructed from 42 vertical scintillator paddles which are 9.3 cm wide, 91 cm high, and 1 cm thick. The modules overlap by at least 2 mm to avoid holes in the acceptance. The signals are read out by photo-multiplier tubes located at the end of each module. An 11 mm thick lead plate (2 radiation lengths) is placed in front of H2. Positrons passing through the lead initiate an electromagnetic shower. The shower causes signals between 20 and 40 MeV in the scintillators. Most hadrons do not initiate showers in the preshower detector, because the lead corresponds to only 0.02 interaction length. Hadrons therefore only deposit about

1-3 MeV by ionisation energy loss. A hadron rejection factor of 10 is reached for a 95% positron detection efficiency.

In addition the preshower detector H2 is used in the trigger together with the calorimeter and the hodoscope H1. The latter is constructed in the same way as the preshower, but there is no lead in front of it. It is used to discriminate neutral and charged particles.

In 1996 another hodoscope, H0, was installed directly in front of the front drift chambers. It consists of two large scintillators and is part of the trigger. The hodoscope identifies backward going particles with a time of flight measurement when combined with the signals from the hodoscopes H1 and H2. Before the hodoscope was installed these particles, which originate from showers generated by the proton beam, met the requirements for a DIS trigger. The installation of the hodoscope eliminated these pseudo DIS events which outnumbered the positron events by a factor of up to three for a hydrogen target.

The Čerenkov Detector

Pions are identified with a threshold Čerenkov counter. The effect on which the counter is based was discovered by the Russian physicist Čerenkov in the 1930s.

Čerenkov radiation is emitted by a charged particle when it enters a medium with a velocity higher than the velocity of light c/n in that medium. The light is emitted at an angle θ given by

$$\cos\theta = \frac{1}{\beta n}. \tag{3.3}$$

Hence no light is emitted if the particle velocity is less than a threshold velocity of

$$\beta_t = \frac{1}{n}. \tag{3.4}$$

A threshold Čerenkov counter takes advantage of this phenomenon. The medium (or the radiator) is chosen so that the threshold velocity lies between the typical velocities of the two particle types to be distinguished. The fast particle emits radiation, while the slower particle traverses the detector without emitting Čerenkov radiation.

The upper half of the counter used in the HERMES experiment is shown in figure 3.6. The frame of the detector is made from aluminum. The entry and exit windows which have a size of 0.86 m^2 and 1.52 m^2 consist of double walled foils. Nitrogen is circulated in the gap between the foils to prevent air from diffusing into the radiator volume. A gas mixture

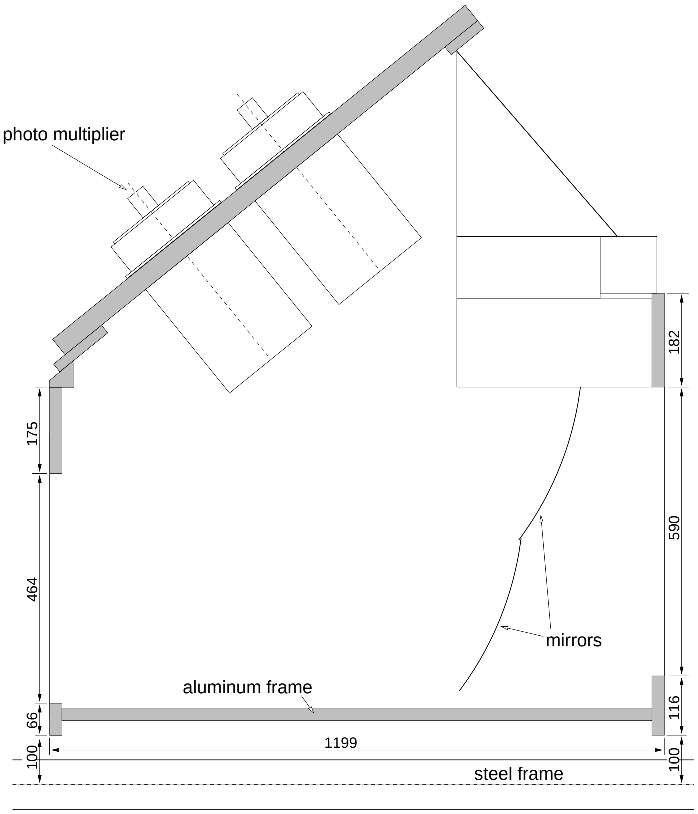

Figure 3.6: The upper half of the threshold Čerenkov detector

of 70% nitrogen and 30% perfluorobutane is used as a radiator. The advantages of a gas radiator are a refractive index near one that enables the discrimination of very fast particles and the possibility to adjust the index by varying the gas pressure. In 1996 and 1997 the gas was kept at atmospheric pressure, resulting in momentum thresholds for pions, kaons and protons of 3.8, 13.6, and 25.8 GeV, respectively.

A set of 20 spherical mirrors focuses the emitted Čerenkov light on a set of photomultiplier tubes. Each tube has a diameter of 12.7 cm and is preceded by a Hinterberger-Winston light cone to maximise the light collection.

In 1998 the threshold Čerenkov counter was upgraded to a ring imaging Čerenkov detector (RICH). This detector allows for the identification of pions, kaons and other hadrons, mostly protons. The identification software is implemented at the present time.

The Transition Radiation Detector

The transition radiation detector (TRD), which is installed behind the Čerenkov counter and the back chambers, provides important information for the identification of leptons and hadrons.

Transition radiation can be thought of as similar to bremsstrahlung, which is radiated when a charged particle is decelerated. Here the velocity of the particle remains the same, but it traverses two media with different dielectric constants. The particle induces a given electromagnetic polarisation in the first material. When the particle crosses the boundary to the second material, the polarisation is adjusted to the different dielectric properties of the second medium. Transition radiation is emitted during this process, because of the sudden change of the electric fields associated with the different polarisations in the two media [29].

The total energy emitted as transition radiation depends linearly on the Lorentz factor γ:

$$W = \frac{2}{3}\,\alpha\,\omega_p\,\gamma, \tag{3.5}$$

where α is the fine structure constant and ω_p the plasma frequency of the medium. Particles with $\beta \approx 1$ can therefore be distinguished by their Lorentz-factor γ, which is for example 27 for a 27 GeV proton, but about 53,000 for a 27 GeV electron.

Transition radiation is emitted around the particle trajectory with an opening angle $\theta \approx \frac{1}{\gamma}$. At high energies the radiation, mainly consisting of X-rays, is therefore emitted almost in the same direction as the particle track. Experimentally this poses a problem to the detection of transition radiation because it is difficult to distinguish the photon from the charged particle.

In addition the intensity of transition radiation is low. This is usually solved by constructing a radiator with many consecutive foils, providing many transitions. The foils must be thicker than the formation zone, the thickness necessary to fully develop the induced electromagnetic field. The radiation emitted from the foils interferes constructively if the foils are separated by the right distance resulting in a larger intensity.

The HERMES transition radiation detector (cf. figure 3.7) is split into six modules above and six modules below the beam pipes. An individual module has an active area of $72.4 \times 325\,\mathrm{cm}^2$. Each module consists of a radiator that initiates the transition radiation and a multi-wire proportional chamber (MWPC) to detect it. Each radiator is 6.35 cm thick and

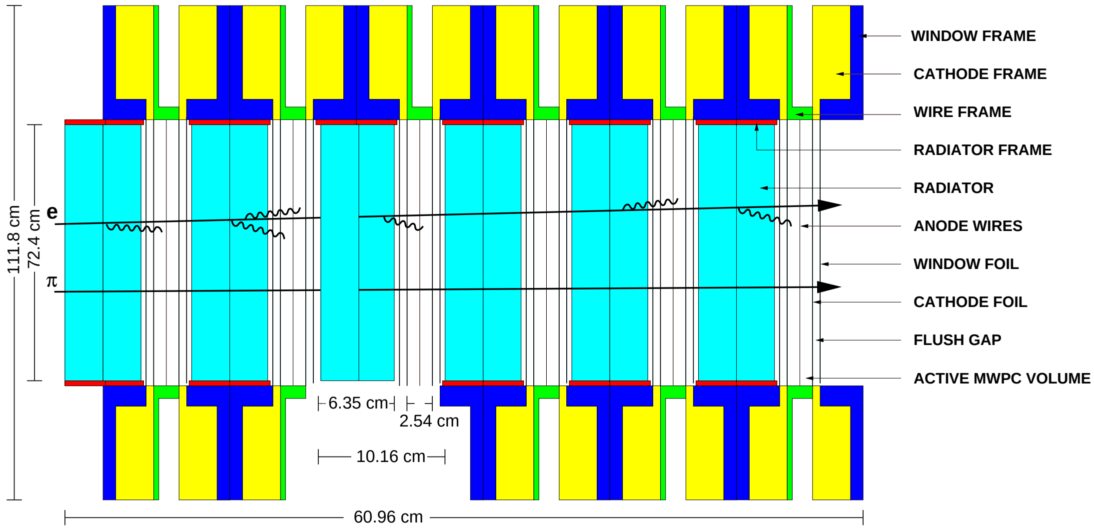

Figure 3.7: The upper half of the transition radiation detector

has approximately 267 active layers. Instead of foils, fibers are used in the radiator because it is impossible to keep the distance between a set of foils constant in a TRD as large as the one used in the HERMES experiment. The diameter of the fibers is 17-20 μm.

The transition radiation produced in the radiator is detected by the following MWPC. The anode wires in the 2.54 cm thick MWPC are made of a gold-coated Be-Cu alloy. There are 256 wires separated by 1.27 cm in each chamber. The cathode planes are at ground potential and the anode wires are at a voltage of 3100 V to collect secondary electrons in the gas within 1 μs, the time window provided by the readout electronics. The frames that hold the wires and the cathode foils were pre-stressed during assembly to achieve a uniform wire and foil tension. The tension of the cathode foils is very high to make the gas volume that is defined by the foils less sensitive to changes in gas pressure. A mixture of 90% xenon and 10% methane is used as detector gas because it efficiently absorbs X-rays.

Every charged particle ionises the chamber gas when it passes through the proportional chamber causing an electrical pulse. In addition to this energy loss, positrons emit transition radiation when they traverse the radiator which adds to the energy deposited in the MWPC. Because hadrons do not emit transition radiation at HERMES energies, positrons can be separated from hadrons by their larger signal in the proportional chamber. This technique circumvents the problem of distinguishing the transition radiation photon and the positron in the chamber.

The pion rejection factor that is achieved by summing up the responses of the single modules can be increased, if the truncated mean of the six modules is taken. In this method the largest signal that was detected for a given track in the modules is discarded. The signals of the other modules are averaged. The tail of the hadronic response that is generated by the rare production of highly energetic knock-on electrons is significantly reduced but the mean of the positron signals is hardly decreased. The result is a better separation of the hadronic and the leptonic peak, yielding a pion rejection factor of about 70 for a 90% positron efficiency.

The pion rejection factor becomes even larger, if a probability based approach is taken. The detector response for a given track is compared with the expected response for hadrons and leptons (cf. chapter 4). A probability is then determined that the particle is a hadron or a lepton. The achieved pion rejection factor is significantly larger for the same positron efficiency.

3.3.4 The Luminosity Monitor

A small calorimeter near the beam pipe between the two lead-glass calorimeter halves measures the luminosity using the cross section for Bhabha scattering ($e^+ e^- \rightarrow e^+ e^-$) and electron-positron annihilation ($e^+ e^- \rightarrow \gamma\gamma$) [1]. The calorimeter consists of an array of 3×4 Čerenkov crystals on each side of the beam-pipe which are very radiation resistant to minimise aging effects. Furthermore, radiation damage due to the close proximity to the beam is prevented by moving the monitor away from the beam-pipe during injection and dumping.

Bhabha scattering and electron annihilation are distinguished from background events by requiring a coincident signal in both detector halves. Background events usually only produce a large signal in one of the blocks. Coincidence rates of 132 Hz have been measured at a beam current of 20 mA and a target density of $1 \cdot 10^{15}$ nucleons/cm^2.

3.4 The Trigger

The HERMES trigger was designed to select deep inelastic scattering events from a large number of background events. The trigger decision is made online within 400 ns of the

[1] Møller scattering ($e^- e^- \rightarrow e^- e^-$) in the case of an electron beam.

interaction. The trigger initiates readout of the electronics and storage of the information on disk.

The trigger uses signals from the three hodoscopes (H0, H1, and H2), the calorimeter, and the accelerator bunch signal (the HERA clock). A signal in the hodoscope H0 ensures that the event is not caused by backward going particles originating from the proton beam. Together with H1, the hodoscope H0 also rejects neutral particle background; this is especially important for the discrimination of photons and electrons.

Charged background is suppressed with the calorimeter by requiring a signal coincident with the HERA clock that is larger than the calorimeter threshold. In 1995 and the beginning of 1996 this threshold was set to 3.5 GeV. In the rest of 1996 and 1997 the threshold was lowered to 1.4 GeV. The high threshold rejects charged hadron background by a factor of 10. The low threshold was chosen in 1996 to increase the range of the inelasticity parameter y from 0.85 to 0.95 in order to increase the acceptance at low x_{bj}.

3.5 Data Acquisition

Once the trigger selects an event, the data acquisition system records the information available from the detectors. In 1996 the acquisition system was able to record up to 150 events per second. In 1996 and 1997 the positron and the proton beam were often stable for 8-12 hours after injection. During this *fill* the data are written to 9 GB disks; they are transferred to the DESY main storage site after the beam is dumped. The fill is split up into *runs* which last about 10 minutes. Each run divides up into *bursts* defined by the scalar reads, during which certain variables, for example the target polarisation, stay constant. A burst is roughly 10 seconds long.

Chapter 4

Particle Identification

4.1 Introduction

Particle Identification (PID) is essential in the HERMES experiment to distinguish different particle types from each other. Primarily, positrons have to be distinguished from hadrons to identify the scattered particle in deep inelastic scattering events. In addition pions have to be discriminated from other hadrons in order to determine the polarised valence quark distributions with the method described in section 2.4. Particle identification relies on the fact that different particle types cause different signals in PID detectors. There exist various methods to take advantage of this. The simplest procedure is to divide the spectrum of a given detector into a number of intervals and assign each interval to a certain particle type, according to its typical detector response.

The truncated mean spectrum of the TRD modules is an example where this discrimination method can be applied easily. The spectrum is shown in figure 4.1. The dotted and the dashed lines show the contributions by positrons and hadrons, respectively. Reasonable cuts to discriminate the two particle types are indicated at 21.8 keV and 17.5 keV. Particles with signals above 21.8 keV are identified as positrons, particles below 17.5 keV as hadrons. Positrons with signals below 17.5 keV are misidentified as hadrons whereas hadrons above 21.8 keV are misidentified as positrons.

The discriminating power of a PID system is often described by the *hadron rejection factor* (HRF), defined as the number of all hadrons divided by the number of hadrons misidentified as leptons. The HRF depends on the ratio of the identified positrons to all positrons

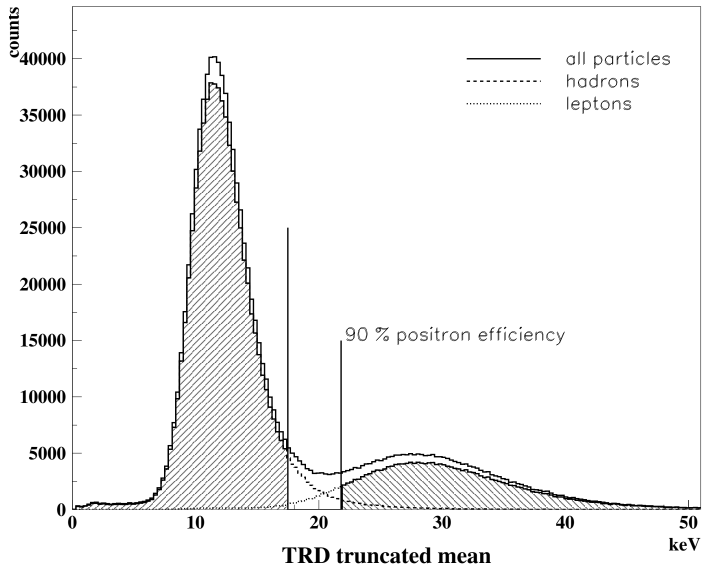

Figure 4.1: TRD truncated mean for data taken in 1996 with the high calorimeter threshold. The shaded areas indicate the particles that are identified as hadrons and leptons, respectively.

in the sample, referred to as the *positron efficiency*. The truncated mean of the TRD for the sample shown in figure 4.1 provides an HRF of about 70 at 90% positron efficiency.

More efficient is a probability based procedure. For each particle type a probability that the measured detector signal was caused by this particle is calculated. The probability is calculated by comparing the signal with *parent distributions* which are the typical responses of the different particle types in the detector. In comparison to the simple cuts described in the previous paragraph this procedure yields a better hadron rejection for the same positron efficiency.

A difficulty that arises is the determination of the parent distributions. It is possible to calculate them from first principles, but the theoretical models that are applied are often complex and the resulting parent distributions do not describe the actual detector spectra sufficiently well. Another way is to determine the parent distributions from data that have been collected. The parent distributions for the different particle types are found by imposing restrictions on other measured quantities to identify one specific particle type. In this chapter the generation of such parent distributions is explained, the performance of the PID system is investigated with a Monte Carlo simulation, and the resulting probability distributions are discussed. Furthermore the Monte Carlo data are compared to a previous model which used less accurate parent distributions.

4.2 Probability Analysis

The probability analysis used for particle identification in the HERMES experiment is based on the comparison of probabilities that a measured detector response E was caused by particles of different types A_i. This *conditional probability* $P(A_i|E)$ is related through *Bayes's theorem* to the conditional probability $P(E|A_i)$ that a particle of a given type A_i causes a detector response E [30, 31]:

$$P(A_i|E) = \frac{P(A_i) \cdot P(E|A_i)}{\sum_{k=1}^{n} P(A_k) \cdot P(E|A_k)}, \tag{4.1}$$

where the sum runs over all particle types A_k and $P(A_i)$ is the probability that a particle of type A_i is present in the detector.

The conditional probability $P(E|A_i)$ for a given detector D is equivalent to the *parent distribution* $\mathcal{L}_D^i$ that depends on the particle type, the detector response E, and the momentum p of the particle:

$$\mathcal{L}_D^i \equiv \mathcal{L}_D^i(E, p). \tag{4.2}$$

The probability $P(A_i)$ is given by the normalized flux ϕ^i which depends on the momentum p and the scattering angle θ:

$$P(A_i) = \phi^i \equiv \phi^i(p, \theta). \tag{4.3}$$

The conditional probability $\mathcal{P}^i \equiv P(A_i|E)$, that a certain particle type has been observed, can be determined from the detector response using Bayes's theorem if the parent distributions and the particle fluxes are known. The parent distributions can be extracted from collected data or theoretical models (cf. section 4.4).

In the HERMES experiment the PID detectors are used mainly to discriminate two particle types: positrons e and hadrons h. In this case the probabilities $\mathcal{P}_D^e$ and $\mathcal{P}_D^h$ are

$$\mathcal{P}_D^e = \frac{\mathcal{L}_D^e}{\Phi\, \mathcal{L}_D^h + \mathcal{L}_D^e} \qquad \mathcal{P}_D^h = \frac{\mathcal{L}_D^h}{\mathcal{L}_D^h + \Phi^{-1}\, \mathcal{L}_D^e}, \tag{4.4}$$

where $\Phi \equiv \phi^h/\phi^e$ is the flux ratio of hadrons and positrons.

The probabilities $\mathcal{P}_D^e$ and $\mathcal{P}_D^h$ are however not used explicitly for particle identification in order to avoid the determination of the particle fluxes ϕ^h and ϕ^e which can only be done with a Bayesian iteration [32]. Rather, the logarithm of the ratio of the positron and the hadron probabilities for a given detector D is calculated:

$$\log_{10}\frac{\mathcal{P}_D^e}{\mathcal{P}_D^h} = \log_{10}\frac{\mathcal{L}_D^e}{\Phi\mathcal{L}_D^h} = \log_{10}\frac{\mathcal{L}_D^e}{\mathcal{L}_D^h} - \log_{10}\Phi, \tag{4.5}$$

and the last term is ignored. Positrons and hadrons are distinguished with the quantity PID defined by

$$\mathrm{PID_D} \equiv \log_{10}\frac{\mathcal{L}_D^e}{\mathcal{L}_D^h}. \tag{4.6}$$

In principle a particle with a negative PID value is more likely to be a hadron, whereas a particle with a positive value has a higher probability to be a positron. However, neglecting the flux ratio $\log_{10}\Phi$ causes a shift of the PID spectrum which depends on the momentum p and the angle θ of the detected particle. Therefore a momentum dependent cut has to be applied to discriminate hadrons and leptons if the flux factor is neglected in the PID spectrum. In practice it is sufficient to use momentum independent cuts, if these are imposed at PID values smaller than zero for hadrons and larger than the minimum in the PID spectrum for leptons. (The probabilities for a hadron and a lepton are assumed to be equal for a PID value between zero and the minimum of the PID spectrum.) Momentum dependent deviations of the probabilities at the cuts are then small enough to be ignored.

A better discrimination between the particle types is achieved when the probabilities of several detectors are combined. As a result an overall PID value can be defined:

$$\mathrm{PID} = \log_{10}\left(\prod_D \frac{\mathcal{L}_D^e}{\mathcal{L}_D^h}\right) = \sum_D \left(\log_{10}\frac{\mathcal{L}_D^e}{\mathcal{L}_D^h}\right). \tag{4.7}$$

In the HERMES experiment the calorimeter, the preshower detector, the Čerenkov detector, and the TRD yield the PID distributions $\mathrm{PID_{Cal}}$, $\mathrm{PID_{Pre}}$, the $\mathrm{PID_{Cer}}$, and $\mathrm{PID_{TRD}}$. $\mathrm{PID_{TRD}}$ is commonly referred to as PID5. This quantity is calculated from the single PID values of the six TRD modules,

$$\mathrm{PID5} = \log_{10}\left(\prod_{i=1}^{6} \frac{\mathcal{L}_{TRD_i}^e}{\mathcal{L}_{TRD_i}^h}\right). \tag{4.8}$$

Furthermore the quantities PID2 and PID3 are defined as

$$\begin{aligned} \mathrm{PID2} &= \mathrm{PID}_{\mathrm{Cal}} + \mathrm{PID}_{\mathrm{Pre}} = \log_{10} \frac{\mathcal{L}^e_{Cal} \cdot \mathcal{L}^e_{Pre}}{\mathcal{L}^h_{Cal} \cdot \mathcal{L}^h_{Pre}} \\ \mathrm{PID3} &= \mathrm{PID}_{\mathrm{Cal}} + \mathrm{PID}_{\mathrm{Pre}} + \mathrm{PID}_{\mathrm{Cer}} = \log_{10} \frac{\mathcal{L}^e_{Cal} \cdot \mathcal{L}^e_{Pre} \cdot \mathcal{L}^e_{Cer}}{\mathcal{L}^h_{Cal} \cdot \mathcal{L}^h_{Pre} \cdot \mathcal{L}^h_{Cer}}. \end{aligned} \tag{4.9}$$

4.3 Monte Carlo Techniques

The Monte Carlo simulation that was used to investigate the performance of the PID system is based on the generated parent distributions. In addition to its use for the optimisation of these parent distributions, the simulation can be used to produce Monte Carlo data for further analysis. For the latter purpose several parameters of the Monte Carlo were tuned to improve the simulation of the PID detectors.

Two different techniques are used in the Monte Carlo to randomly generate events from the parent distributions, the *transformation method* and the *rejection method* [33]. The goal of each method is to generate the events as random samples of a specific generally non-constant probability distribution f (the parent distribution) with the help of a *uniform distribution* (a uniform distribution is implemented in most compilers as a random number generator). By definition the probability density distribution of a uniform distribution is normalised and constant between 0 and 1:

$$p(r) = \begin{cases} 1 & \text{for } 0 \leq r \leq 1 \\ 0 & \text{otherwise,} \end{cases} , \tag{4.10}$$

$$\int_{-\infty}^{\infty} p(r)\, dr = \int_0^1 1\, dr = 1. \tag{4.11}$$

The uniform distribution can be extended to any interval $[a, b]$ with the transformation

$$p'(r) = (b - a) \cdot p(r) + a. \tag{4.12}$$

The new distribution $p'(r)$ is constant between a and b.

The Rejection Method

In this method a pair of random numbers is generated to create a single random number drawn from the specific distribution f. The first random number x is drawn from a uniform

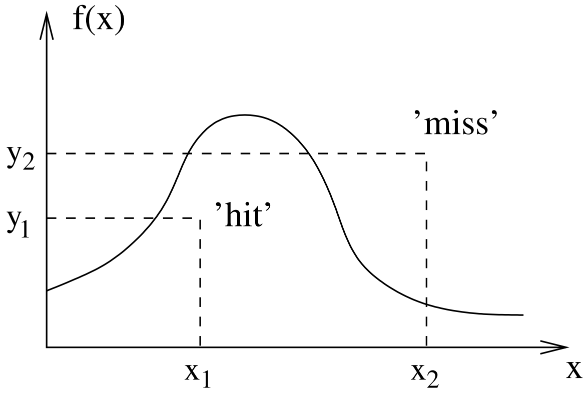

Figure 4.2: The rejection method

distribution $p'(r)$ (eq. (4.12)) in the range $[x_1, x_2]$ of the distribution f. The second number y is drawn such that it lies in the range $[\min\{f(x)\}, \max\{f(x)\}]$. By comparing the two values $f(x)$ and y, it is determined whether the value x is a *hit* or a *miss*: $y \leq f(x)$ is a hit and $y > f(x)$ is a miss (cf. figure 4.2.) The set of hits x constitutes the set of random numbers drawn from the specific distribution f.

The Transformation Method

Different from the rejection method, the transformation method only requires the generation of one random number r drawn from a uniform distribution. The random number is compared with the integrated and normalised specific distribution to find the random number x drawn from the specific distribution. Let $\tilde{f}$ be the normalised distribution,

$$\tilde{f}(x) = \left[\int_{x_{min}}^{x_{max}} f(x')\, dx' \right]^{-1} f(x) \tag{4.13}$$

and F the integrated distribution,

$$F(x) = \int_{x_{min}}^{x} \tilde{f}(x')\, dx'. \tag{4.14}$$

Then the random number x drawn from the specific distribution is determined by the equation

$$x = F^{-1}(r). \tag{4.15}$$

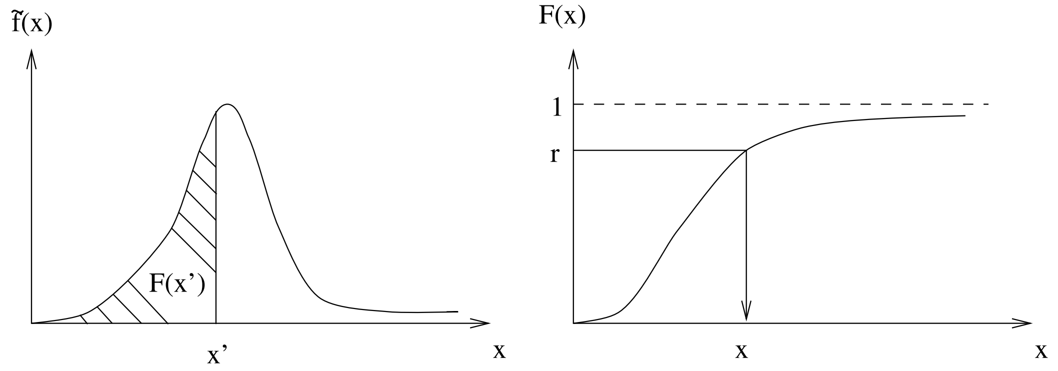

Figure 4.3: The transformation method

The method is illustrated in figure 4.3. The transformation method is more efficient than the rejection method, because every generated number is a hit and only one random number has to be generated for each event. However, the rejection method has a better resolution, if the integrated distribution $F(x)$ is very flat.

4.4 The Parent Distributions

A *parent distribution* determines the probability of finding a given detector response in a measurement [33]. The parent distributions for the four PID detectors and the particle momenta were used as input for the Monte Carlo simulation and as reference distributions for the calculation of the PID values.

It is imperative to produce accurate parent distributions in order to allow for a precise simulation of the detector responses. Theoretical models can be used to calculate the parent distributions, but the theoretical description of a particle detector and the interactions of different particle types with the detector material is usually complex. Therefore the resulting parent distributions often lack sufficient accuracy to describe the true probability distributions of the detector responses for the different particle types.

Another way is to extract the parent distributions from collected data. In principle the exact determination of a parent distribution is only possible if the particle types can be discriminated exactly and an infinite number of measurements are available. However, the parent distribution for a given particle type is approximated if a large number of measure-

Detector	Range	
	Leptons	Hadrons
Calorimeter (E/p)	$0.92 < E/p < 1.10$	$E/p < 0.80$
Preshower [MeV]	$0.025 < E_{Pre}$	$E_{Pre} < 0.004$
Čerenkov ($\mathrm{N_{pe}}$)	$1.4 < \mathrm{N_{pe}}$	$\mathrm{N_{pe}} < 0.2$
TRD [keV]	$26.0 < E_{TRD}$	$E_{TRD} < 14.0$

Table 4.1: Medium cuts (In case of the calorimeter the cut is given in terms of the ratio of deposited energy and the particles momentum and in case of the Čerenkov the cut is given in terms of the mean number of photoelectrons detected.)

ments are available and a sufficiently clean sample of the particle type can be extracted from the data set.

The parent distributions described in this thesis for PID analysis and the Monte Carlo were extracted from data collected in 1996. The clean data samples for the two particle types and the four detectors were generated by imposing restrictive cuts on the PID detectors other than the one being studied. This technique relies on the assumption that the detector responses for a given particle type are uncorrelated. It is therefore assumed that for example the cuts on the calorimeter do not bias the parent distributions of the other three detectors. The restrictive cuts will be referred to as *medium cuts* according to their definition in [30]. The values are given in table 4.1 and the cuts are shown in figure 4.4. The cuts are a compromise between a very clean data sample and high statistics. For example the positron cut for the TRD yields a hadron rejection factor of over 200, but only about 70% of the positrons are identified.

The parent distributions depend not only on the detector response but also on the momentum of the particle. To account for this, the parent distributions were divided into several momentum bins. The number and the size of the bins is a compromise between the momentum resolution of the spectrometer and the minimisation of the number of bins to achieve reasonable statistics and to reduce memory usage and computing time in the Monte Carlo and in PID analysis. Different momentum bins were chosen for each of the four detectors and the two particle types to account for the varying momentum dependences of the parent distributions (see figure 4.5).

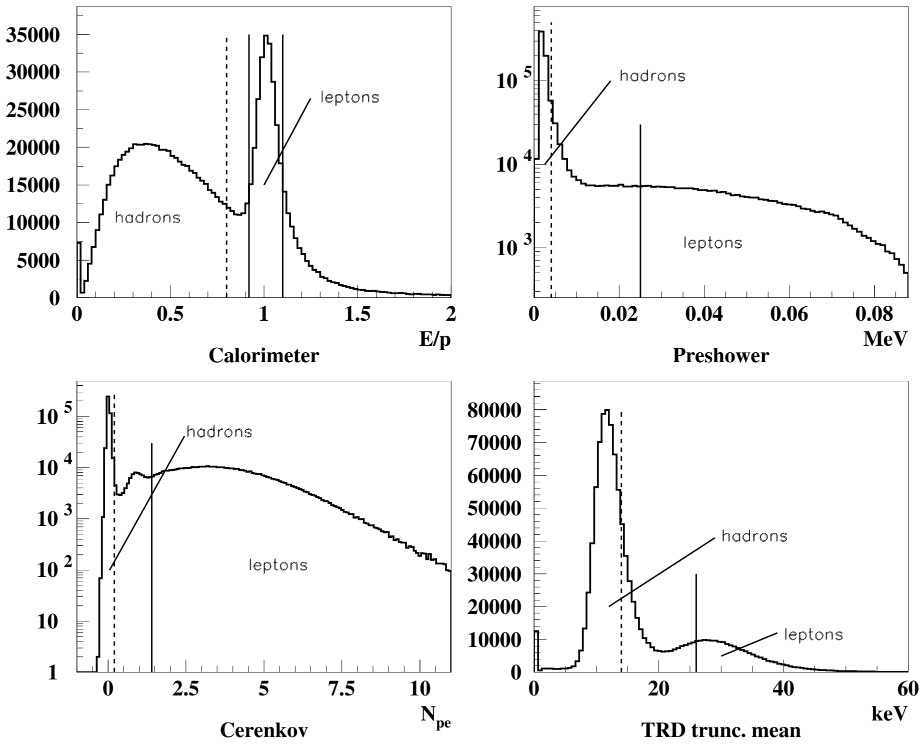

Figure 4.4: The cuts that were used to determine the clean particle samples for hadrons and leptons in the determination of the parent distributions.

The data from which the clean particle samples were extracted are semi-inclusive deep inelastic scattering data. Only events that passed the deep inelastic scattering trigger (see section 3.4) contributed to the samples. The resulting parent distributions are therefore not the probability distributions for the true detector responses, but rather describe spectra of the PID detectors that are modified by the DIS trigger. Furthermore two sets of parent distributions had to be produced, one for the high and one for the low calorimeter threshold in the HERMES trigger. On the other hand an advantage of the extraction of parent distributions from DIS data is that it is not necessary to simulate the deep inelastic scattering trigger in the Monte Carlo.

A number of 200 response bins was chosen for the parent distributions of all four detectors to simplify the Monte Carlo and the PID routines and to provide a reasonable computation time while accounting for the energy resolution of the detectors. The specific properties of the

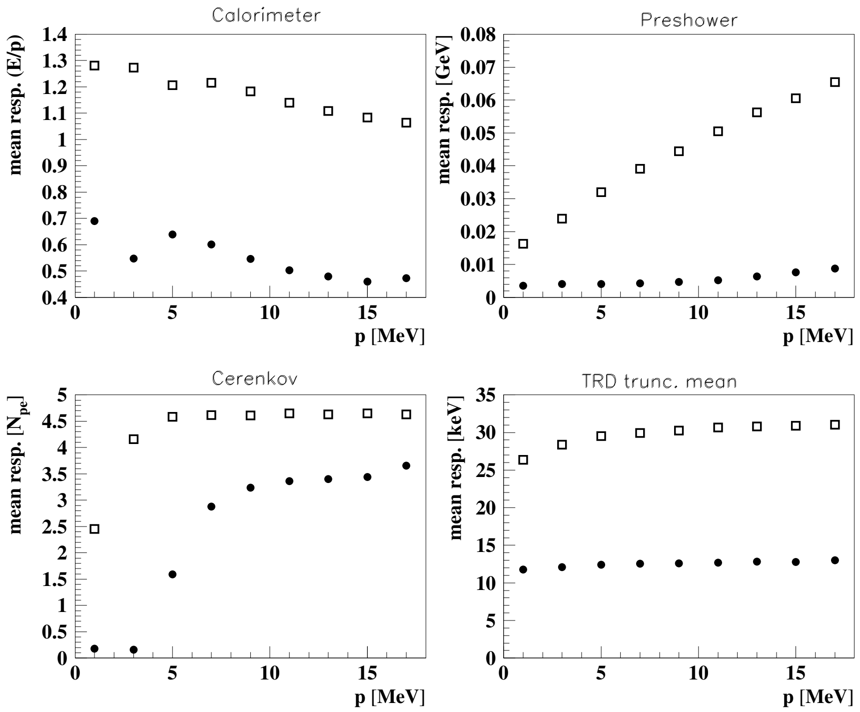

Figure 4.5: The mean detector responses as a function of momentum (1996 data high calorimeter threshold). The squares are leptons, the circles hadrons.

parent distributions for the four particle identification detectors and the parent distributions for the momentum are discussed in the following sections.

The TRD Distributions

The TRD parent distributions for leptons were divided into five momentum bins and the distributions for hadrons into six bins. They were generated individually for each module. The ranges of the momentum bins are given in table 4.2. The bins are the same for both the low and high calorimeter threshold because the TRD response does not depend strongly on the chosen threshold.

The range of the response was chosen to be 0 to 250 keV. In addition to a normal TRD response, values above 200 keV were included where the TRD readout overflows. It follows from this range and the number of response bins that a bin is 1.25 keV wide.

	Čerenkov		TRD	
Bin	Leptons	Hadrons	Leptons	Hadrons
1	0 - 4.4 GeV	0 - 1 GeV	0 - 6 GeV	0 - 2 GeV
2	4.4 - 10	1 - 4	6 - 12	2 - 4
3	10 - 17	4 - 4.4	12 - 18	4 - 6
4	17 - 30	4.4 - 5	18 - 23	6 - 8
5		5 - 6	23 - 30	8 - 10
6		6 - 8		10 - 30
7		8 - 10		
8		10 - 12.5		
9		12.5 - 15		
10		15 - 30		

Table 4.2: Momentum bins for the Čerenkov and the TRD parent distributions

Only medium cuts on the preshower detector and the calorimeter were used for the extraction of the clean particle samples, because the Čerenkov cut was found to cause a significant difference between the PID5 spectrum of the Monte Carlo and the PID5 spectrum of the data. This is shown in figure 4.6.

As mentioned above, the four PID detectors were assumed to be uncorrelated. A possible reason for the shift of the hadron peak in the PID5 distributions is that this assumption is wrong and that there is a correlation between the TRD and the Čerenkov detector. However a scatter-plot of the Čerenkov response and the response of the first TRD module shown in figure 4.7 reveals no significant correlation between the two detectors.

Despite this, it is likely that there is a subtle correlation induced by the cuts that causes the differences in the hadron peak of the PID5 spectrum. The Čerenkov cut for hadrons is placed so that pions with momentum above the Čerenkov threshold for pions of 3.8 GeV are not included in the clean hadron samples for the parent distributions. Therefore it is expected that the TRD spectra generated with and without cuts are the same for momenta below this threshold. This agreement was verified by the Monte Carlo simulations and is illustrated in the left plot of figure 4.8. The right hand plot in figure 4.8 shows TRD truncated mean spectra in a momentum bin above the pion Čerenkov threshold, 6 GeV to 8 GeV. The TRD spectrum generated with a Čerenkov cut is shifted from the spectrum

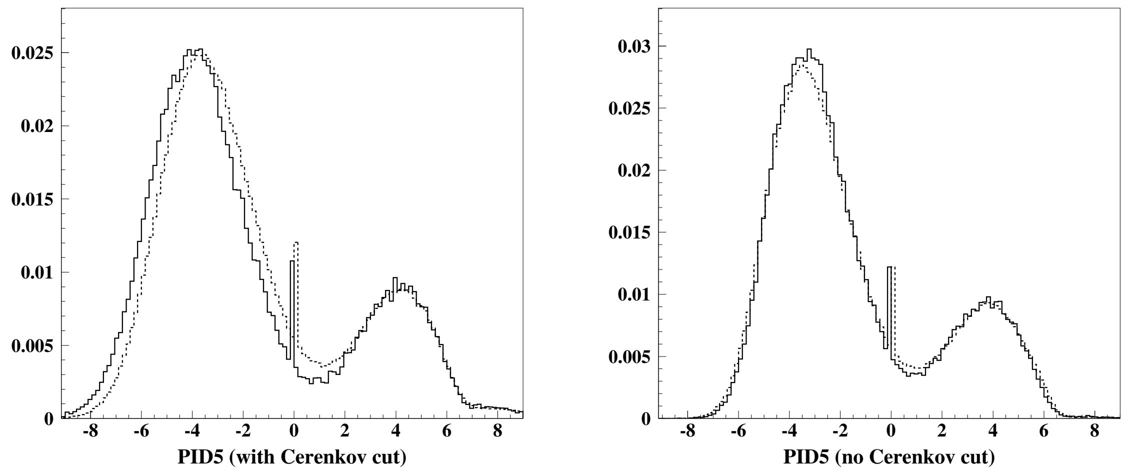

Figure 4.6: Comparison of Monte Carlo data generated using parent distributions with a Čerenkov cut (left) and without a Čerenkov cut (right). The dashed line is 1996 data (high calorimeter threshold).

generated from the data. If pions with momenta above the Čerenkov threshold cause this shift, they must deposit more energy in the TRD modules than other hadrons. Figure 4.9 illustrates the TRD truncated mean for pions and heavier hadrons with momenta between 7 and 9 GeV, well above the pion threshold at 3.8 GeV. The pion peak is in fact shifted from the peak of the other hadrons towards higher energy deposition. Gaussian fits of the two peaks show that in this momentum range pions deposit a mean energy of $(12.13 \pm 1.94)\,\mathrm{keV}$ in the TRD whereas heavier hadrons deposit on average only $(10.57 \pm 1.85)\,\mathrm{keV}$. The ratio $R = 1.15 \pm 0.27$ agrees within the error-bars with the ratio of the expected ionisation energy loss of pions and protons in Xenon: $R = 1.29 \pm 0.04$ [34]. Therefore the differences in the TRD spectra in figure 4.8 are caused by the exclusion of pions with momenta above the Čerenkov threshold.

This effect shifts the PID5 spectrum as shown in figure 4.6 because the probabilities are calculated with incorrect parent distributions. In the data, a hadron causes on average a larger signal in the TRD than is expected by parent distributions generated with the Čerenkov cut. Therefore it looks more like a lepton and has a higher PID5 value. The hadron peak in the Monte Carlo generated PID5 spectrum is shifted to lower PID5 values because the same parent distributions were used to generate the hadron response in the first

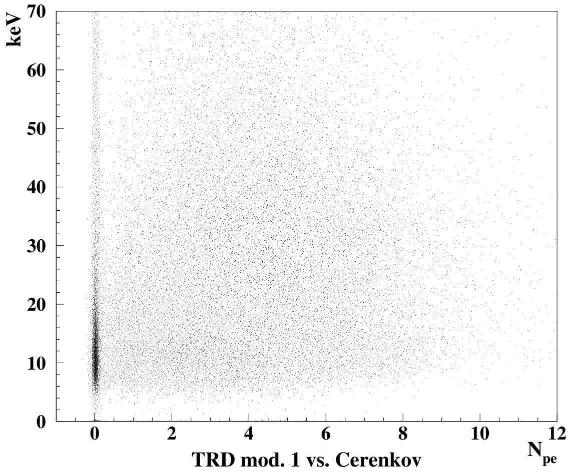

Figure 4.7: Two-dimensional plot of the TRD module 1 response in keV versus the number of photoelectrons detected in the Čerenkov counter (1996 data fill 57).

place.

Two sets of parent distributions, one for each calorimeter threshold in the trigger, were generated to account for the different TRD response for each threshold. Generally the response is independent of the calorimeter threshold, but the spectra for the high threshold differ from those for the low threshold because of the different particle fluxes of the two data sets and the finite number of momentum bins. This causes small differences of the fluxes within the bins and results in small shifts of the hadron peak in the TRD response. Therefore the PID spectrum is shifted if parent distributions averaged over both thresholds are used.

The Čerenkov Distributions

The momentum bins for the Čerenkov counter are also given in table 4.2. Only four momentum bins for the lepton parent distributions were needed because the mean number of photons emitted by an electron in the counter is almost independent of the momentum (cf. figure 4.5). The Čerenkov response varies significantly up to 6 GeV because of the threshold of 3.8 GeV for pions. Small bins in this range were chosen to account for the strong momentum dependence at the threshold.

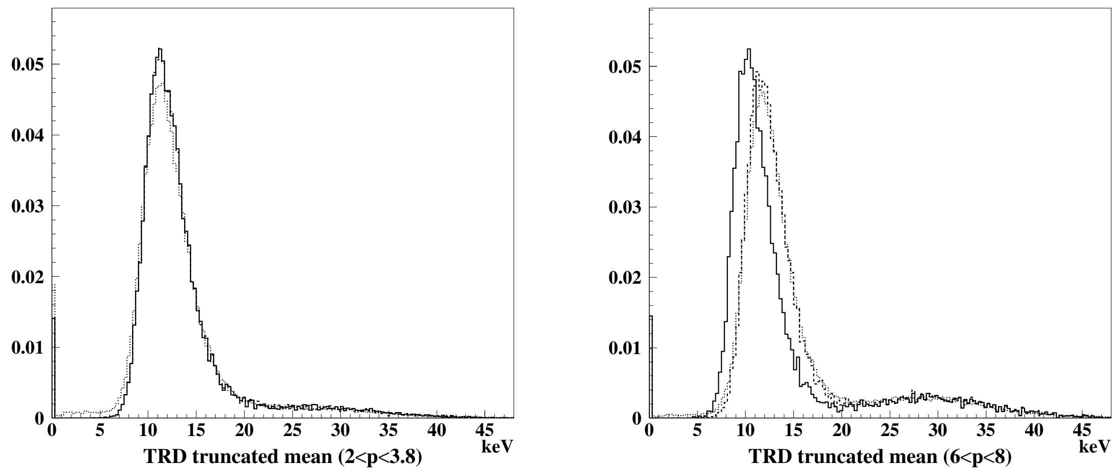

Figure 4.8: Comparison of TRD truncated mean spectra using parent distributions with Čerenkov cut and without Čerenkov cut in two different momentum bins. The solid line is Monte Carlo data calculated from parent distributions with Čerenkov cut and the dashed line is Monte Carlo data from parent distributions without Čerenkov cut. The dotted line is 1996 data (high calorimeter threshold). (In the left plot both Monte Carlos calculate the same TRD response, whereas in the right plot only the parent distribution without Čerenkov cut agrees with the data.)

Cuts on the TRD, the calorimeter, and the preshower detector given in table 4.1 were used to extract the clean data samples for positrons and hadrons from data taken in 1996. With these cuts, parent distributions for each of the two calorimeter thresholds were generated. Similarly to the TRD responses small differences in the Čerenkov response for the two thresholds are caused by varying particle fluxes and the finite number of momentum bins. The parent distributions have a range of (-1) to 15 N_{pe}. The size of a response bin is therefore 0.08 N_{pe}. The range includes the electron tail and a negative region. The 'response' of the Čerenkov is in fact negative for some events because of the pedestal that is subtracted from the response in online analysis and the finite resolution of the detector.

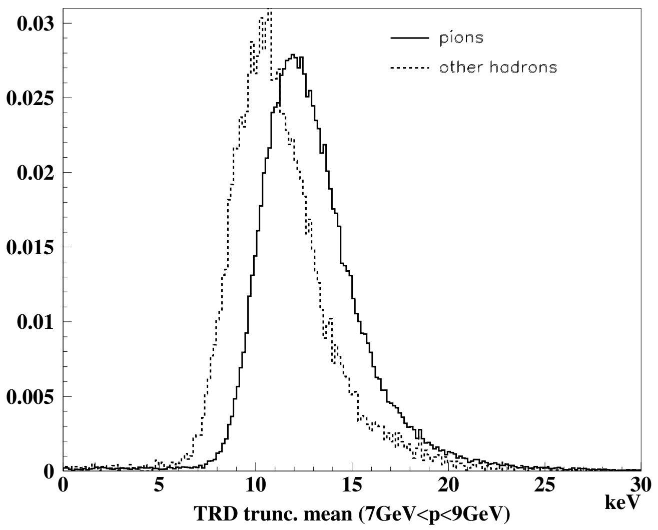

Figure 4.9: TRD truncated mean response of pions (solid line) and other hadrons (dashed line); 1996 data, high calorimeter threshold.

The Calorimeter Distributions

The hadron and positron parent distributions for the calorimeter were divided into different momentum bins for the two calorimeter thresholds. The bins are listed in table 4.3. The range of the detector response for the parent distributions is 0 to 4 in units of the ratio (E/p). This range contains hadrons with values mostly below 0.9, the lepton peak at 1 and a long tail for $E/p > 1.0$. The width of a response bin is 0.02.

The parent distributions were extracted from data using only cuts on the preshower detector and the TRD. The two cuts provided a sufficient cleanliness of the particle samples because of the high discrimination efficiency of the TRD. Unlike for the TRD parent distributions no differences between parent distributions with and without a Čerenkov cut were observed. However, the Čerenkov cut was not applied in order to include the pions mentioned in the discussion of the TRD parent distributions.

	Threshold 1.4 GeV		Threshold 3.5 GeV	
Bin	Leptons	Hadrons	Leptons	Hadrons
1	0 - 2.5 GeV	0 - 1.0 GeV	0 - 2.0 GeV	0 - 1.0 GeV
2	2.5 - 3.5	1.0 - 1.5	2.0 - 3.0	1.0 - 1.5
3	3.5 - 4.5	1.5 - 2.0	3.0 - 5.0	1.5 - 2.0
4	4.5 - 6.5	2.0 - 4.0	5.0 - 7.0	2.0 - 3.0
5	6.5 - 8.5	4.0 - 5.0	7.0 - 10.0	3.0 - 3.5
6	8.5 - 30.0	5.0 - 7.0	10.0 - 30.0	3.5 - 4.0
7		7.0 - 10.0		4.0 - 4.5
8		10.0 - 30.0		4.5 - 5.0
9				5.0 - 6.0
10				6.0 - 7.0
11				7.0 - 8.0
12				8.0 - 9.0
13				9.0 - 30.0

Table 4.3: Momentum bins for the calorimeter parent distributions

The Preshower Distributions

A range for the preshower parent distributions from 0 to 0.22 GeV was chosen to contain the hadron peak close to zero and the electron tail up to about 0.1 GeV. Furthermore an overflow region above 0.1 GeV was included in the response range. It follows from the number of response bins of 200 that the width of each bin is 1.1 MeV.

The momentum bins for the parent distributions are given in table 4.4. The hadron response is almost independent of the momentum, thus only four bins were chosen for the low calorimeter threshold and three bins for the high calorimeter threshold. The stronger momentum dependence of the positron response was accounted for by choosing nine bins for the positron parent distributions. The two particle types were discriminated by imposing cuts on the calorimeter and the TRD. Similarly to the TRD and the Calorimeter parent distributions the Čerenkov counter was not used to produce the clean particle samples.

	Threshold 1.4 GeV		Threshold 3.5 GeV	
Bin	Leptons	Hadrons	Leptons	Hadrons
1	0 - 1.5 GeV	0 - 2.5 GeV	0 - 1.5 GeV	0 - 3.0 GeV
2	1.5 - 2.0	2.5 - 6.0	1.5 - 2.0	3.0 - 8.5
3	2.0 - 2.5	6.0 - 9.0	2.0 - 2.5	8.5 - 30.0
4	2.5 - 3.0	9.0 - 30.0	2.5 - 3.0	
5	3.0 - 4.0		3.0 - 4.0	
6	4.0 - 6.0		4.0 - 6.0	
7	6.0 - 8.5		6.0 - 8.5	
8	8.5 - 12.0		8.5 - 12.0	
9	12.0 - 30.0		12.0 - 30.0	

Table 4.4: Momentum bins for the preshower parent distributions

The Momentum Distributions

Parent distributions for the particle momentum are only necessary for the Monte Carlo simulation. The distributions for hadrons and leptons were extracted from data with a cut on the PID spectrum of the TRD. The cut was placed at the minimum of the PID5 spectrum. At this minimum the hadron rejection factor is about 200 and the positron identification efficiency is approximately 91%, yielding a low contamination of both momentum parent distributions. (In the case of the hadron parent distributions the positron contamination is smaller than 2% because of the large flux ratio Φ.)

4.5 The Monte Carlo Simulation

The Monte Carlo program that was implemented is based on a program originally developed by B. Bray and K. McIlhany. The original code used parent distributions that were calculated sometimes crudely from theoretical models as well as distributions extracted from experimental data. The new program uses the parent distributions that were discussed in the previous section. These parent distributions yield Monte Carlo data that are in better agreement with experimental data (see section 4.6) because of their optimised response ranges and momentum bins, and the use of different sets of distributions for the two calorimeter thresholds in the trigger. An additional feature of the new Monte Carlo is the simulation of detector efficiencies such as the simulation of the TRD efficiency with a *TRD missing spectrum*.

Monte Carlo events are generated by the following procedure: First it is decided whether to generate a hadron or a positron. This is done randomly with respect to a parameter that sets the average flux ratio in the Monte Carlo. A momentum for each particle type is generated using the rejection method and the momentum parent distributions. The momentum bins for the PID detectors are determined from the generated momentum and the responses simulated with the transformation method.

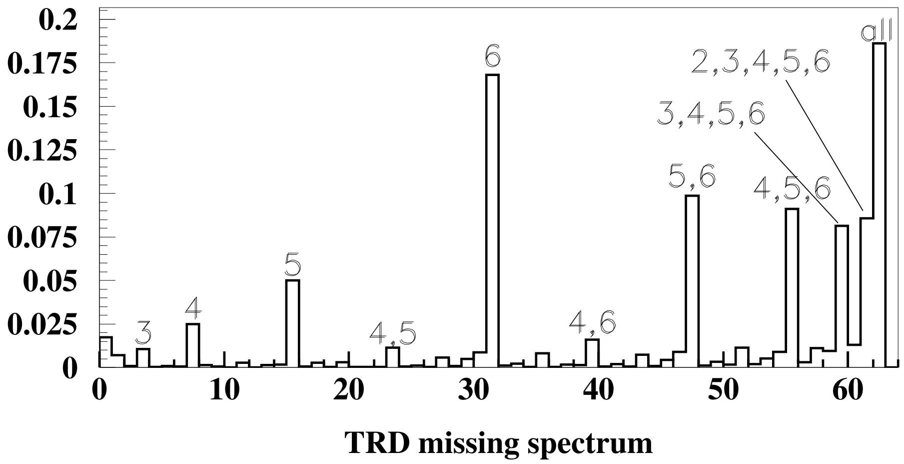

Figure 4.10: The TRD missing spectrum for the inefficiency simulation. The numbers indicate which modules have no response. See text for details.

In addition, detector efficiencies are simulated to match the no-response channels in the detector spectra. For the calorimeter and the preshower detector, this is simply done by comparing a random number with an efficiency parameter. In the case of the TRD a correlation between the efficiencies of the individual modules is considered, although the signals in the six modules are generated independently. The efficiency of the TRD is simulated with a simple Monte Carlo routine of hits and misses. The parent distribution which is used in this case was extracted from 1996 data and is shown in figure 4.10. The binary representation of the abscissa gives information on whether a module has a response or not. For example $4 = (100)_2$ means that the third module does not respond whereas $24 = (11000)_2$ means that there is no response in the fourth and fifth modules.

The spectrum illustrates that inefficiencies in the TRD are mostly due to its geometry. It is more likely that misses occur in the rear modules because the modules all have the same size. Hence the first modules have an acceptance larger than the spectrometer acceptance while the acceptance of the rear modules matches that of the spectrometer.

To simulate the inefficiency, it is randomly decided whether any combination of misses in the modules occurs at all. A random number drawn from the probability distribution shown in figure 4.10 is then generated with the transformation method and its binary representation determines which modules have no response.

The Monte Carlo therefore simulates correlated misses in the TRD modules. However, the TRD module responses and the detector responses in general are assumed to be uncorrelated in the Monte Carlo. The simulation of correlations between the PID detectors would require multi-dimensional parent distributions. There are too few data available to provide sufficient statistics to generate such parent distributions. Nevertheless, as will be presented in the next section, the agreement of the Monte Carlo generated detector responses with the experimental detector responses is very good. On the other hand, it will be shown that small correlations are crucial to a proper description of the tails of the PID distributions.

4.6 The Responses of the Particle Identification Detectors

The discussion of the Monte Carlo detector responses is restricted to a comparison with 1996 data for the high calorimeter threshold. The results for the low calorimeter threshold are of similar quality to the ones presented here.

The detector spectra calculated with the old Monte Carlo are compared to 1996 data in figure 4.11. The Monte Carlo simulates the basic features of the measured detector responses, but there are significant deviations. Obvious is the missing overflow region in the preshower response. More important is the poor agreement of the detector responses in the overlap region between hadrons and leptons.

The detector responses as simulated by the new Monte Carlo are compared to data in figure 4.12. The agreement of Monte Carlo and data is excellent which is not surprising because the Monte Carlo is based on parent distributions which were derived from data. In figure 4.13 the detector responses for hadrons and leptons are compared separately to the results of the Monte Carlo. Hadrons and leptons were discriminated in the data with cuts

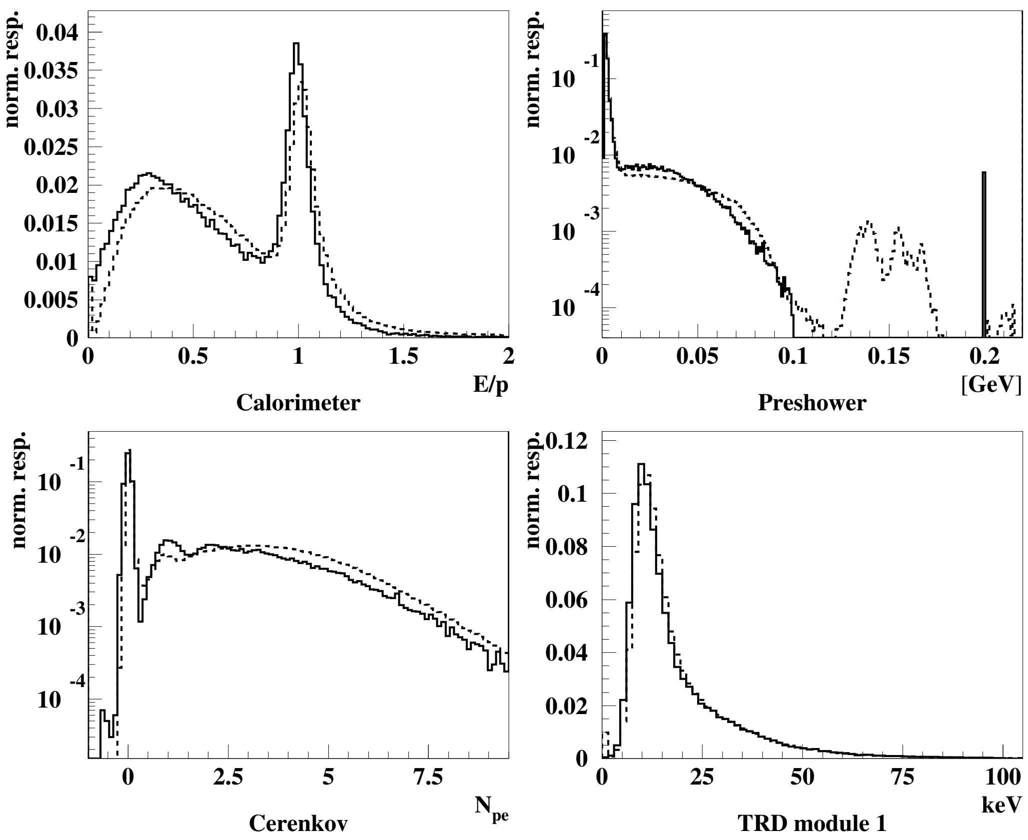

Figure 4.11: Detector responses of the old Monte Carlo compared with the data (calorimeter threshold 3.5 GeV); solid line: Monte Carlo, dashed line: data.

on PID3 in the case of the TRD and on PID5 in the case of the other three detectors. Like the overall distributions the single particle responses simulated by the Monte Carlo are in good agreement with the data.

The only crucial difference between the data and the Monte Carlo is that the Monte Carlo does not consider correlations among the detectors. The good agreement of the Monte Carlo with the data shows that the correlations are generally small.

On the other hand small deviations of the generated TRD response to the data are present, which are caused by correlations among the TRD modules. This difference is best reflected by considering the TRD truncated mean spectrum shown in figure 4.14. In the range between 15 and 45 keV the Monte Carlo is in reasonable agreement with the data,

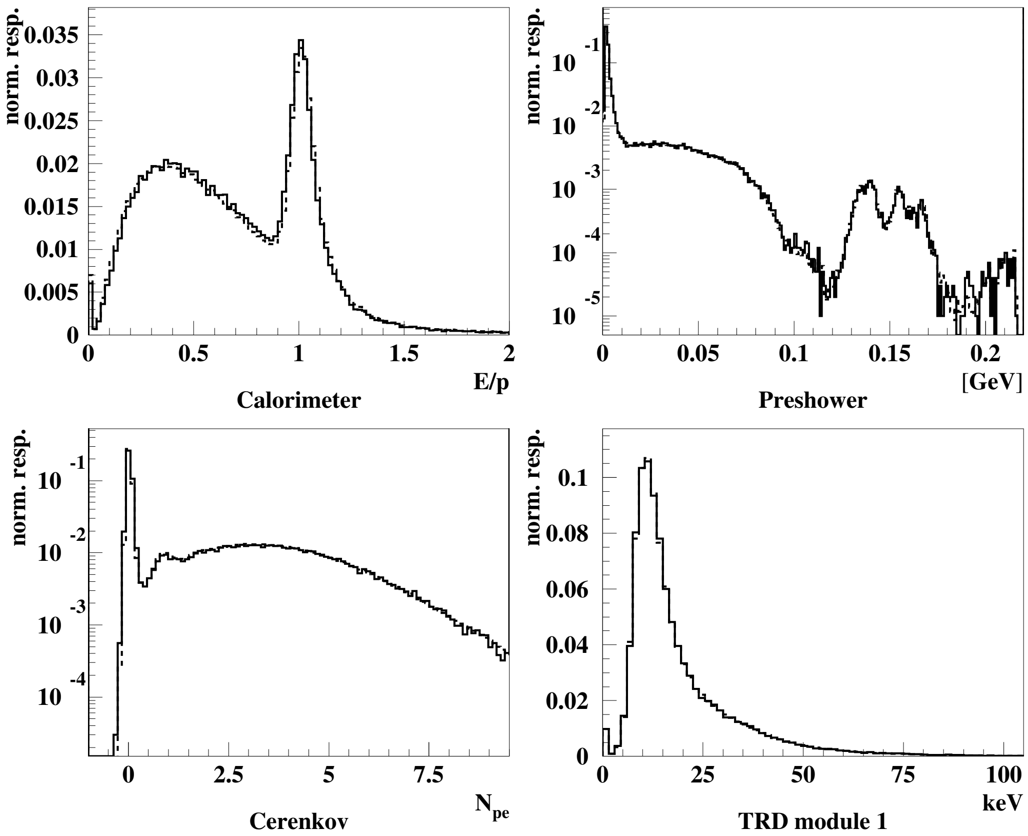

Figure 4.12: Detector responses for the high calorimeter threshold. The solid line shows the new Monte Carlo, the dashed line the data. The Monte Carlo is in excellent agreement with the data.

but the tails above 45 keV and below 15 keV are poorly reproduced. The high energy tail is likely caused by delta-rays or hadronic showers which cause large responses in all modules. The small signals below 10 keV in the data are possibly the result of correlated inefficiencies in the TRD that are not simulated by the Monte Carlo, despite the inefficiency simulation discussed above.

Overall the new Monte Carlo yields much better agreement of the generated detector spectra with the data than the old simulation. The improvement is mostly due to new parent distributions that were extracted from collected data.

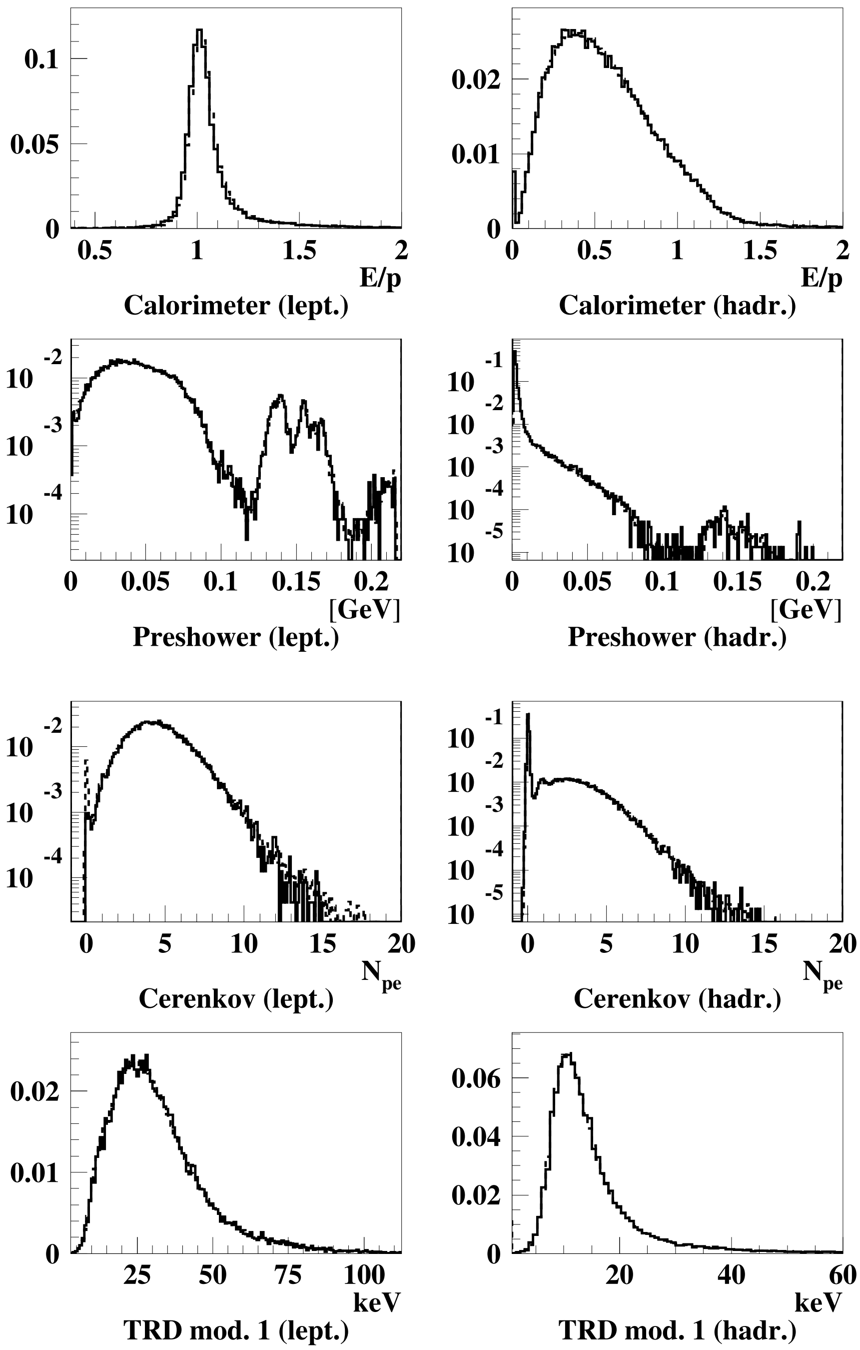

Figure 4.13: Detector responses of leptons and hadrons (Solid line: Monte Carlo, dashed line: data).

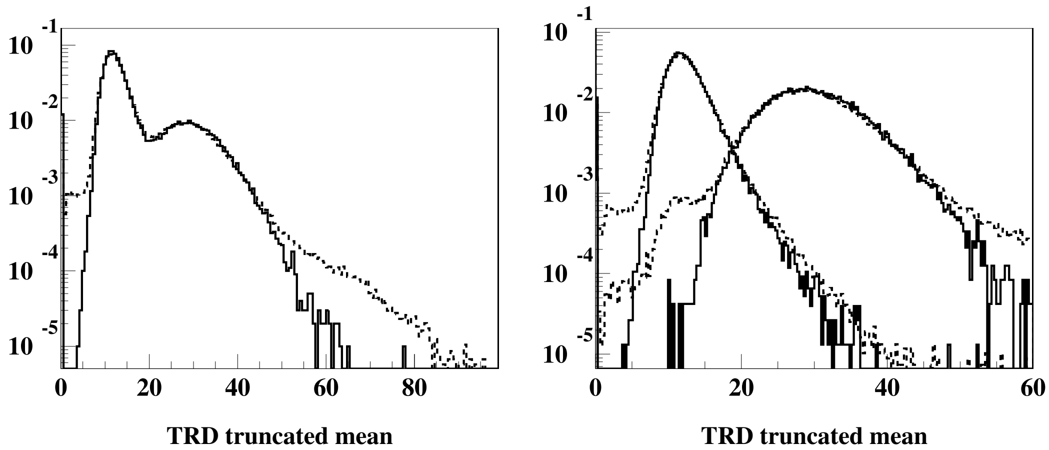

Figure 4.14: TRD truncated mean. Left plot: overall response. Right plot: hadrons (left peak) and leptons (right peak); solid line: Monte Carlo, dashed line: data. In case of the data the shoulder in the electron distributions at 10 keV is caused by a contamination of the sample and by electrons that do not deposit transition radiation in the TRD.

4.7 The PID spectra

The PID spectra for both the Monte Carlo simulation and the data are calculated with the parent distributions described in section 4.4 as the input conditional probability distributions. The results for the 1996 high calorimeter threshold data are shown in figure 4.15. The plots show two peaks, the left being the hadron peak and the right the lepton peak, except for the PID2 spectrum which has two hadron peaks. The peak closer to zero is caused mostly by particles that lose no energy in the preshower but are absorbed in the calorimeter. The preshower therefore identifies a hadron and the calorimeter a lepton. These particles are identified as hadrons by the TRD. The misidentification by the calorimeter is caused by the large energy deposition which is likely a result of charge exchange processes in the lead-glass.

In addition particles that lose some of their energy in the preshower but deposit only part of their remaining energy in the calorimeter contribute to the peak. In this case the calorimeter identifies a hadron and the preshower a lepton. However only few tracks with these properties were found.

The minimum that separates leptons and hadrons is found not to be at zero. This shift is

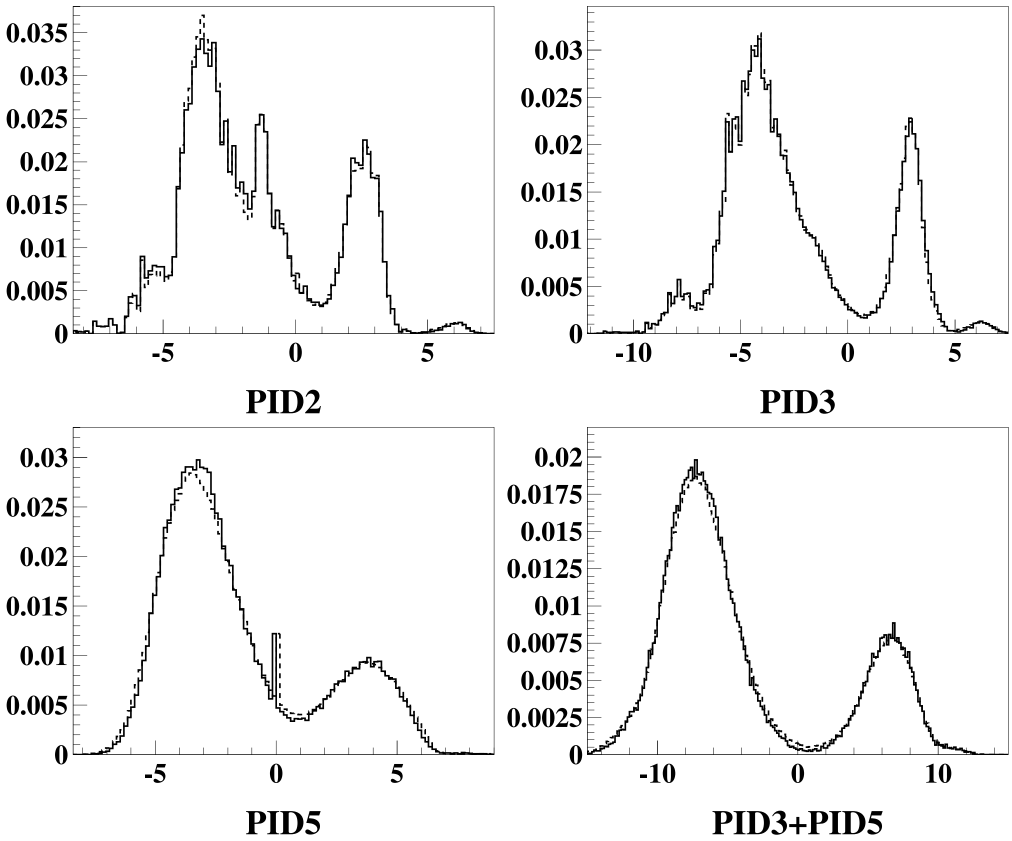

Figure 4.15: PID spectra for the high calorimeter threshold. The solid line shows the Monte Carlo, the dashed line data.

due to the fact that the flux ratio Φ was not included in the calculation of the PID quantities (section 4.2). In the case of the PID2 and PID3 distributions a shift is also caused by the hadron identification inefficiencies of the calorimeter, which shift the hadron peak closer to the lepton peak.

The Monte Carlo reproduces the $\text{PID2} = \text{PID}_{\text{Cal}} + \text{PID}_{\text{Pre}}$ and $\text{PID3} = \text{PID}_{\text{Cal}} + \text{PID}_{\text{Pre}} + \text{PID}_{\text{Cer}}$ distributions very well. The generated distributions agree with the data even in the tails (figure 4.15). The agreement for PID5 is also good, although it is not as perfect as the simulation of the PID3 spectrum. The hadron peak and the minimum where the hadron and the lepton distributions overlap are not perfectly reproduced.

More crucial are the discrepancies of Monte Carlo and data in the quantity PID3 + PID5

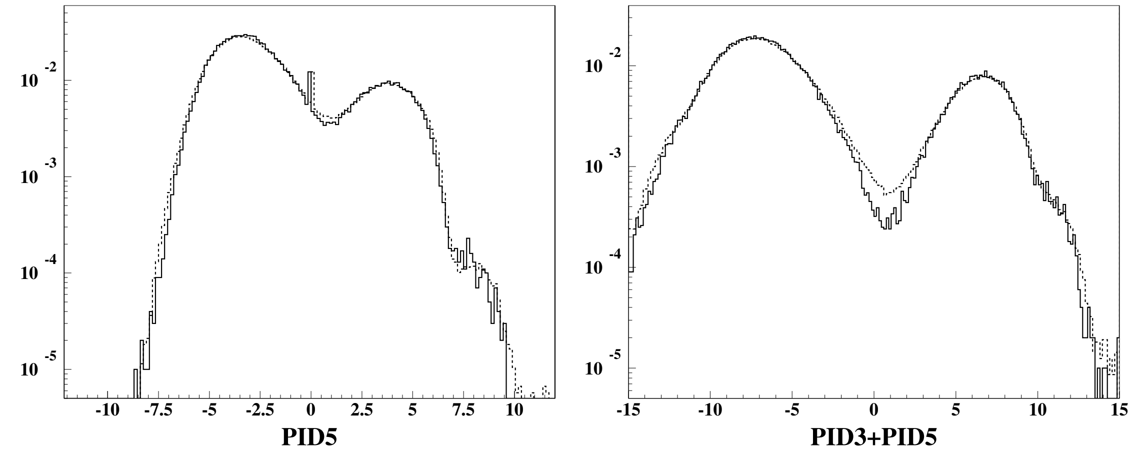

Figure 4.16: Logarithmic spectra of PID5 and PID3 + PID5. The solid line shows the Monte Carlo, the dashed line the data (1996 data, high calorimeter threshold).

which yields the highest hadron rejection factors because all PID detectors are included in the probability analysis. The overall agreement is reasonable, but the agreement around the minimum is worse than the agreement of the two quantities PID3 and PID5 indiviually. Figure 4.16 illustrates the disagreement for PID5 and PID3 + PID5. The minimum in the PID5 spectrum is reasonably reproduced but the Monte Carlo clearly overestimates the discrimination power of PID3 + PID5. The reason for this difference between Monte Carlo and data is not due to problems in the simulation of the single PID detectors but rather correlations in the data that are not simulated by the Monte Carlo.

The cause for the differences of the Monte Carlo and the data is best discussed using the two-dimensional scatter-plots of PID3 and PID5 shown in figure 4.17. It is worthwhile to divide the plots into four regions. Region A contains particles which are identified as hadrons by the TRD and as leptons by the combination of the other three PID detectors. In region B all detectors identify a lepton and in region C they all detect a hadron. In region D the TRD identifies a lepton while the other three detectors together see a hadron. The borders of the regions were chosen according to the position of the minima in the one-dimensional plots of PID3 and PID5. Clearly, regions A and D are the two regions that cause problems in the sum of PID3 and PID5. The Monte Carlo generated only few events in the areas A and D, while there are relatively many particles in these areas for the data.

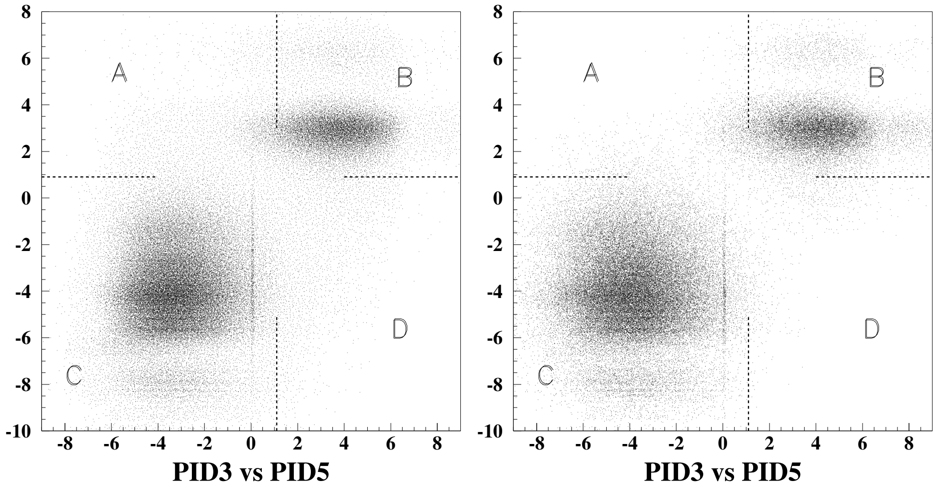

Figure 4.17: PID3 vs PID5; the left plot is experimental data and the right plot Monte Carlo data (1996 data, high calorimeter threshold).

In both regions there are two possibilities for the particle type, because either the TRD or the combination of the other three detectors misidentify the particle type. A hadron with PID values in region A is misidentified as a lepton by the sum of the calorimeter, the preshower, and the Čerenkov detector. In this case at least two out of the three detectors have to misidentify the particle or one of the detectors has to misidentify while the others give only low probabilities for finding a hadron. Both possibilities are unlikely. In the other case the TRD is at fault. If the TRD misidentifies the lepton as a hadron, the lepton did not cause as large a signal in the TRD as expected. The small signal could be caused by leptons with tracks that miss one or more modules due to geometric effects. This possibility was investigated and ruled out by imposing fiducial cuts on the TRD modules and thereby only considering tracks that lie well in the TRD acceptance. The percentage of particles in region A remained the same.

Another cause for zero signals in a track is misalignment of the TRD. The HERMES reconstruction program assigns certain cells to a given track according to a mapping of the spectrometer. However, if the TRD detector is slightly misaligned, it is possible that the signals in some of the modules occurred in a cell other than the ones assigned to the track. This gives rise to a zero signal in those modules.

In the other problematic region, region D, the number of particles also did not change with fiducial cuts ruling out the limited acceptance of the spectrometer as a cause for the particle misidentification. If the particle is really a lepton, there is a PID3 inefficiency which is unlikely because there are three detectors contributing to this quantity. The more probable possibility, that it is actually a hadron, is caused by a misidentification in the TRD due to hadrons with a large energy deposition in the TRD. One possible cause of the misidentification is a hadronic shower that results in a large signal in the TRD. This makes a hadron look like a lepton. These showers could be initiated in the radiators or in the lead located in front of the TRD to shield it from synchrotron photons.

This effect is also the source of the disagreement of the Monte Carlo and the data in the PID5 spectrum (figure 4.15). The simulated hadron peak is larger because the Monte Carlo does not simulate the hadronic showers, that lead to the hadron misidentification in the data. Moreover this results in the disagreement in the overlap region.

Generally, the observed discrepancy is very subtle and affects only very few events. Nevertheless, they are important in the contamination/efficiency analysis because of the high discrimination power of the particle identification system (cf. section 4.9).

Finally the new PID distributions were compared to the PID spectra calculated with the old parent distributions. Two-dimensional scatter-plots of old versus new PID3 and PID5 are shown in figure 4.18. In the case of the TRD the new and the old methods are in good agreement because they are essentially the same. The two PID schemes disagree for less than 1% of the tracks (regions A and D separated by the solid line in figure 4.18). Most of the particles are located in a narrow band around the diagonal. In the case of PID3 about 2% of the particles that are identified as hadrons in the old scheme are found to be leptons in the new scheme while 1% of the sample are identified as leptons with the old and as hadrons with the new analysis. The scatter-plot also illustrates that each scheme gives a somewhat different PID value.

If more restrictive cuts are applied to the PID spectra, a smaller inconsistency of the old and the new method is found. The dashed lines in figure 4.18 are an example for such harder cuts. (Similar cuts are applied to $\mathrm{PID3} + \mathrm{PID5}$ in data analysis.) The particles in between the areas A,B,C, and D are discarded. In this case the number of particles that are identified differently by PID3 and PID5 (regions A and D) drops below 0.02% for PID5 and below 0.1% for PID3.

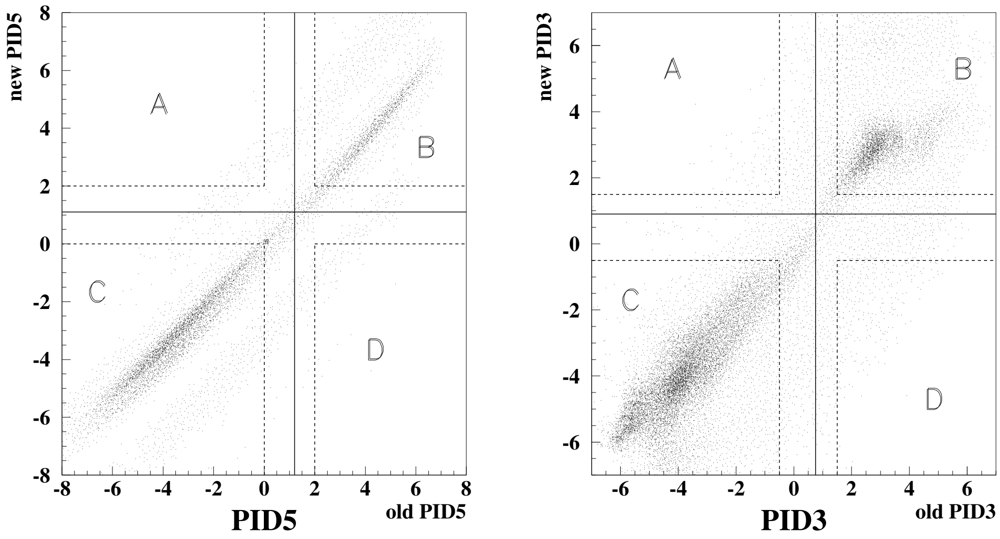

Figure 4.18: Comparison of old and new PID methods; the solid lines indicate cuts based on the minima in the PID spectra and the dashed lines harder cuts for a cleaner identification of positrons and hadrons.

The old and new PID analysis schemes are therefore generally in good agreement. In this sense the improved parent distributions verify that the PID analysis with the old distributions yielded reasonable results. The new scheme is nevertheless superior in principle because of the better agreement of the new Monte Carlo with the data.

4.8 The Hadron and Lepton PID Distributions

The contributions by hadrons and positrons in the PID spectra have to be discriminated in order to determine the performance of the PID system. In the past, estimates were often done by fitting exponential or Gaussian functions to the PID spectra [35]. In the Monte Carlo, the particle type is known by a flag associated with each particle. Another method was recently suggested by Yvo Gärber [36]; it will be referred to as the *probability method*. This method uses the definition of the logarithmic ratio PID. It follows from equation (4.6) that the probabilities for a lepton $\mathcal{P}_D^e$ or a hadron $\mathcal{P}_D^h$ are given by

$$\mathcal{P}_D^e = \frac{10^{\mathrm{PID}}}{1+10^{\mathrm{PID}}} \qquad \text{and} \qquad \mathcal{P}_D^h = \frac{1}{1+10^{\mathrm{PID}}}. \tag{4.16}$$

If N particles are found at a given PID value, the number of leptons N_e and hadrons N_h in that channel is therefore

$$N_e = N\frac{10^{PID}}{1+10^{PID}} \qquad \text{and} \qquad N_h = N\frac{1}{1+10^{PID}}. \tag{4.17}$$

The PID value has to be shifted by a certain amount if the flux factor Φ is neglected in the calculation of the PID spectra. A momentum independent shift was chosen, so that a good agreement of the single particle distributions with the Monte Carlo was achieved.

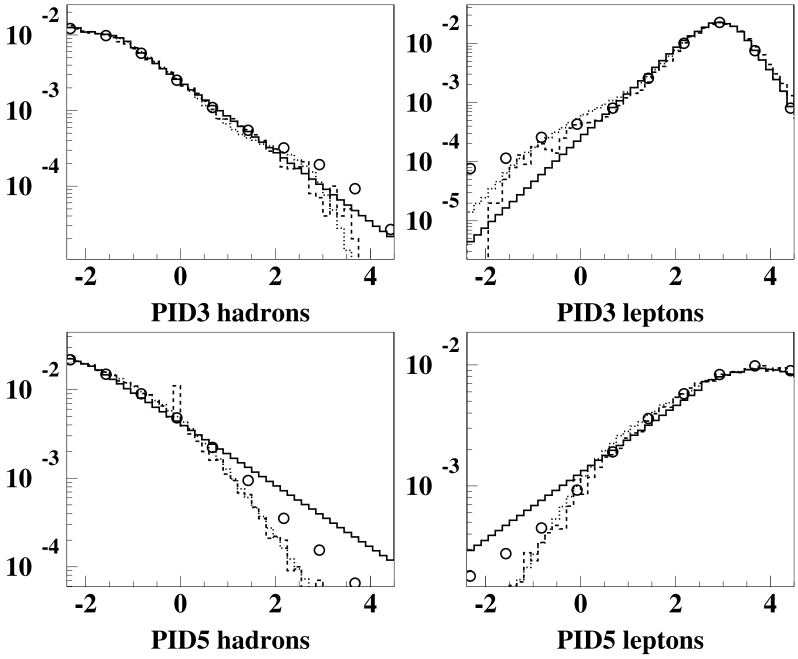

Figure 4.19: Fits of the PID spectra. Solid line: exponential fit of the data; dashed line: Monte Carlo; dotted line: probability method; circles: PID cuts on the data (see text for details). 1996 data, high calorimeter threshold.

The exponential estimates and the probability method are compared to the Monte Carlo in figure 4.19, which focuses on the region around the minimum in the spectra of PID3 and PID5 where the contributions by hadrons and leptons overlap. The circles indicate the distributions extracted from data with cuts on PID5 for the PID3 distributions and on PID3 for PID5.

In the case of PID3 the estimates by the three methods for the contributions by hadrons and leptons are in reasonable agreement. The distribution that was extracted with cuts on PID5 also agrees with the three methods in principle. A deviation towards larger values is seen in the tails, which is likely the result of a contamination of the particle samples that were extracted with the cuts.

In the PID5 spectrum the Monte Carlo and the probability method are in very good agreement. The two methods predict a smaller overlap than the exponential fit and the distributions that were extracted with a cut on PID3. The estimate by the Monte Carlo and the probability method as well as the distributions given by cuts on PID3 indicate that the exponential fit overestimates the contamination of the single particle samples.

4.9 Contamination/Efficiency Analysis

The efficiency with which positrons are identified in a data sample is an important characteristic of any PID system. The extraction of a clean positron sample from the data set is crucial at HERMES for the identification of inclusive deep inelastic scattering events. For semi-inclusive analysis the tagging of the hadron type is also important, but the probability based particle identification procedure described in this chapter only discriminates between leptons and hadrons. Pions can be distinguished from other hadrons with a simple cut on the Čerenkov counter. In the data taken in 1998 and 1999 the ring imaging Čerenkov counter (RICH) will allow for an identification of kaons and protons in addition to pions.

Three variables are generally used to describe the performance of the particle identification scheme: the hadron rejection factor (HRF), the positron efficiency (see section 4.1), and the *contamination of the positron sample* defined as the percentage of hadrons in the positron sample.

The PID distributions for hadrons and positrons calculated by the three methods discussed in the previous section were used to analyse the performance of the PID system. In figure 4.20 the contamination of the positron sample versus the positron identification efficiency is plotted. Figure 4.21 shows the hadron rejection factor as a function of the positron efficiency. The hadron rejection factor for the TRD truncated mean response is also shown

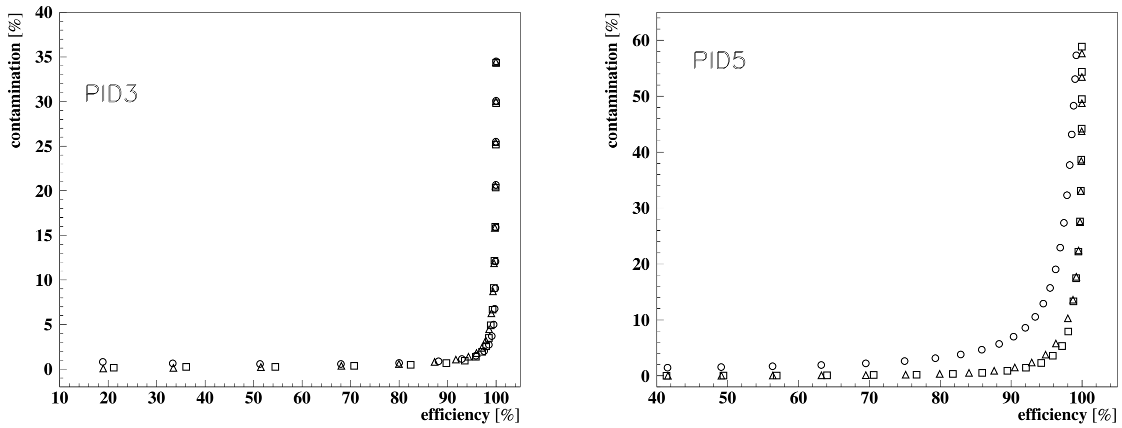

Figure 4.20: The hadron contamination as a function of the positron efficiency. The squares show the efficiency and the contamination calculated from the Monte Carlo; the circles are calculated from exponential fits of the data and the triangles are calculated from the probability method. 1996 data, high calorimeter threshold.

for comparison.

The exponential fit, the Monte Carlo and the probability method applied to the PID3 distribution result in good agreement of the contamination/efficiency spectra. The hadron rejection factors calculated from the Monte Carlo and the exponential estimate agree for efficiencies greater than 97%, but deviate for lower efficiencies. The probability method yields generally lower hadron rejection factors.

It is in principle difficult to decide which of the three methods gives the best estimate of the performance of the PID system. The PID3 distributions that were extracted with cuts on PID5 estimate a larger overlap than any of the three methods (figure 4.19). The Monte Carlo, which estimates the largest HRF likely overestimates the PID3 hadron rejection factor because it does not take all the effects in the detectors into account. However, the very good agreement of the Monte Carlo detector responses with the data suggests that the true hadron rejection factor is close to that predicted by the Monte Carlo.

In the case of the PID5 spectrum the contamination estimated with the exponential fit is significantly larger than those given by the Monte Carlo and the probability method. Consequently the hadron rejection factor estimated from the fit is much smaller. It is even lower than that of the truncated mean. The distributions that were extracted with cuts on

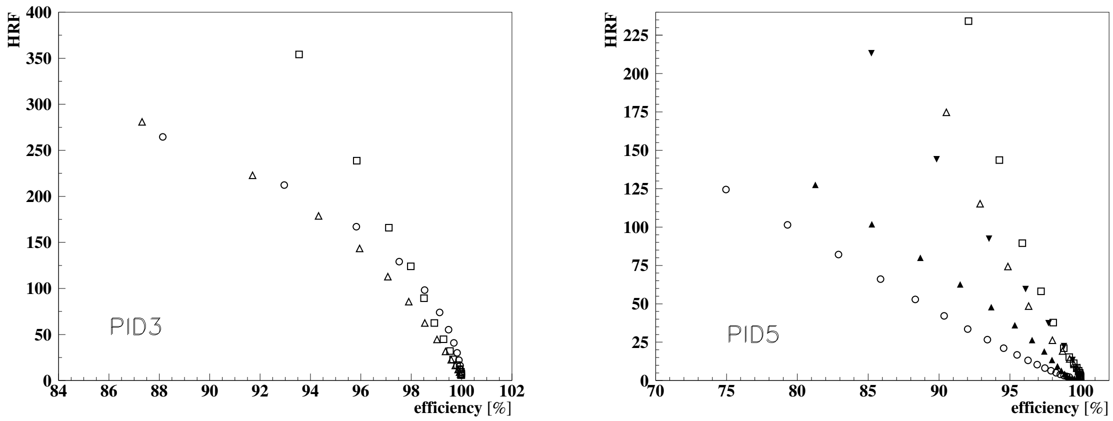

Figure 4.21: The hadron rejection factor as a function of the positron efficiency. The squares show the efficiency and the HRF calculated from the Monte Carlo; the circles are calculated from exponential fits of the data and the triangles are calculated from the probability method. The filled triangles show the hadron rejection factor for the TRD truncated mean given by the Monte Carlo (▼) and by an exponential fit (▲). 1996 data, high calorimeter threshold.

PID3 verify that the exponential fit underestimates the performance of the TRD for particle identification (figure 4.19).

The reasonable agreement of the Monte Carlo responses with the TRD responses extracted from data and the agreement with the probability method suggest that these two methods approximate the true hadron rejection factor. The larger estimate of the HRF by the Monte Carlo simulation is a result of the missing correlations between the TRD modules. This deficiency leads to the conclusion that the probability method gives the best estimate of the HRF.

Naturally, the combination of all PID detectors in the quantity PID3 + PID5 results in better discrimination of the two particle types. The HRF as a function of the positron efficiency is shown in figure 4.22. The Monte Carlo gives hadron rejection factors that are much larger than the HRF's estimated by the exponential fit and the probability method. This is clearly an overestimate of the true hadron rejection factors because of the differences of the simulated PID3 + PID5 distribution and the data especially in the overlap region (cf. section 4.7).

On the other hand the true hadron rejection factor is likely larger than the prediction

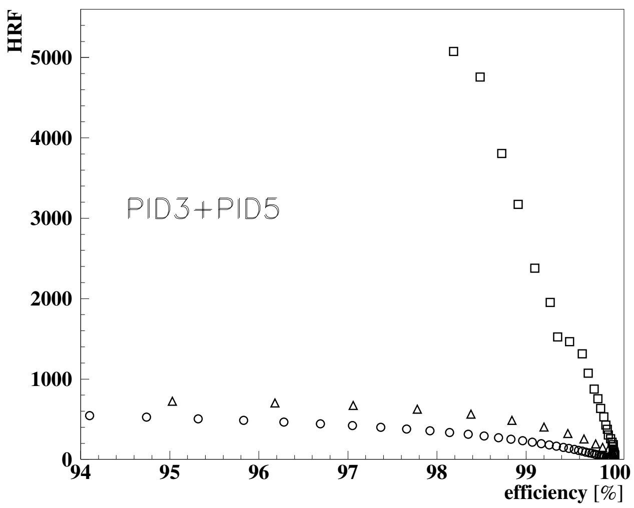

Figure 4.22: The hadron rejection factor as a function of the positron efficiency. The squares show the efficiency and the HRF calculated from the Monte Carlo; the circles are calculated from exponential fits of the data and the triangles from the probability method. 1996 data, high calorimeter threshold.

by the exponential fits because the fits were found to underestimate the factors for the individual distributions PID3 and PID5.

The true factors are probably close to or slightly larger than the HRF's estimated by the probability method, which are only a bit larger than the ones given by the exponential fit. The fact that the probability method is independent of a simulation and its flaws, such as the missing correlations in the Monte Carlo simulation, supports this conclusion. At a positron identification efficiency of 98% an estimate for the hadron rejection factor is six hundred. On the trigger level a hadron rejection factor of at least ten is achieved (section 3.4). Therefore the overall hadron rejection factor of the HERMES PID system is larger than 6,000. Further improvement would be found if the flux factors were taken into account [32].

4.10 Summary

In this chapter a new particle identification scheme for the HERMES experiment has been presented. The parent distributions that are used for the probability based identification of positrons and hadrons were extracted from data taken in 1996.

A Monte Carlo simulation was implemented using the parent distributions to simulate the four PID detectors. The simulation was used to optimise the bins for the parent distributions and to estimate the performance of the particle identification system. The parent distributions yield a much better agreement between the detector responses generated by the Monte Carlo and the experimental detector responses than an older Monte Carlo that was based on sometimes crude theoretical as well as experimental parent distributions.

The generated TRD response agrees reasonably well with the data, but small deviations exist due to correlations between the individual detector modules that the Monte Carlo does not account for. The simulated calorimeter, preshower, and Čerenkov responses are in excellent agreement with the data.

The experimental and simulated PID distributions that are used to discriminate between positrons and hadrons agree in the case of the calorimeter, the preshower, and the Čerenkov detector. The simulated and the generated PID distributions for the TRD, known as PID5, have some small discrepancies due to correlations between the TRD modules, but reasonable agreement was achieved. The quantity PID3, which is the combination of the PID values of the calorimeter, the preshower detector, and the Čerenkov counter, is in very good agreement with the data.

A discrepancy between data and Monte Carlo was found in the $\mathrm{PID3} + \mathrm{PID5}$ spectrum. The distributions disagree in the important area where the positron and the hadron distributions overlap. The Monte Carlo overestimates the discrimination power of the sum of the four detectors, while a third method to discriminate the positron and hadron distributions estimates hadron rejection factors on the order of the HRF's calculated from exponential fits. An estimate of the hadron rejection factor at a positron identification efficiency of 98% is six thousand, if all particle identification detectors are fully operational and the HRF of the trigger is included. However, flux factors have not been taken into account in these studies.

The generated parent distributions were used for particle identification in the HERMES analysis to extract the inclusive and semi-inclusive asymmetries from data taken in 1997. For the 1995 and 1996 data the older parent distributions were used but the systematic errors introduced are small because of the agreement of the old and the new PID distributions.

Chapter 5

The Asymmetries on Hydrogen

5.1 Event and Track Selection

Inclusive and semi-inclusive asymmetries as described in section 2.4 were extracted from data taken in 1996 and 1997 with a polarised hydrogen target. The extraction was carried out using a number of conditions on the event parameters (cuts). The cuts can be divided in two groups: cuts on the burst-level that are applied to all tracks in one burst (cf. section 3.5) and cuts that are applied to the individual tracks. On the burst-level, slow control parameters are checked to reject data with poor running conditions. Cuts on the individual tracks are applied to select particles that are within the acceptance of the spectrometer and that originate from DIS events.

5.1.1 Burst Selection

The data quality cuts on the burst-level were taken from results of the HERMES inclusive analysis group. This section only summarises the relevant cuts. Additional cuts rejected data that were taken when for example the spectrometer or parts of it were not operational or when the conditions of the beam or the target were unstable.

Data Acquisition

The first and the last burst in a run were rejected. In the first burst it is possible that the system was not completely initialized, whereas in the last burst the recorded data might be incomplete.

All bursts with a burst length larger than 11 seconds are discarded. Usually a burst is 10 seconds long and all bursts with a different length should be rejected. However in 1996 and 1997 a burst was split into three records when the spin of the target polarisation was flipped during the burst and only the record in which the spin was changed is discarded.

The live time, which is the percentage of the generated triggers recorded by the data acquisition system, was required to be larger than 80%, but was typically larger than 96%.

Luminosity

A stable measurement of the luminosity is crucial for the calculation of the asymmetries, because it directly enters the equation of the measured asymmetry $A_{||}$ (see below: equation (5.1)). The luminosity rate was required to have values between 5 and 60 Hz to ensure that the measured luminosity was reasonable and to discard spikes in the luminosity that usually indicate partial beam losses.

Beam and Target Polarisation

The polarisations of the target and the beam were required to be reasonably large. Low polarisations do not contribute significantly to the asymmetry measurement. Furthermore a large target polarisation ensures that the target was stable and not in transition. The target polarisation was flipped every one to two minutes in order to minimise systematic errors in the asymmetries.

In the case of the beam polarisation a fitted value was used to remove unphysical jumps and statistical fluctuations in the polarisation measurement. Because the measurement is only carried out on a minute by minute basis, it was also required that the time elapsed since the last valid measurement of the beam polarisation was not longer than 5 minutes. The cuts applied to the polarisations are[1]:

- $30\% < P_{Beam} < 80\%$,
- $80\% < P_{Target} < 99\%$.

[1] P_{Target} is the polarisation measured by the Breit Rabi Polarimeter.

5.1.2 Track Selection

Geometrical and Fiducial Cuts

Geometrical cuts on the tracks are applied to account for the limited acceptance of the spectrometer. In particular two cuts were used on the projections of the polar angle onto the $y-z$ plane (θ_x) and onto the $x-z$ plane (θ_y):

- $0.040\,\text{mrad} < |\theta_y| < 0.140\,\text{mrad}$,
- $|\theta_x| < 0.180\,\text{mrad}$.

Tracks that did not have angles within these ranges were discarded. The accepted tracks are shown in figure 5.1. The cuts reflect the fact that the spectrometer has two separate halves, one above the beam-line and the other below it.

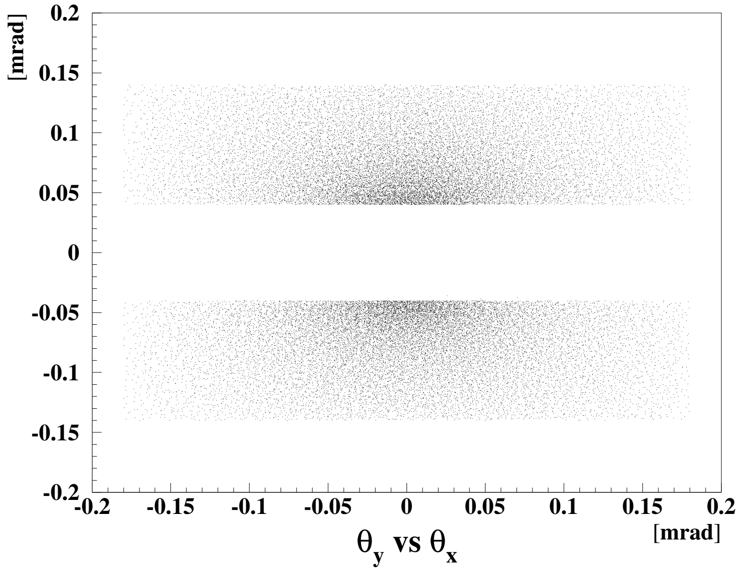

Figure 5.1: The geometrical acceptance of the HERMES spectrometer.

In order to select only tracks originating from beam-target interactions within the target cell two volume cuts were imposed on the point of interaction (the vertex) in the target:

- $-18\,\text{cm} < z_{\text{vertex}} < 18\,\text{cm}$,

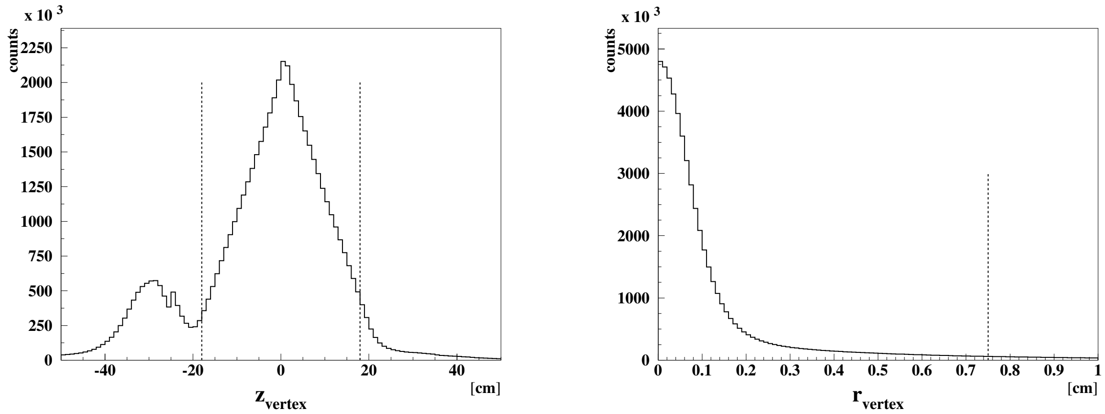

Figure 5.2: Cuts on the vertex position in the target cell.

- $r_{\text{vertex}} < 0.75\,\text{cm}$,

where z_{vertex} is the distance of the vertex from the middle of the target cell along the beam direction and r_{vertex} the distance of the vertex from the middle of the target cell perpendicular to the z-direction. The cuts are shown in figure 5.2. The graph of z_{vertex} exhibits two peaks, one centered at 0 cm and a smaller peak at about -30 cm. The large peak is caused by the high target gas density in the middle of the cell where the gas is injected. The smaller peak results from vertices located in the collimator. These events are discarded by the fiducial cut on z_{vertex}.

Kinematic Cuts

Kinematic cuts were used to identify events in the DIS region. A cut on the transferred momentum Q^2 was applied to select only events in the scaling region, where the parton model can be used to describe the scattering process:

- $Q^2 > 0.8\,\text{GeV}^2$,

The resonance region of the scattering reaction is rejected by requiring that the total energy W^2 be larger than 3.84 GeV^2:

- $W^2 > 3.84\,\text{GeV}^2$.

The parameter y is restricted to avoid the elastic scattering region and regions where the radiative corrections applied to the data are very large:

- $0.1 < y < 0.85$.

The impact of these restrictions on the variables Q^2 and ν is shown in figure 5.3. Also indicated are a few values of x_{bj}.

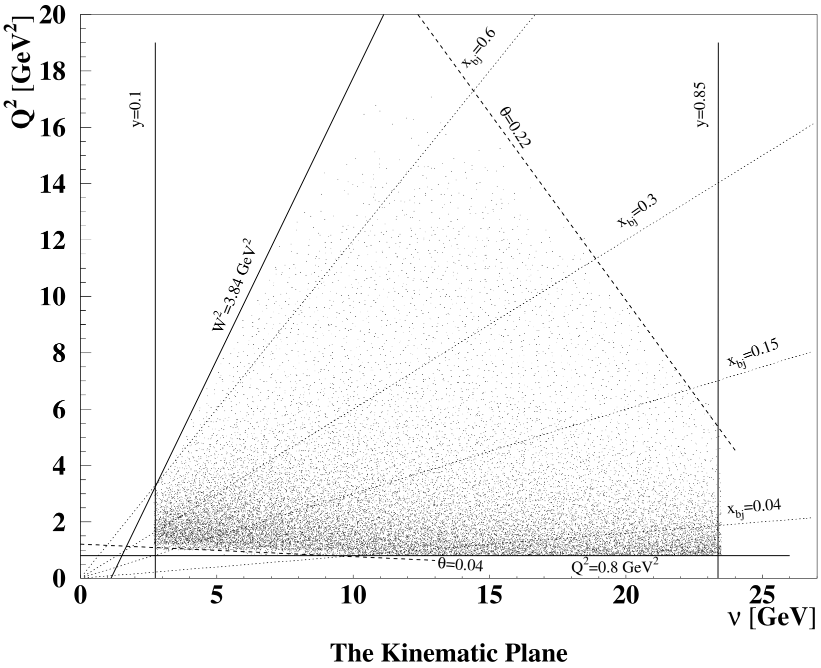

Figure 5.3: The kinematic plane. The solid lines show the kinematic cuts that were applied; the dashed lines indicate the limit of the spectrometer acceptance and the dotted lines show some values of x_{bj}.

Positron Identification

The PID value PID3 + PID5 was required to be larger than 2 for a positron. However, only PID3 was used if the signal in the TRD was discarded in the data quality analysis or not available. In case of a problem in the Čerenkov detector only the distribution PID2 + PID5 was used to identify positrons. This procedure is referred to as downshifting and was applied to less than 1% of the data. The preshower detector and the calorimeter are operational for all recorded events because the response of the two detectors is included in the trigger.

Furthermore a signal in the calorimeter larger than 3.5 GeV was required to select positrons with an energy in the deep inelastic scattering region and discard lower energetic background events.

Hadron Identification

Hadrons were identified with a cut on the PID3 + PID5 value at -1. The downshifting procedure that was used for the electron identification was also used to identify hadrons, if either the Čerenkov counter or the TRD was not available.

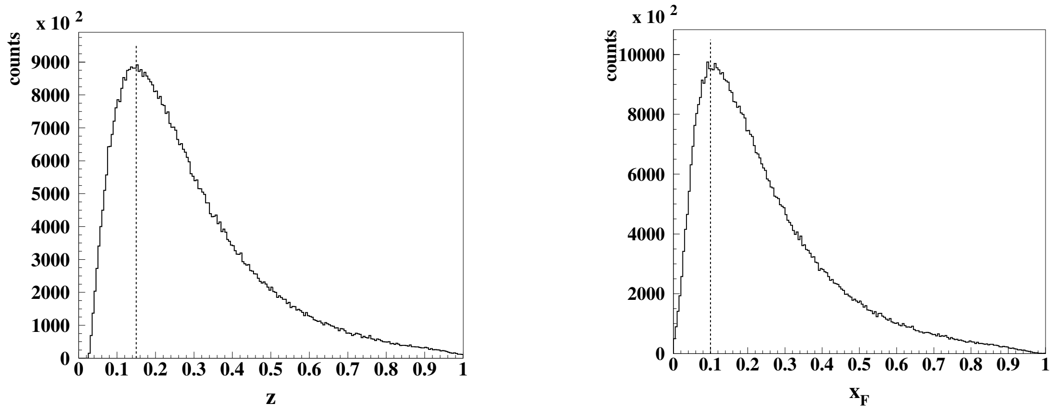

Figure 5.4: Cuts on z and x-Feynman to identify the leading hadron

In addition it is necessary to discriminate current fragments from target fragments. As described in section 2.1, current fragments can be identified with cuts on the variables x_F and z. The distributions of these two parameters are shown in figure 5.4. Current fragments were identified by the cuts:

- $x_F > 0.1$,
- $z > 0.15$,
- $W^2 > 10\,\mathrm{GeV}^2$.

The cut on W^2, which is more restrictive than for the inclusive asymmetries helps to separate the current and target regions.

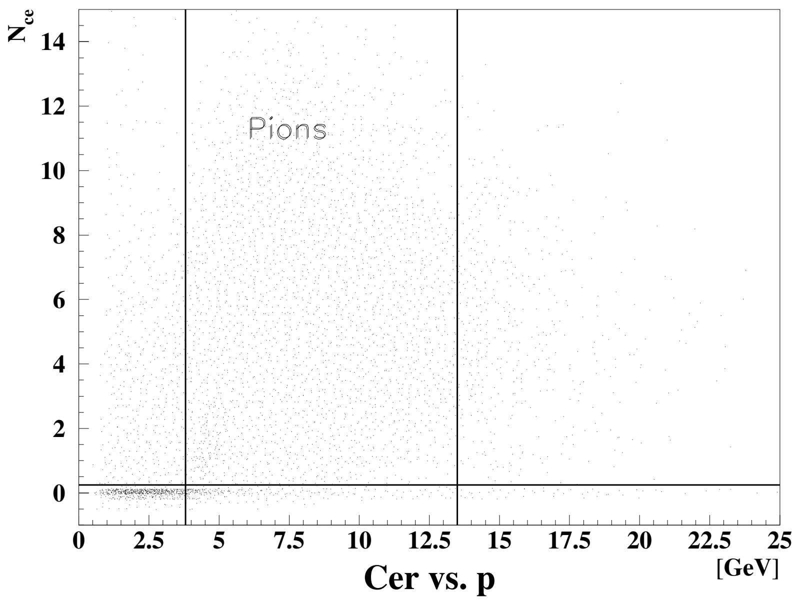

Figure 5.5: The cuts applied to the Čerenkov response to identify pions in the hadron sample

Pions have to be distinguished from other hadrons for the extraction of the valence quark spin distributions. The Čerenkov counter was used for this task because unlike other hadrons, pions that have a momentum above 3.8 GeV emit Čerenkov radiation. The next heavier hadron, the kaon, has a momentum threshold of 13.6 GeV. Therefore hadrons with momentum between 4.0 GeV and 13.5 GeV and a mean number of photons in the Čerenkov counter greater than 0.25 were identified as pions. Figure 5.5 illustrates the cuts in the Čerenkov response-momentum plane.

5.2 Background Correction

The DIS data sample was corrected for events that are identified as DIS events, but originate from different processes. The main source for these pseudo-DIS events is charge symmetric background. A positron emerging from pair production is misidentified as a DIS positron, if

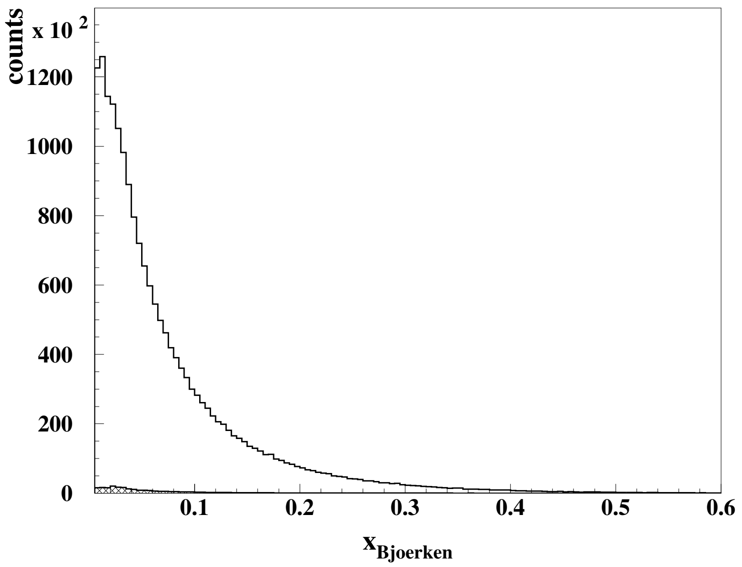

Figure 5.6: The charge symmetric background as a function of x_{bj}. The shaded histogram shows the distribution of the background electrons. The contribution of charge symmetric processes is tiny.

it passes the DIS positron cuts discussed in the previous section. The photons that cause the pair production are for example produced in the decay of π^0's into two photons. It is also possible that a hadron that emerges from photo-production is misidentified as a DIS positron. In this case a second hadron is misidentified as a semi-inclusive hadron and contributes to the semi-inclusive asymmetries.

The inclusive and the semi-inclusive data were corrected for these types of background. If an electron was, except for its charge, identified as a DIS positron, a positron with the same kinematic properties was subtracted from the DIS positron sample. A hadron that was detected in coincidence with the electron was also subtracted from the hadron count rate.

This procedure relies on the assumption that the background is charge symmetric. It is assumed that the probabilities to detect the electron or the positron of the background process are equal. Therefore for every background electron there is a positron originating from a background event in the data.

Figure 5.6 shows the number of background events in comparison to the identified deep inelastic scattering events that were extracted from 1997 data. This correction is very small.

5.3 Extraction of the Asymmetries

Calculation of the Asymmetries

The inclusive and semi-inclusive asymmetries $A_{\|}$ and $A_{\|}^h$ (eq. (2.28)) were calculated from the measured particle yields in the two target spin-states, the measured luminosity and the target and beam polarisations:

$$A_{\|}^h = \frac{N_{\uparrow\downarrow}^h L_{\uparrow\uparrow} - N_{\uparrow\uparrow}^h L_{\uparrow\downarrow}}{N_{\uparrow\downarrow}^h P_{\uparrow\uparrow} + N_{\uparrow\uparrow}^h P_{\uparrow\downarrow}}, \tag{5.1}$$

where $L_{\uparrow\downarrow}$ is the integrated luminosity when the spin of the target and the beam are anti-aligned,

$$L_{\uparrow\downarrow} = \int_{\uparrow\downarrow} \mathcal{L}(t)\,\mathrm{d}t \tag{5.2}$$

and the luminosity weighted polarisation $P_{\uparrow\downarrow}$ is given by

$$P_{\uparrow\downarrow} = \int_{\uparrow\downarrow} \mathcal{L}(t)\,P_{beam}(t)\,P_{target}(t)\,\mathrm{d}t. \tag{5.3}$$

The luminosity $L_{\uparrow\uparrow}$ and the polarisation $P_{\uparrow\uparrow}$ are defined analogously for aligned beam and target polarisations. $N_{\uparrow\downarrow}^h$ ($N_{\uparrow\uparrow}^h$) is the number of hadrons observed when the target spin and the beam spin are anti-aligned (aligned). The asymmetry in equation (5.1) is therefore corrected for the beam and the target polarisations. The fraction f of polarisable nucleons in the target is assumed to be 1. The asymmetries $A_{\|}^h$ were then corrected by the depolarisation factor D given in equation (2.30) to find the asymmetries A_1^h:

$$A_1^h = \frac{A_{\|}^h}{D}. \tag{5.4}$$

In order to determine the depolarisation factor the parameter y was calculated from the kinematics of the positron and the ratio R from the parameterisation given in [16].

In the case of the inclusive measurement, the number of DIS positrons in each target spin state was counted to calculate the asymmetry. The semi-inclusive asymmetries were extracted for positive hadrons, negative hadrons, and positive and negative pions. Furthermore the charge difference asymmetries were calculated from the count-rates $N_{\uparrow\downarrow}^{h^+-h^-} \equiv N_{\uparrow\downarrow}^{h^+} - N_{\uparrow\downarrow}^{h^-}$ and $N_{\uparrow\downarrow}^{\pi^+-\pi^-} \equiv N_{\uparrow\downarrow}^{\pi^+} - N_{\uparrow\downarrow}^{\pi^-}$. The pion charge difference asymmetry was used to extract the spin distribution functions of the valence quarks in the proton (cf. sections 2.4 and 2.5).

Asymmetry Results

Figures 5.7 to 5.9 show the asymmetries that were extracted from HERMES data taken in 1996 and 1997. The data were collected with a hydrogen target and the asymmetries are therefore for the proton. The errors shown are the statistical errors that arise in the asymmetry calculation.

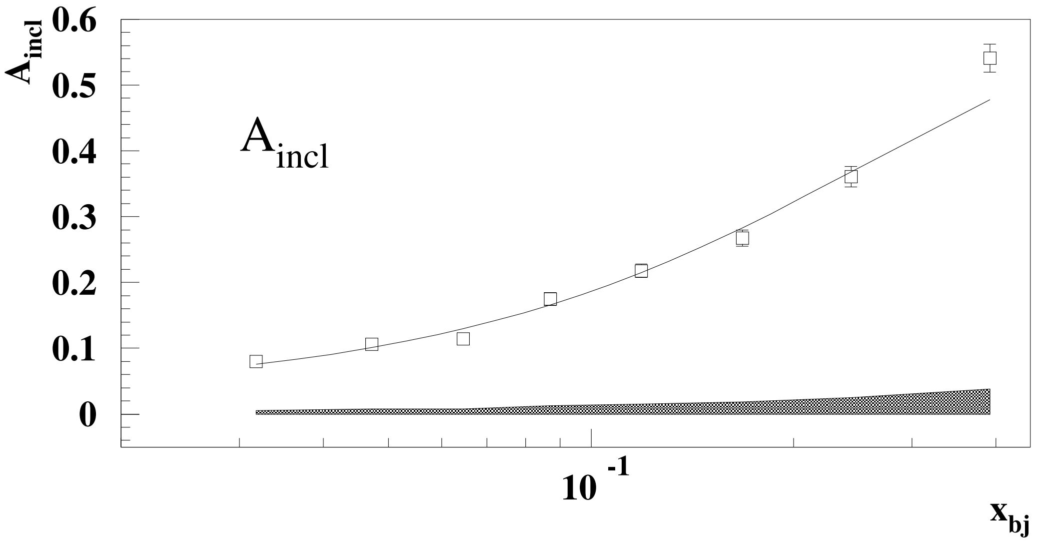

Figure 5.7: The measured inclusive asymmetry (1996 and 1997). The solid line indicates a parameterisation given by the GRSV model [37]. The error bars are statistical only and the band illustrates the estimated systematic uncertainty.

The data were analysed with the cuts listed in the previous section. In the case of the 1996 data the old PID scheme was used whereas for the 1997 data the new PID scheme was utilised to identify hadrons and leptons. The x_{bj}-range was divided into eight bins as shown in table 5.1. The bins are a compromise between the resolution in x_{bj} and the available statistics for the semi-inclusive data.

The inclusive and semi-inclusive asymmetries have the same basic features. The asymmetry is small for small x_{bj} where the quark sea dominates, indicating that the spin contributions are diluted by the unpolarised part of the quark sea. At $x_{bj} = 1/3$ the asymmetry is larger, consistent with the assumption that the valence quarks dominate in this region.

bin number	x_{bj} bin range
1	0.023 - 0.040
2	0.040 - 0.055
3	0.055 - 0.075
4	0.075 - 0.100
5	0.100 - 0.140
6	0.140 - 0.200
7	0.200 - 0.300
8	0.300 - 0.600

Table 5.1: The x_{bj}-bins for the extraction of the asymmetries.

The inclusive asymmetry is compared with a parameterisation given by GRSV [37]. The asymmetry extracted from HERMES data agrees well with this next-to-leading order analysis of world data available on the proton asymmetry.

The data for the asymmetries shown in figures 5.7 to 5.9 are tabulated in appendix A.

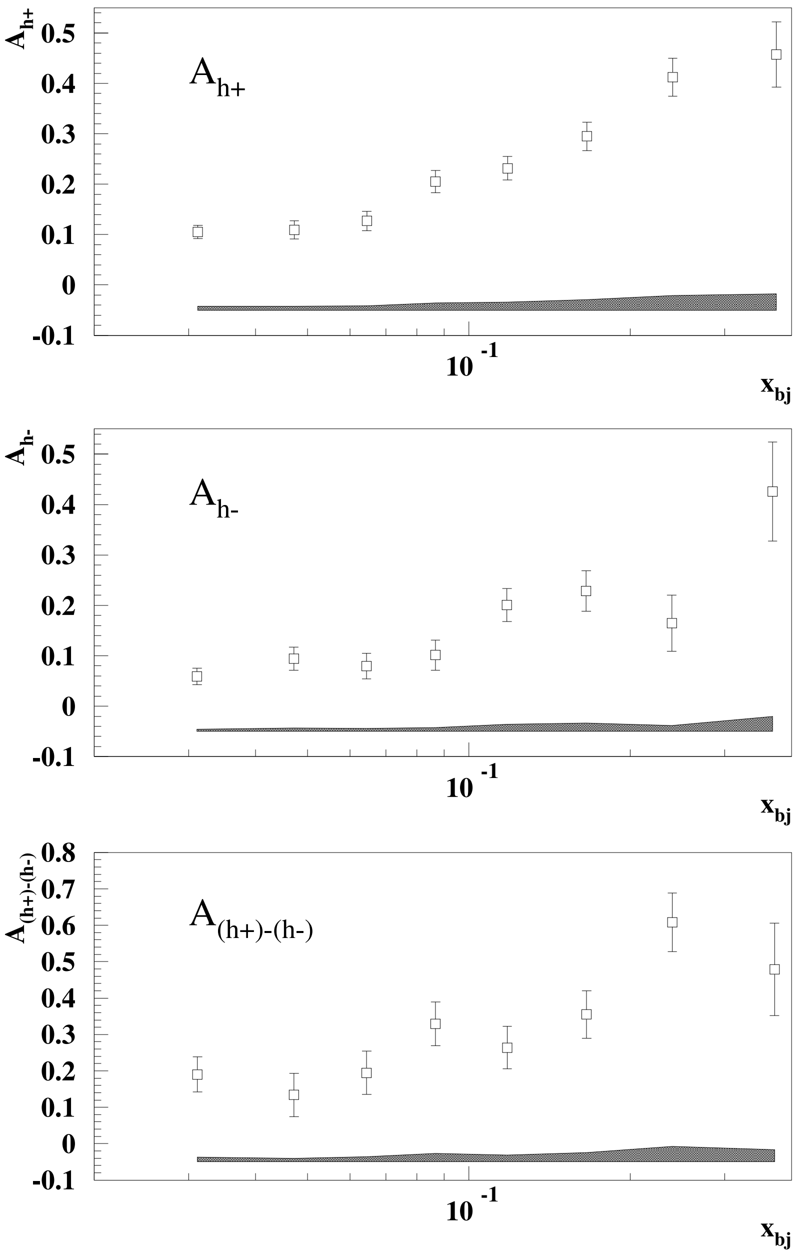

Figure 5.8: The measured single charged hadron asymmetries (top plots) and the hadron charge difference asymmetry (bottom plot) (1996 and 1997). The error bars are statistical only and the band illustrates the estimated systematic uncertainty.

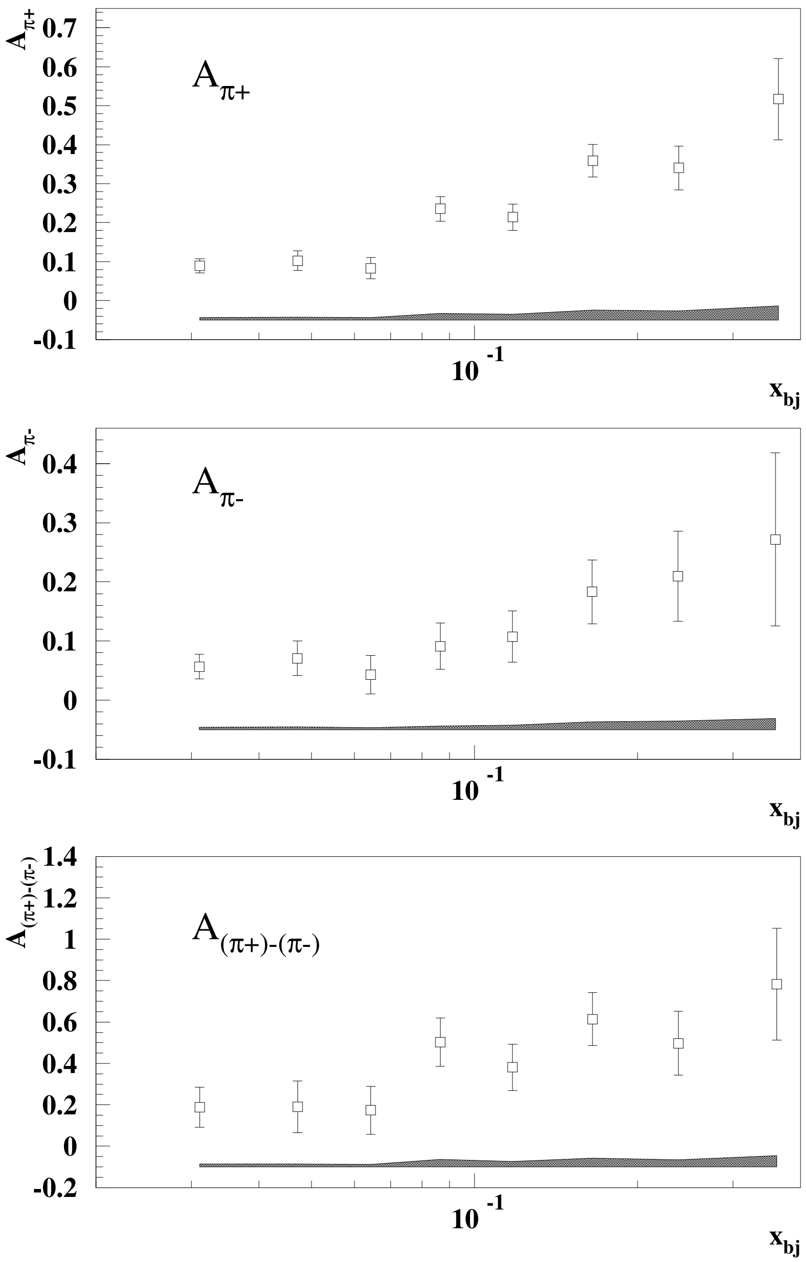

Figure 5.9: The measured single charged pion asymmetries (top plots) and the pion charge difference asymmetries (bottom plots) (1996 and 1997). The error bars are statistical only and the band illustrates the estimated systematic uncertainty.

5.4 Systematic Studies

Stability over Time

Changes in the conditions under which the HERMES experiment is running can cause significant deviations in the measured quantities. It is therefore important to check that these conditions were stable over the long periods of time during which data were being taken.

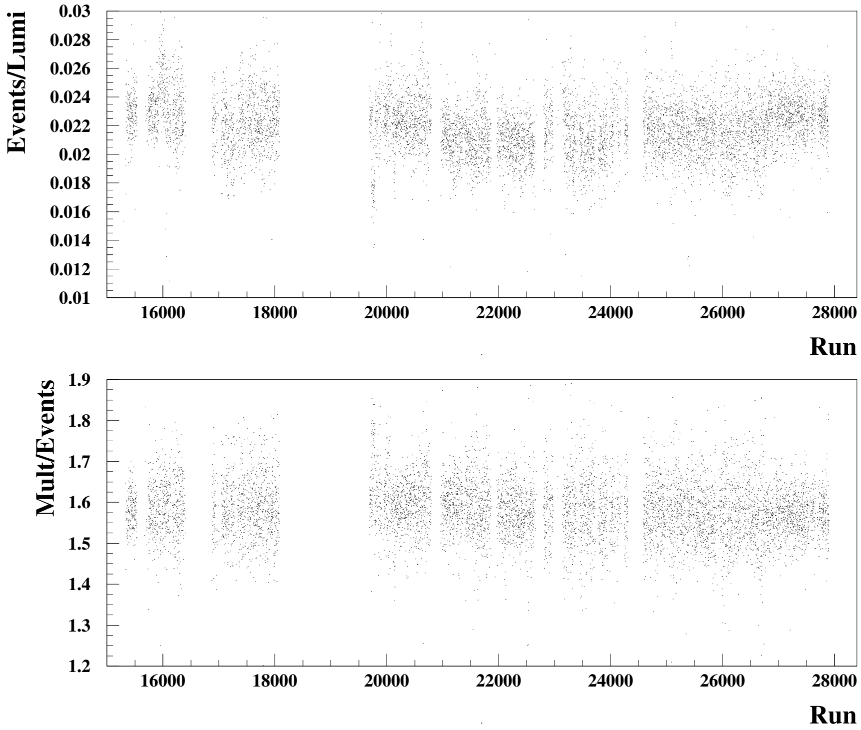

Figure 5.10: Top plot: The ratio of DIS events to luminosity vs run number. Bottom plot: The charge multiplicity as a function of the run number.

Several quantities were investigated to verify the stability of the experiment. The top plot in figure 5.10 shows the number of deep inelastic scattering events divided by the luminosity as a function of the run number. Except for the gaps in the plot that are caused by data that have been discarded by the quality cuts or unpolarised running, the fluctuations are statistical.

Another quantity, the charge multiplicity of an event is shown in the bottom plot of figure 5.10. No time-dependence of the multiplicity is seen, indicating a stable tracking efficiency

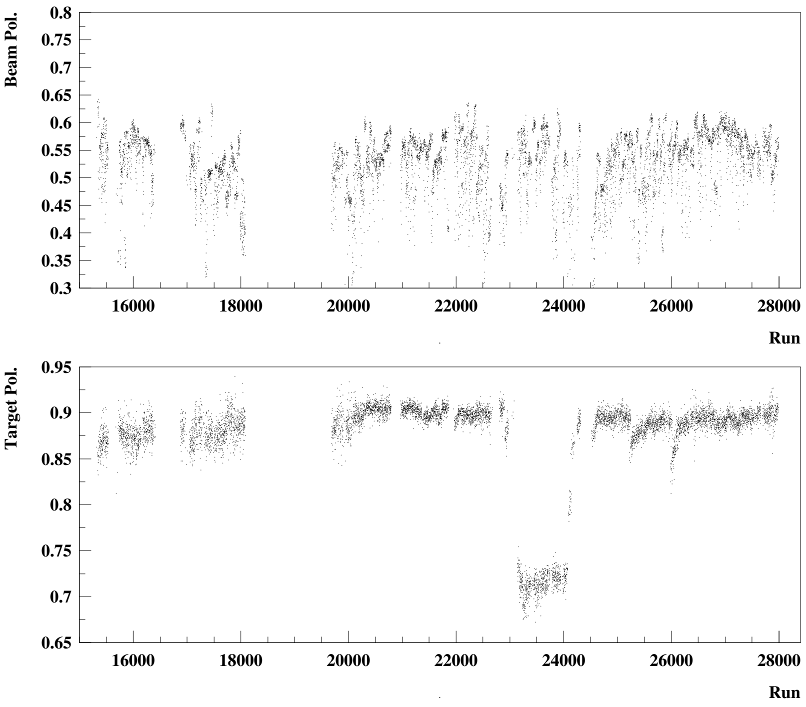

Figure 5.11: The beam polarisation (top) and the target polarisation (bottom) as a function of the run number (1997 data).

of the spectrometer.

For polarised running, reasonable target and beam polarisations are necessary. However, time-dependent fluctuations of the polarisations are possible due to a varying performance of the synchrotron and the target. Figure 5.11 shows both quantities as a function of run number. The lower plot shows the target polarisation corrected for unpolarized molecules and recombination effects in the target gas. The target and beam polarisations are observed to be time-dependent. For example, the small target polarisations for the runs 23,000 to 24,100 are the result of a beam dump in the target cell and a study of the target. Around run 26,000 the low polarisation was caused by another beam dump in the target cell. Except for these periods of known low polarisations, the variations of the target polarisations are statistical. The time dependence of the beam polarisation is caused by changing running conditions and the rise of the beam polarisation during the beginning of a fill.

Finally the time-dependence of the asymmetries averaged over all x_{bj} was studied. As an example the averaged inclusive asymmetry is shown in figure 5.12. The asymmetry is in

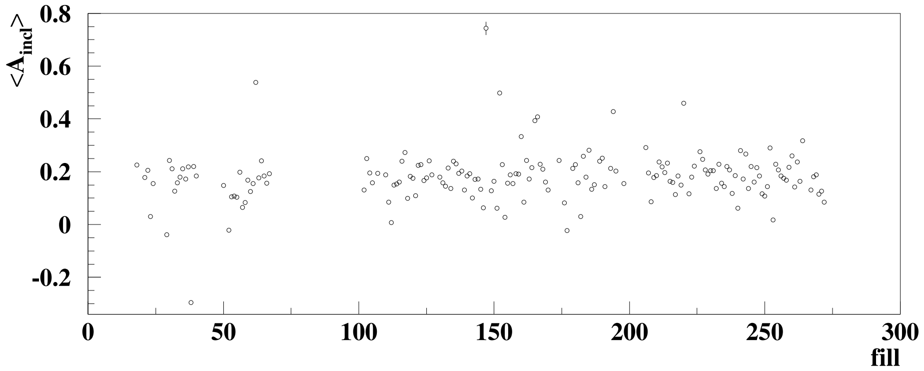

Figure 5.12: The average inclusive asymmetry as a function of the fill number (1997 data). The large gaps are mainly due to unpolarised running periods. The statistical error is very small because of the averaging.

principle time-independent and the fluctuations statistical. The fills with very large or small average asymmetries had too few good data to give significant results.

In conclusion the experimental conditions in 1997 were sufficiently stable to ensure negligible systematic errors caused by varying properties of beam, target and spectrometer. A similar study in [32] verified the stability of the experimental setup in 1996.

Influence of the PID system

The old and new PID schemes were used for the extraction of the data. The 1996 data were analysed with the old scheme and the 1997 data with the new scheme.

The PID quantities calculated with the old scheme were also available for the 1997 data. The influence of the two PID schemes on the 1997 asymmetries could therefore be studied. Figure 5.13 shows the 1997 asymmetries using both PID schemes. The asymmetries agree much better than the statistical uncertainties. A χ^2-analysis of the two data sets showed that the maximum point to point χ^2 value is smaller than 0.04. The good agreement of the two sets of asymmetries was expected due to the agreement of the particle identification schemes (section 4.7). The use of either the new or the old PID scheme has therefore little impact on the asymmetries. This result is important for the analysis of data taken in 1995 and 1996 because only the old PID quantities were available for these years.

In a second study, the influence of the cuts on the identification of hadrons and leptons

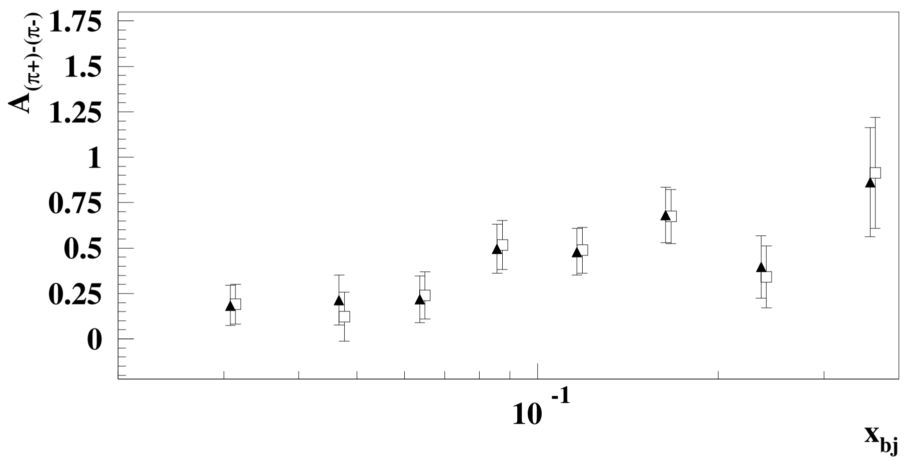

Figure 5.13: The pion charge difference asymmetry calculated with the new PID scheme (triangles) and the old PID scheme (squares). (1997 data; the x_{bj} values are shifted on purpose for clear presentation.)

was investigated. The extracted asymmetries presented in section 5.3 were compared with the results of an analysis with a PID cut at 5 for leptons and -5 for hadrons. The asymmetries of the two analyses are in very good agreement; an average χ^2 of less than 0.3 was calculated. As an example figure 5.14 shows the pion charge difference asymmetry for the two sets of cuts. It can be concluded that the applied PID cuts at 2 for leptons and -1 for hadrons provide sufficiently clean particle samples, while ensuring small statistical errors.

Discrepancies of Data Taken with Opposite Beam Helicities

In 1996 the helicity of the electron beam remained the same, whereas in 1997 the helicity was switched twice during data taking. The helicity was negative in 1996 and the second period in 1997, and positive in the first and third period in 1997. Figure 5.15 shows a comparison of the negative hadron and the charge difference pion asymmetry for the two data sets. The disagreement of the two asymmetries in a number of x_{bj}-bins is apparent. A χ^2-analysis of the two data sets showed that in the case of the negative hadrons the discrepancy is larger than for any of the other asymmetries.

The reason for this discrepancy is not understood at the present time. In principle the

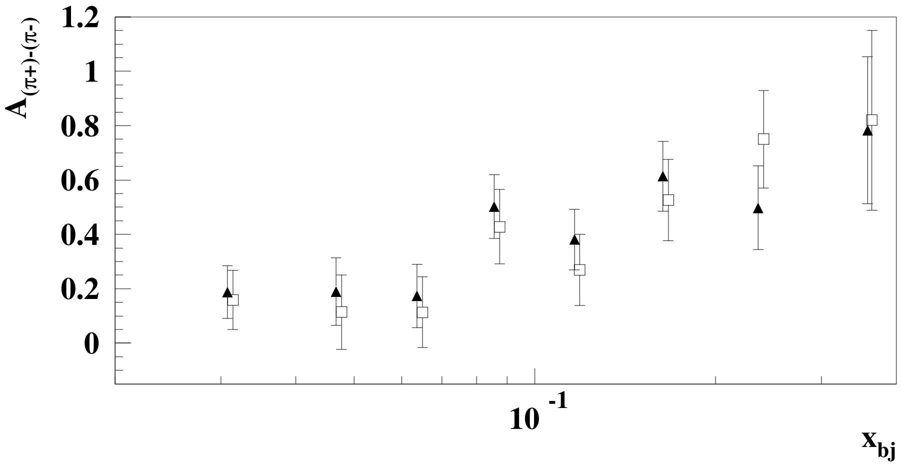

Figure 5.14: The asymmetry $A_1^{\pi^+-\pi^-}$ calculated with hard PID cuts (triangles) and the cuts used in the analysis (squares). (The x_{bj} values are shifted on purpose for a clear representation.)

helicity of the beam has no influence on the scattering reaction, although effects related to transverse polarisation could cause a difference in the cross section for the two beam helicities. The asymmetries presented in section 5.3 were averaged over the two data sets to reduce any systematic error that is introduced by this difference.

The Systematic Error on the Asymmetries

The systematic uncertainty on the asymmetry is caused mainly by the uncertainty on the beam and target polarisation measurements. For 1996 and 1997 data the relative systematic uncertainty of the target polarisation measurement was estimated to be 5% and the relative error of the beam polarisation measurement was 3.4% [13, 38].

Additional errors arise due to the performance of the PID system and the systematic uncertainty on the ratio R of longitudinal and transverse cross-section. The error on the asymmetries was estimated to be 4%, where studies in references [13, 32] were taken into account.

The resulting relative systematic error on the asymmetries is 7%. It is shown as bars in figures 5.7 to 5.9.

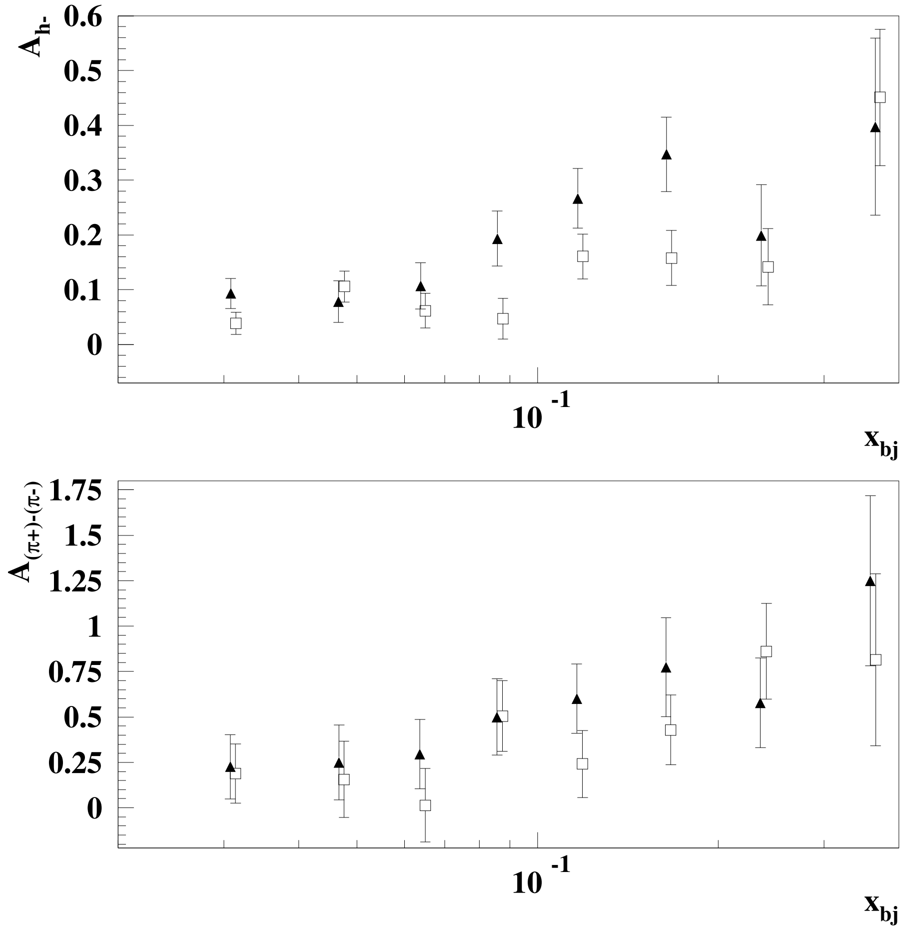

Figure 5.15: Comparison of the asymmetries $A_1^{h^-}$ and $A_1^{\pi^+-\pi^-}$ measured with negative and positive beam helicity (triangles: 1996 and period 2 1997; squares: 1997 period 1 and 3). The x_{bj}-values for the two data sets are shifted intentionally.

Chapter 6

The Polarised Valence Quark Distributions

6.1 The Asymmetries on ^{3}He

The charge difference pion asymmetry on ^{3}He was extracted from HERMES data taken in 1995. 1995 was the commissioning year of the HERMES experiment and the amount of data collected is relatively small due to necessary studies and adjustments of the spectrometer and target. Only about 90,000 semi-inclusive pions were identified in the data compared to 330,000 pions in 1996 and 1997 for hydrogen.

The analysis of the data was done by Felix Menden in 1997 and only the results are presented in this section. The asymmetries were extracted analogously to the procedure described in section 5.3. For details on the cuts and data quality the reader is referred to [32]. The pion asymmetry on ^{3}He is shown in figure 6.1. The bar illustrates the systematic error which was estimated to be 7.0%. Numerical results are given in table A.5 in appendix A. The statistical uncertainties are significantly larger than for the asymmetries on the proton due to the small amount of data taken in 1995. Within these error bars the asymmetry is observed to be consistent with zero.

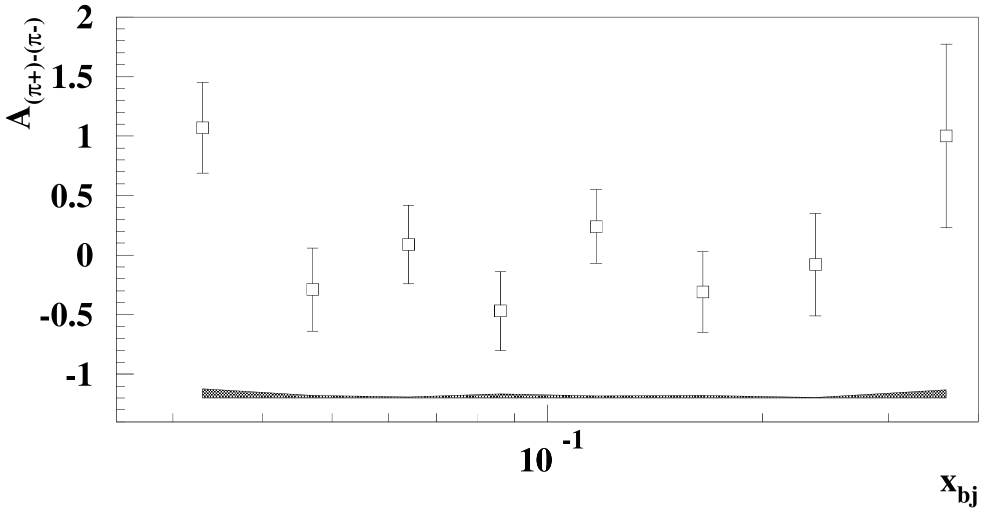

Figure 6.1: The pion charge difference asymmetry on ^{3}He (1995).

6.2 The Valence Quark Distributions $\Delta u^v(x)$ and $\Delta d^v(x)$

The spin dependent valence quark distributions $\Delta u^v(x)$ and $\Delta d^v(x)$ were calculated from the pion charge difference asymmetries on the proton presented in chapter 5 and the ^{3}He-asymmetries shown in the previous section. The calculation is based on equations (2.46) and therefore also involves the unpolarised quark distributions $q^v(x)$. These functions were taken from the MRST parameterisation described in section 2.5.

The distributions are shown in figure 6.2. Also shown is the GRSV parameterisation [37]. Both functions are in reasonable agreement with the parameterisation of world data that was available in 1996[1]. The parameterisation was evaluated using parton model predictions for the inclusive asymmetries, whereas in this thesis the functions were extracted by tagging the flavor of the struck quark using semi-inclusive asymmetries.

The agreement of the final results confirms that the polarised valence quark distributions are described correctly, although the uncertainties are still large.

[1] The world data used for the parameterisation does not include data from the HERMES experiment.

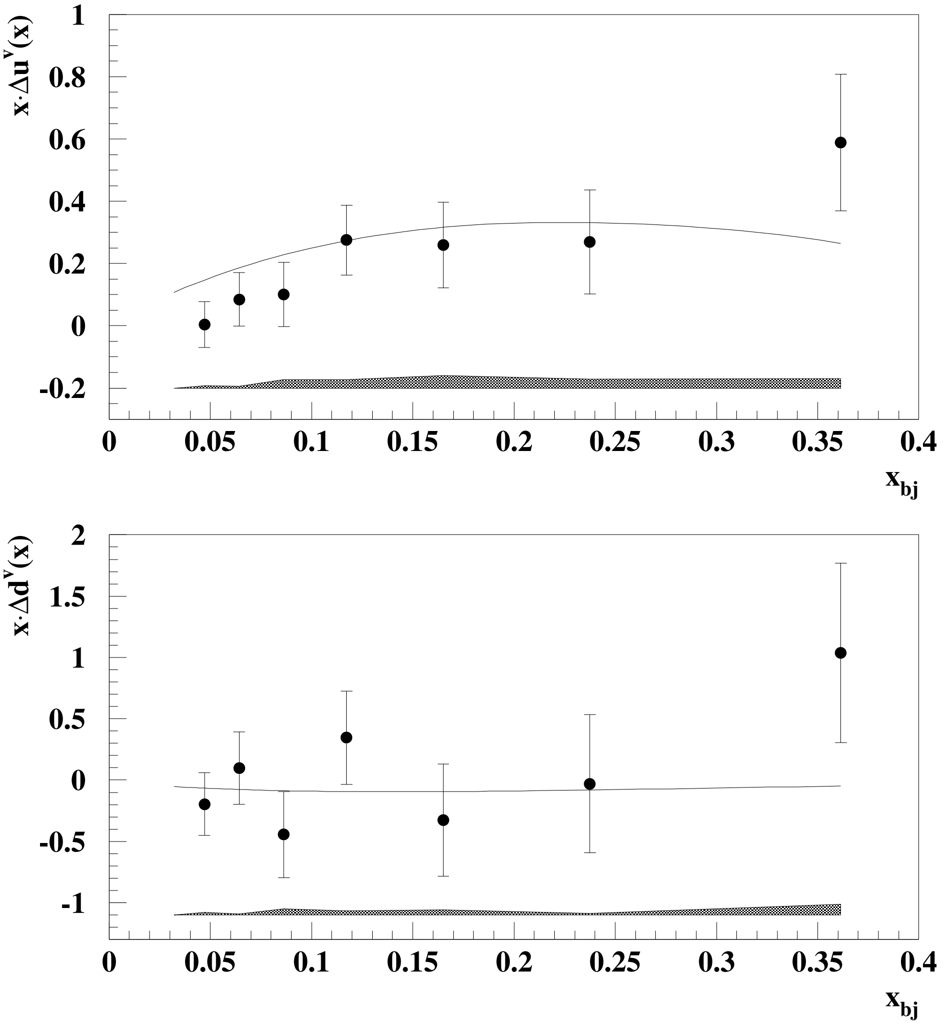

Figure 6.2: The spin distribution function of the valence up and the valence down quarks in the proton. The solid line shows the GRSV parameterisation. The bar at the bottom of the plots illustrates the estimated systematic error.

6.3 Systematic Studies

The systematic uncertainties for the polarised valence quark distributions were calculated from the systematic errors on the proton asymmetries (see section 5.4) and the uncertainty on the ^{3}He asymmetries (section 6.1).

The error that arises from the MRST parameterisation was estimated by comparing it with the CTEQ5 and the GRV parameterisations of world data [39, 40]. An average error of 4.9% was assigned to the MRST parameterisation of the up quark and 8.3% to the distribution of the down quark.

In addition, a systematic error introduced by the assumption of isospin symmetry of the fragmentation functions was studied. Isospin symmetry led to the favoured and unfavoured fragmentation functions $D_1(z)$ and $D_2(z)$ (cf. section 2.4), which significantly simplified the formulas for the polarised valence quark distributions. The influence of this assumption on the asymmetries was studied by deriving equations of the polarised valence quark distributions that take deviations of the fragmentation functions from the favoured and unfavoured functions into account. The estimated uncertainty on the distributions, which is the result of this study, is 5%. A more detailed analysis with a Monte Carlo simulation will likely result not only in a more accurate systematic error, but in a correction of the distributions.

The resulting overall systematic uncertainty is shown as the bars in figure 6.2. On average, the uncertainty is 13% for the valence up-quark and 11% for the valence down-quark.

Chapter 7

Conclusion

The HERMES experiment has been taking data since 1995 when a ^{3}He target was used and data for analysis of the neutron structure were taken. In this thesis, the analysed data were taken in 1996 and 1997 with a H target.

In the analysis, it is necessary to discriminate the particle type of the outgoing particles. The particle identification system of the HERMES experiment consists of a calorimeter, a preshower detector, a Čerenkov counter, and a transition radiation detector. Particle identification relies on a probability based analysis of the detector responses. New, more accurate, parent distributions for the probability analysis were extracted from data and the performance of the system was investigated with a Monte Carlo simulation. The simulation showed that the parent distributions reproduce the single detector responses very well. Furthermore, good agreement between the new and the old schemes for the discrimination of hadrons and leptons was found, a result that is of importance for the analysis of 1995 and 1996 data where the old scheme was used for particle identification.

The Monte Carlo simulation is the only reliable way to determine the performance of the particle identification system when all four detectors are used. The contamination/efficiency analysis with the simulation verified the assumption that the (guessed) exponential tails underestimate the discrimination power of the PID system used at HERMES. The hadron rejection factor of the whole particle identification system, before the trigger, was estimated to be about six thousand at a 98% positron efficiency. The particle identification system therefore provides very clean positron and hadron samples.

The accuracy of the estimate is impaired by the fact that the Monte Carlo does not simulate correlations between the detectors, which are small but crucial to accurately estimate the performance of the PID system. However, the technique used to generate the Monte Carlo data is not insufficient in principle. It would work if more data were available to generate multi-dimensional parent distributions that simulate the correlations. Another possibility is a Monte Carlo that simulates the interactions of the particles with the spectrometer on a microscopic level. Such a simulation does not rely on available data, but on models of the underlying processes. The simulation of the correlations is therefore possible if the theoretical models describe the interactions sufficiently well. However, such a simulation generally requires long computing times. The existing HERMES Monte Carlo simulation would need to be heavily modified to allow for the simulation of the detectors in a reasonable time for PID studies at the 10^{-4} precision level.

In the second part of this thesis, the extraction of inclusive and semi-inclusive spin asymmetries from data taken in 1996 and 1997 was presented. The parton model was applied to extract the polarised valence quark distributions from the pion charge difference asymmetries on H and ^{3}He. The uncertainties of $\Delta u^v(x)$ and $\Delta d^v(x)$ are mostly statistical and dominated by the low statistics of the ^{3}He asymmetry. The two structure functions agree within the errors, with the next-to-leading order GRSV parameterisation. Therefore the extraction of $\Delta u^v(x)$ and $\Delta d^v(x)$ from the pion charge difference asymmetries on H and ^{3}He gives consistent results within the precision of the data. The assumption of favoured, unfavoured, and strange fragmentation functions is valid within these uncertainties.

The results for the polarised valence quark distributions given in this thesis are only intermediate. The statistical uncertainty on the parton distribution functions is expected to be significantly reduced when 1998 and 1999 data on deuterium are analysed. The contributions by the valence quarks to the proton spin can be extracted by incorporating theoretical models to describe the regions in x_{bj} where no data are available. The spin content of the valence quarks is then determined by integrating the distributions over all x_{bj}. The final HERMES data set will not only allow for a determination of the distributions $\Delta u^v(x)$ and $\Delta d^v(x)$ but generally provide a precise measurement of the spin structure of both the proton and the neutron.

Appendix A

Tables of Results

$< x_{bj} >$	$< Q^2 >$	$A_{1,p}$	σ_{stat}	σ_{syst}
0.032	1.080	0.080	0.006	0.003
0.047	1.384	0.106	0.007	0.004
0.065	1.681	0.115	0.008	0.004
0.087	1.984	0.175	0.010	0.006
0.119	2.304	0.218	0.010	0.008
0.168	2.661	0.267	0.013	0.009
0.244	3.131	0.361	0.016	0.012
0.392	4.274	0.541	0.021	0.019

Table A.1: The inclusive asymmetries for the proton (1996 and 1997 data)

$< x_{bj} >$	$< Q^2 >$	$A_{1,p}^{h^+}$	σ_{stat}	σ_{syst}
0.031	1.032	0.105	0.013	0.004
0.047	1.398	0.110	0.018	0.004
0.065	1.753	0.127	0.019	0.004
0.087	2.181	0.205	0.022	0.007
0.118	2.750	0.232	0.024	0.008
0.166	3.581	0.295	0.028	0.010
0.240	4.776	0.412	0.038	0.014
0.375	6.551	0.457	0.065	0.016

$< x_{bj} >$	$< Q^2 >$	$A_{1,p}^{h^-}$	σ_{stat}	σ_{syst}
0.031	1.038	0.059	0.016	0.002
0.047	1.415	0.094	0.023	0.003
0.064	1.779	0.079	0.025	0.003
0.087	2.211	0.101	0.030	0.004
0.118	2.794	0.201	0.033	0.007
0.166	3.675	0.229	0.040	0.008
0.239	4.930	0.165	0.056	0.006
0.369	6.908	0.426	0.098	0.015

Table A.2: The semi-inclusive hadron asymmetries for the proton (1996 and 1997 data)

$< x_{bj} >$	$< Q^2 >$	$A_{1,p}^{\pi^+}$	σ_{stat}	σ_{syst}
0.031	1.049	0.089	0.018	0.003
0.047	1.441	0.102	0.025	0.004
0.064	1.831	0.083	0.027	0.003
0.087	2.325	0.235	0.032	0.008
0.118	3.017	0.214	0.034	0.007
0.165	4.088	0.359	0.042	0.013
0.238	5.711	0.340	0.056	0.012
0.364	8.262	0.517	0.105	0.018

$< x_{bj} >$	$< Q^2 >$	$A_{1,p}^{\pi^-}$	σ_{stat}	σ_{syst}
0.031	1.052	0.057	0.021	0.002
0.047	1.454	0.071	0.029	0.002
0.064	1.845	0.043	0.033	0.002
0.086	2.332	0.091	0.039	0.003
0.118	3.042	0.107	0.043	0.004
0.165	4.129	0.183	0.054	0.006
0.238	5.740	0.209	0.076	0.007
0.360	8.100	0.272	0.146	0.010

Table A.3: The semi-inclusive pion asymmetries for the proton (1996 and 1997 data)

$< x_{bj} >$	$< Q^2 >$	$A_{1,p}^{h^+-h^-}$	σ_{stat}	σ_{syst}
0.031	1.035	0.190	0.048	0.007
0.047	1.407	0.134	0.059	0.004
0.064	1.766	0.195	0.059	0.007
0.087	2.196	0.329	0.060	0.012
0.118	2.772	0.264	0.058	0.009
0.166	3.628	0.355	0.065	0.013
0.240	4.853	0.608	0.080	0.021
0.372	6.729	0.479	0.127	0.017

$< x_{bj} >$	$< Q^2 >$	$A_{1,p}^{\pi^+-\pi^-}$	σ_{stat}	σ_{syst}
0.031	1.051	0.188	0.097	0.007
0.047	1.447	0.190	0.125	0.007
0.064	1.838	0.173	0.116	0.006
0.087	2.328	0.502	0.117	0.017
0.118	3.029	0.381	0.111	0.013
0.165	4.108	0.614	0.128	0.022
0.238	5.725	0.497	0.154	0.017
0.362	8.181	0.783	0.271	0.027

Table A.4: The semi-inclusive charge difference asymmetries for the proton (1996 and 1997 data)

$< x_{bj} >$	$< Q^2 >$	$A_{1,^3\mathrm{He}}^{\pi^+-\pi^-}$	σ_{stat}	σ_{syst}
0.033	1.24	1.07	0.38	0.037
0.047	1.54	−0.29	0.35	0.010
0.064	1.93	0.09	0.33	0.003
0.086	2.47	−0.47	0.33	0.016
0.117	3.26	0.24	0.31	0.008
0.165	4.40	−0.31	0.34	0.011
0.237	6.10	−0.08	0.43	0.003
0.361	8.80	1.00	0.77	0.035

Table A.5: The pion charge difference asymmetries on ^{3}He (1995 data)

$< x_{bj} >$	$< Q^2 >$	$x\Delta u^v(x)$	σ_{stat}	σ_{syst}	$x\Delta d^v(x)$	σ_{stat}	σ_{syst}
0.047	1.493	0.004	0.074	0.008	−0.197	0.256	0.020
0.064	1.884	0.085	0.086	0.007	0.097	0.296	0.008
0.086	2.399	0.101	0.102	0.027	−0.445	0.352	0.051
0.117	3.144	0.275	0.112	0.026	0.345	0.381	0.033
0.165	4.253	0.260	0.137	0.040	−0.326	0.458	0.043
0.238	5.911	0.269	0.168	0.029	−0.031	0.563	0.013
0.361	8.488	0.588	0.219	0.030	1.037	0.731	0.087

Table A.6: The extracted polarised valence quark distributions using 1995 data on ^{3}He, and 1996-97 data on H.

Appendix B

Contributions to HERMES

Modern experiments in elementary particle physics are usually large projects and many people are involved in their realisation. The HERMES collaboration consists of close to 200 collaborators from 10 countries. In this section my personal contributions to the physics program of the HERMES experiment are described.

I joined the HERMES collaboration in January 1998 and started working on the Monte Carlo simulation for PID analysis described in chapter 4. This included extensive systematic studies and modifications to the computer program. The particle identification routines of the simulation were implemented in the HERMES data analysis package and are now commonly used to discriminate positrons and hadrons.

Furthermore I analysed the HERMES data taken in 1996 and 1997. I extracted the inclusive and semi-inclusive asymmetries on hydrogen as described in chapter 5. Among other systematic studies I specifically studied the influence of the new particle identification scheme. Finally I used the H asymmetries and the ^{3}He asymmetries to calculate the polarised valence quark distributions in the proton (see chapter 6).

At DESY in Hamburg, where I spent about six weeks in 1998 and 1999, I became acquainted with the experiment. I took two weeks of shifts as a spectrometer person during which I made sure that the spectrometer was running properly, so that a maximum amount of data could be taken. Furthermore I took part in the data quality checks of the transition radiation detector. The TRD data quality is checked daily to ensure stable running of the detector and to find any problems that may influence the data analysis.

Bibliography

[1] R. McAllister, R. Hofstadter, Phys. Rev. **102** (1956) 851

[2] A. Afanasev, C. E. Carlson, C. Wahlquist, Phys. Rev. **D58** (1998) 054007, hep-ph/9706522

[3] T.-C. Meng, J.-C. Pan, Q. bing Xie, W. Zhu, Phys. Rev. **D40** (1989) 769

[4] E. Berger, *Semi-Inclusive Inelastic Electron Scattering from Nuclei*, Workshop on Electronuclear Physics with Internal Targets (Stanford 1987), ANL-HEP-PR-87-45

[5] W. Greiner, A. Schäfer, Quantum Chromodynamics (Springer, 1995)

[6] M. Alguard, *et al.*, Phys. Rev. Lett. **37** (1976) 1261

[7] G. Baum, *et al.*, Phys. Rev. Lett. **51** (1983) 1135

[8] R. Feynman, Photon-Hadron Interactions (W. A. Benjamin, Inc., 1972)

[9] J. Bjørken, Phys. Rev. Lett. **179** (1969) 1547

[10] F. Close, An Introduction to Quarks and Partons (Academic Press, 1979)

[11] F. Halzen, A. Martin, Quarks and Leptons: An Introductory Course In Modern Particle Physics (John Wiley, 1984)

[12] C. Callan, D. Gross, Phys. Rev. Lett. **21** (1968) 311

[13] A. Airapetian, *et al.*, Phys. Lett. **B 442** (1998) 484, hep-ex/9807015, HERMES internal note 98 047

[14] K. Ackerstaff, *et al.*, Phys. Lett. **B 404** (1997) 383, hep-ex/9703005, HERMES internal note 97 008

[15] M. Vetterli, *The Spin Structure of the Nucleon*, Lake Louise Winter Institute, published in World Scientific (1998), HERMES internal note 98 065

[16] L. Whitlow, *et al.*, Phys. Lett. **B 250** (1990) 193

[17] Frankfurt, *et al.*, Phys. Lett. **B 230** (1989) 141

[18] A. Martin, *et al.*, Eur. Phys. J. **C 4** (1998) 463

[19] A. Sokolov, I. Ternov, Sov. Phys. Dokl. **8** (1964) 1203

[20] D. Barber, *et al.*, Nucl. Instr. and Meth. **A 329** (1993) 79

[21] D. Barber, *et al.*, Nucl. Instr. and Meth. **A 338** (1994) 166

[22] J. Buon, K. Steffen, Nucl. Instr. and Meth. **A 245** (1986) 248

[23] W. Lorenzon, *Beam Polarimetry at HERA*, Proc. of the Workshop on pol. Targets and Sources (Urbana-Champaign, USA 1997), HERMES internal note 97 068

[24] K. Zapfe, *et al.*, Nucl. Instr. and Meth. **A 368** (1996) 293

[25] F. Stock, *et al.*, Nucl. Instr. and Meth. **A 343** (1994) 334

[26] B. Braun, *The HERMES polarimeter*, Proc. of the Workshop on pol. Targets and Sources (Urbana-Champaign, USA 1997), HERMES internal note 97 061

[27] K. Ackerstaff, *et al.*, Nucl. Instrum. Meth. **A 417** (1998) 230, hep-ex/9806008, HERMES internal note 98 035

[28] W. Wander, Ph.D. thesis, Friedrich Alexander Universität Erlangen-Nürnberg, (1996), English translation: HERMES internal note 97 031

[29] R. Fernow, Introduction to Experimental Particle Physics (Cambridge University Press, 1986)

[30] R. Kaiser, *Particle Identification at HERMES*, 1997, HERMES internal note 97 025

[31] I. Bronstein, K. Semendjajew, Taschenbuch der Mathematik (B. G. Teubner, 1991)

[32] F. Menden, Diploma Thesis, TRIUMF/ Hamburg, 1997, HERMES internal note 98 001

[33] P. Bevington, D. Robinson, Data Reduction and Error Analysis for the Physical Sciences (McGraw-Hill, Inc., 1992)

[34] W. Herold, *et al.*, Nucl. Instr. Meth. **217** (1983) 277, hep-ph/9508347

[35] R. Kaiser, Ph.D. thesis, Simon Fraser University, 1997, HERMES internal note 97 017

[36] Y. Gärber, *private communication*

[37] M. Glück, *et al.*, Phys. Rev. **D53** (1996) 4775, hep-ph/9508347

[38] K. Ackerstaff, *et al.*, *Flavor Decomposition of the Polarized Quark Distributions in the Nucleon from Inclusive and Semi-Inclusive Deep-inelastic Scattering*, to be published

[39] H. L. Lai, *et al.*, *Global QCD analysis of parton structure of the nucleon: CTEQ5 parton distributions* (1999), hep-ph/9903282

[40] M. Glück, E. Reya, A. Vogt, Eur. Phys. J. **C5** (1998) 461, hep-ph/9806404

[41] M. Vetterli, *private communication*

[42] H. Tallini, Ph.D. thesis, University of Liverpool, 1998, HERMES internal note 98 024

[43] D. de Schepper, Ph.D. thesis, Massachusetts Institute of Technology, 1997, HERMES internal note 97 022